Peer Reviewed

Title:
In situ Analytical Characterization of Interfacial Phenomena in All-Solid-State Lithium Ion Thin Film Batteries

Author:
Wang, Ziying

Acceptance Date:
2016

Series:
UC San Diego Electronic Theses and Dissertations

Degree:
Ph.D., Chemical EngineeringUC San Diego

Advisor(s):
Meng, Ying S

Committee:
Fenning, David, Fullerton, Eric, Villa, Elizabeth, Gianneschi, Nathan

Abstract:

UNIVERSITY OF CALIFORNIA, SAN DIEGO

In situ Analytical Characterization of Interfacial Phenomena in All-Solid-State Lithium Ion Thin Film Batteries

A dissertation submitted in partial satisfaction of the
requirements for the degree Doctor of Philosophy

in

Chemical Engineering

by

Ziying Wang

Committee in charge:

Professor Ying Shirley Meng, Chair
Professor David Fenning
Professor Eric Fullerton
Professor Nathan Gianneschi
Professor Elizabeth Villa

2016

The Dissertation of Ziying Wang is approved, and it is acceptable in quality and form for publication on microfilm and electronically:

_____

_____

_____

_____

_____

Chair

University of California, San Diego

2016

DEDICATION

To Boqian Wang and Guangqi Cheng

TABLE OF CONTENTS

LIST OF FIGURES

LIST OF TABLES

ACKNOWLEDGEMENTS

Firstly, I would like to thank my thesis advisor Dr. Ying Shirley Meng for providing me the opportunities to do this research and her continuous support. She saw potential in me that no one else did and taught me how to face adversity appropriately. I would also like to express my gratitude to my other committee members: Dr. Eric Fullerton, Dr. David Fenning, Dr. Nathan Gianneschi, and Dr. Elizabeth Villa for their time and guidance.

Secondly, I would like to acknowledge my collaborators and co-authors at UCSD, Dr. Kyler Carroll, Dr. Dhamodaran Santhanagopalan, Dr. Danna Qian, Dr. Cyrus Rustomji, Jungwoo Lee, and Thomas Wynn with whom I had many useful and stimulating discussions. I'm also grateful to all my group mates in Laboratory for Energy Storage and Conversion (LESC) who have helped and inspired me in many ways.

Finally, I would like to express my gratitude to my collaborators and co-authors, Dr. Juchuan Li, Dr. Nancy Dudney at Oak Ridge National Lab, Dr. Feng Wang, Dr. Wei Zhang, Dr. Huolin Xin, Dr. Kai He, Lili Han at Brookhaven National Lab, and Dr. Delphine Guy-Bouyssou, Dr. Emilien Bouyssou, Dr. Marina Proust, and Nathanael Grillon at STMicroelectronics for their expertise, time and invaluable support throughout the projects.

Last but not least, my deepest gratitude goes to my parents Boqian Wang and Guangqi Cheng for their support. I would also like to thank my friends Tyler, Melanie, Amanda, Jeff, Timm, and Avital for their support through graduate school.

I would like to acknowledge the financial support from the Office of Basic Energy Sciences, under award number DE-SC0002357. The collaboration with national labs is made possible with partial support of the Northeastern Center for Chemical Energy Storage, an Energy Frontier Research Center funded by the U.S. Department of Energy, Office of Basic Energy Sciences, under award number DE-SC0001294.

Chapter 4, in full, is a reprint of the material "Analytical Electron Microscopy – Study of All-Solid-State Batteries" as it appears in Handbook of Solid State Batteries 2nd Edition, Ziying Wang, Ying Shirley Meng, World Scientific, 2015, pp 109-131. The dissertation author was the co-primary investigator and author of this book chapter. All the experiments and writing were performed by the author.

Chapter 5, in full, is a reprint of the material "Interface Limited Lithium Transport in Solid-State Batteries" as it appears in the Journal of Physical Chemistry Letters, Dhamodaran Santhanagopalan, Danna Qian, Thomas McGilvray, Ziying Wang, Feng Wang, Fernando Camino, Jason Graetz, Nancy Dudney, and Ying Shirley Meng, 2014, 5, 298-303. The dissertation author was a co-primary investigator and author of this paper. The author wrote the STEM-EELS analysis of anode-electrolyte interface part.

Chapter 6, in full, is a reprint of the material "*In situ* STEM-EELS Observation of Nanoscale Interfacial Phenomena in All-Solid-State Batteries" as it appears in Nano Letters, Ziying Wang, Dhamodaran Santhanagopalan, Wei Zhang, Feng Wang, Huolin L. Xin, Kai He, Juchuan Li, Nancy Dudney, Ying Shirley Meng, 2016, 16 (6), 3760-3767. The dissertation author was a co-primary investigator and author of this paper.

All the experiment and writing were conducted by the author except for STEM-EELS data collection and the particular *in situ* charge.

Chapter 7, in full, is a reprint of the material "Effects of Cathode Electrolyte Interfacial (CEI) Layer on Long Term Cycling of All-Solid-State Thin-Film Batteries" as it appears in Journal of Power Sources, Ziying Wang, Jungwoo Z. Lee, Huolin L. Xin, Lili Han, Nathanael Grillon, Delphine Guy-Bouyssou, Emilien Bouyssou, Marina Proust, Ying Shirley Meng, 2016, 324, 342-348. The dissertation author was a co-primary investigator and author of this paper. All the experiment and writing were conducted by the author except for STEM-EELS data collection.

VITA

2011	Bachelor of Science, California Institute of Technology, CA
2013	Master of Science, University of California, San Diego, CA
2016	Doctor of Philosophy, University of California, San Diego, CA

PUBLICATIONS

1. **Wang, Z.**; Meng, Y. S., Analytical Electron Microscopy Study of All Solid-State Batteries. In Handbook of Solid State Batteries, WORLD SCIENTIFIC: 2015; Vol. Volume 6, pp 109-131.

2. **Wang, Z.**; Santhanagopalan, D.; Zhang, W.; Wang, F.; Xin, H.; He, K.; Li, J.; Dudney, N. J.; Meng, Y. S. Nano Letters 2016, 16 (6), 3760-3767

3. **Wang, Z.**; Lee, J. Z.; Xin, H.; Han, L.; Grillon, N.; Guy-Bouyssou, D.; Bouyssou, E.; Proust, P.; Meng, Y. S. Journal of Power Sources 2016, 324, 342-348

4. Santhanagopalan, D.; Qian, D.; McGilvray, T.; **Wang, Z.**; Wang, F.; Camino, F.; Graetz, J.; Dudney, N.; Meng, Y. S. The Journal of Physical Chemistry Letters 2013, 5, (2), 298-303.

5. Xu, B.; Qian, D.; **Wang, Z.**; Meng, Y. S. Materials Science and Engineering: R: Reports 2012, 73, (5–6), 51-65.

6. Verde, M. G.; Carroll, K. J.; **Wang, Z.**; Sathrum, A.; Meng, Y. S. Energy & Environmental Science 2013, 6, (5), 1573-1581.

7. Saracibar, A.; **Wang, Z.**; Carroll, K. J.; Meng, Y. S.; Dompablo, M. E. A.-d. Journal of Materials Chemistry A 2015, 3, (11), 6004-6011.

8. Yoon, H.; Xu, A.; Sterbinsky, G. E.; Arena, D. A.; **Wang, Z.**; Stephens, P. W.; Meng, Y. S.; Carroll, K. J. Physical Chemistry Chemical Physics 2015, 17, (2), 1070-1076.

9. Yersak, T. A.; Shin, J.; **Wang, Z.**; Estrada, D.; Whiteley, J.; Lee, S.-H.; Sailor, M. J.; Meng, Y. S. ECS Electrochemistry Letters 2015, 4, (3), A33-A36.

10. Verde, M. G.; Baggetto, L.; Balke, N.; Veith, G. M.; Seo, J. K.; **Wang, Z.**; Meng, Y. S. ACS Nano 2016, 10, (4), 4312-4321.

ABSTRACT OF THE DISSERTATION

In situ Analytical Characterization of Interfacial Phenomena in
All-Solid-State Lithium Ion Thin Film Batteries

by

Ziying Wang

Doctor of Philosophy in Chemical Engineering

University of California, San Diego, 2016

Professor Ying Shirley Meng, Chair

Lithium ion batteries have become one of the most important rechargeable energy storage devices used in our modern society today. As the demand for such devices shift from portable electronics to electric vehicles and large scale storage in order to utilize energy sustainably, ever increasing energy densities both in terms of weight and volume are needed. To satisfy this demand, lithium ion batteries utilizing solid state electrolytes show promise of a new paradigm shift in energy storage

technologies. The introduction of solid state electrolyte could, in principle, yield many advantages over conventional lithium ion batteries. Foremost, lithium metal can be used as the anode along with a high voltage cathode to boost energy density. Secondly, removal of flammable liquid electrolyte greatly improves the inherent safety of the battery.

We focused on using Focused Ion Beam (FIB) nano-fabrication technique to prepare Transmission Electron Microscopy (TEM) samples of all-solid-state batteries produced through physical vapor deposition techniques. The particular full cell chemistry of lithium cobalt oxide ($LiCoO_2$) as cathode, amorphous silicon (a-Si) as anode, and lithium phosphorus oxynitrdie (LiPON) as electrolyte was used for investigations. Through analysis of TEM images and electron energy loss spectroscopy (EELS), important interfacial phenomena were observed at the anode-electrolyte interface and the cathode-electrolyte interface. Overcharging of the anode resulted in accumulation of lithium at the anode-current collector interface and interdiffusion of phosphorus and silicon atoms at the anode-electrolyte interface.

Furthermore, we developed a unique methodology using FIB fabrication techniques to prepare electrochemically active TEM samples of all-solid-state nanobatteries that can be galvanostatically charged in the FIB or TEM. This new methodology enabled *in situ* TEM observations of a previously undiscovered interfacial layer between the $LiCoO_2$ cathode and LiPON electrolyte. This interfacial layer is composed of a highly disordered rocksalt like cobalt oxide phase that is oxidized and forms lithium oxide species during *in situ* charge. Additionally, electrochemically cycling at elevated temperatures (80 °C) causes further

decomposition of the cathode layer decreasing the overall capacity and increasing interfacial impedance of the cell. These results indicate that proper engineering of electrode-electrolyte interface is essential for the performance of all-solid-state batteries.

Chapter 1. Introduction

1.1. Challenges and Motivation

The greatest challenge facing our society today is the continued increase in global temperature due to the emission of green house gases, namely carbon dioxide, through various human activities. In 2015, the global average temperature was 0.87 °C above the 1951-1980 average. As seen in Figure 1.1, the average temperature has been on the sharp rise in recent decades.

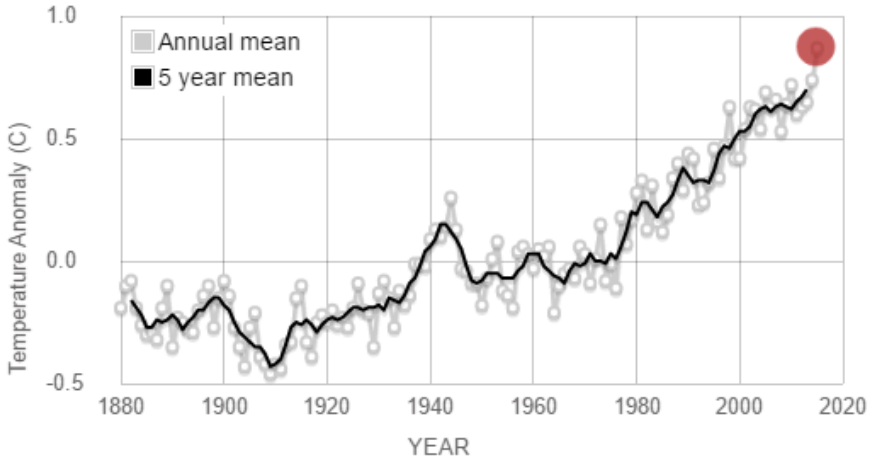

Figure 1.1 Global average temperature deviations from the 1951-1980 average since 1880 [1]

While a cause and effect relationship between global temperature and carbon dioxide atmospheric concentration is difficult to establish to due to other factors such as land vegetation, land surface characteristics, and glacial extent, there has been a strong correlation between the two dating back hundreds of thousands of years as shown in Figure 1.2. More worrisome is the fact that atmospheric carbon dioxide

levels has risen above 400 parts per million in 2015 (Figure 1.3), much higher than the historical record of 300 parts per million before 1950 (Figure 1.4).

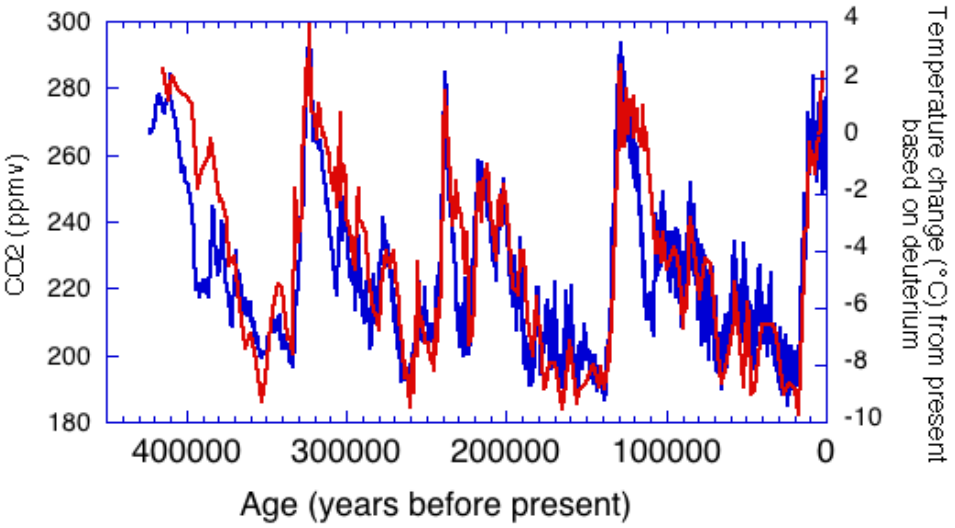

Figure 1.2 Correlation between global temperature and carbon dioxide concentration change. Red line shows the carbon dioxide concentration while blue line shows the global temperature based on deuterium measurements in glacial ice [2]

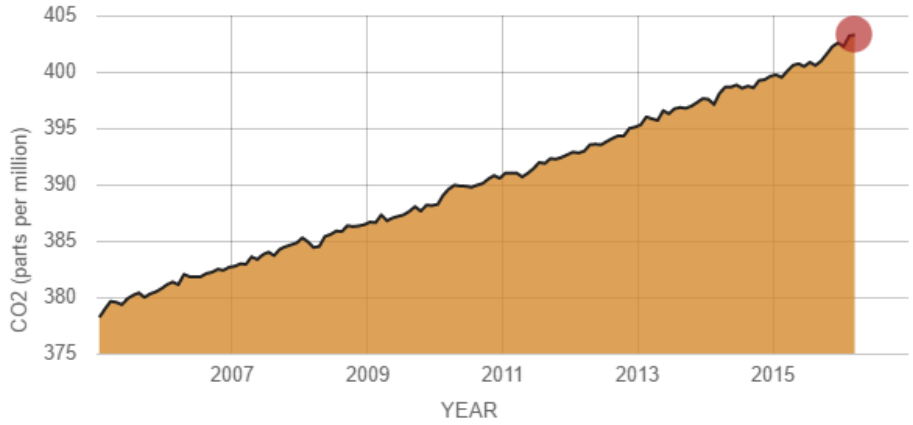

Figure 1.3 Atmospheric measurements of carbon dioxide concentration [3]

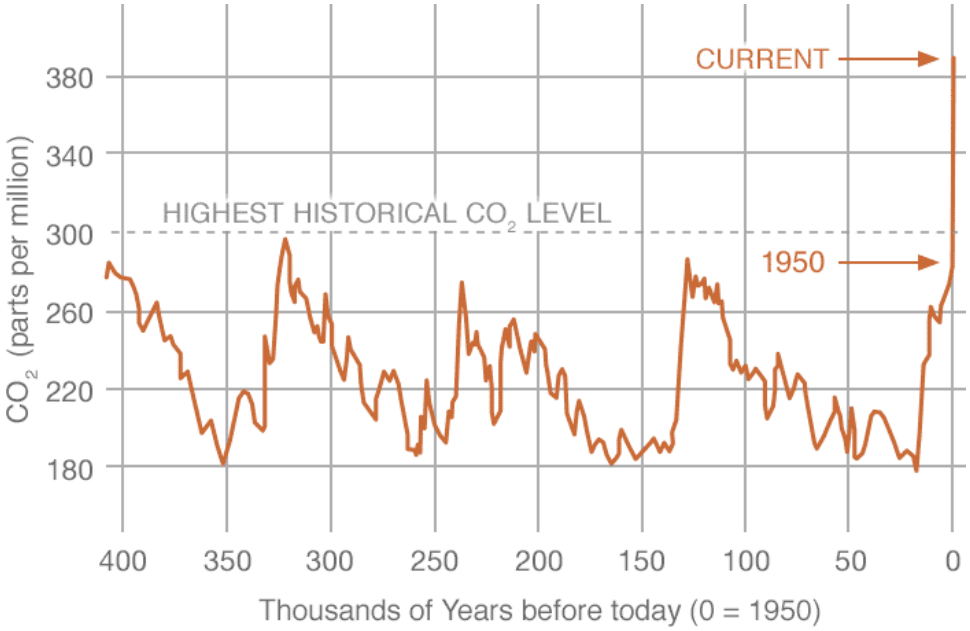

Figure 1.4 Historical measurements of atmospheric carbon dioxide concentrations [3]

The rise of atmospheric carbon dioxide levels has been mostly attributed to human activity through the use of fossil fuels. According to the Environmental Protection Agency [4], global emissions of carbon dioxide can be broken down to 25% electricity and heat production, 24% agriculture, 21% industry, 14% transportation, 6% building, and 10% other uses (Figure 1.5). As more advances in technology allow us to move away from fossil fuel energy generation in electricity production and transportation to renewable energy sources, intermittent energy storage devices become hugely important in the way we manage our energy resources. Advanced batteries allow efficient storage of renewable energy from solar and wind and enable practical driving ranges for electric vehicles. Currently, the most advanced form of energy storage technology is lithium ion batteries as it has the best combination of energy density, cycle life, cost, and safety.

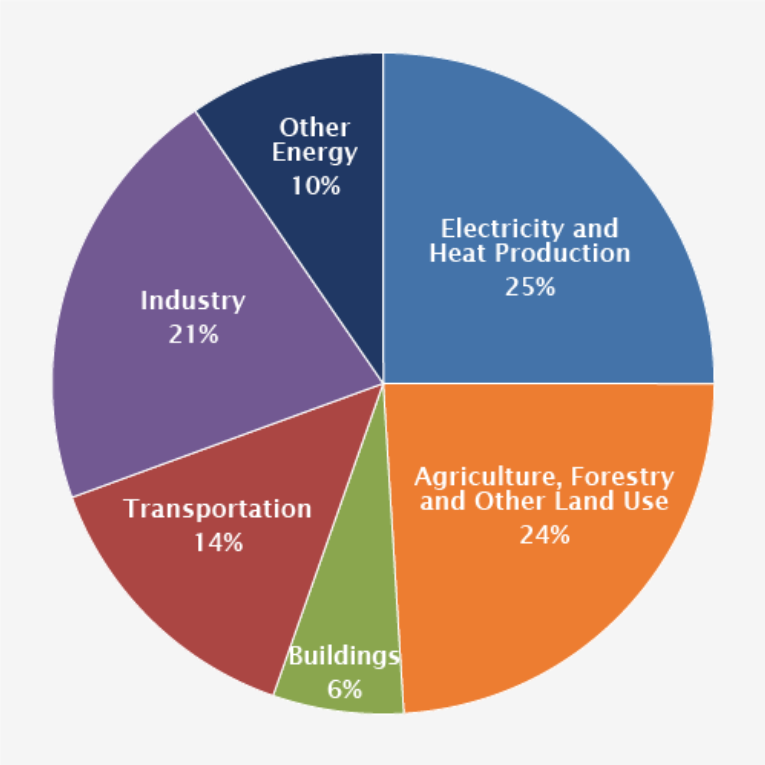

Figure 1.5 Global emissions of greenhouse gases by economic sector [4]

1.2. Lithium Ion Batteries

Lithium ion batteries are devices that can convert chemical energy to electrical energy and vise versa reversibly. The use of lithium ions as the energy carrier allows the highest energy density both in terms of volume and weight. This is due to lithium being the lightest metallic element and having one of the lowest reduction potential of – 3.04V vs standard hydrogen electrode. Figure 1.6 illustrates the fundamental mechanism of lithium ion battery operation. Lithium ion batteries consist of a positive cathode and a negative anode separated by an electrolyte that is ionically conducting to lithium ions but insulating to electrons. In conventional lithium ion batteries, the electrolyte is usually an organic solvent containing lithium salt. The cathode and

anode materials are separated physically by a porous polymer membrane separator that is also electrically insulting. There are currently various reaction mechanisms in research for both the cathode and anode; however, the most used technology involves intercalation reaction of lithium ions with the cathode and anode materials. During charging of the battery, lithium ions are extracted out of the positive cathode and inserted into the negative anode. During this ionic movement, other atomic species in the cathode, usually transition metal ions, are oxidized and give off electrons, while the anode material accepts electrons and becomes reduced. The difference of chemical potential of lithium in the cathode and anode enables the conversion of electrical energy to chemical energy.

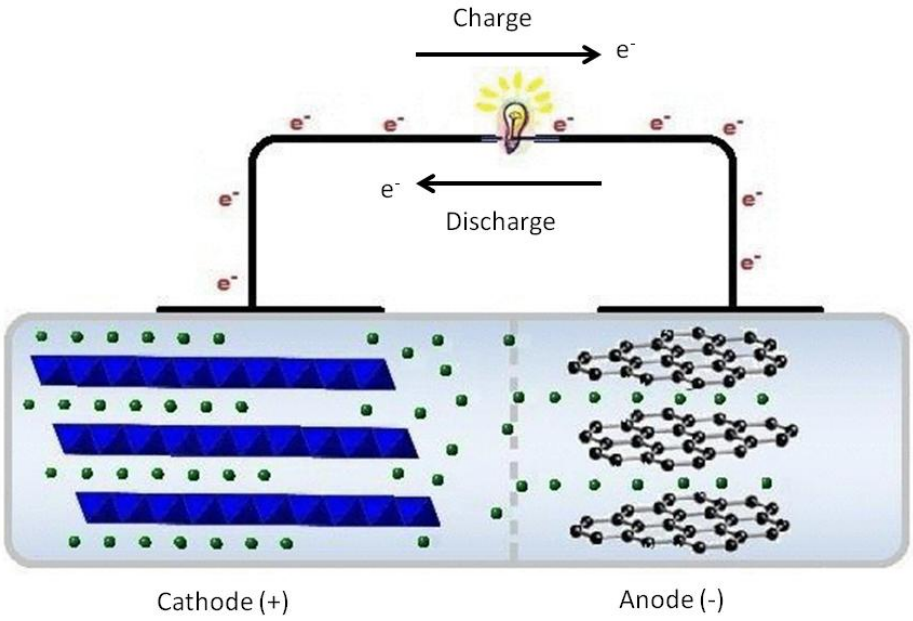

Figure 1.6 Schematic showing the fundamental functions of a lithium ion battery

The first commercial lithium ion batteries consisted of $LiCoO_2$ materials as the cathode and graphite material as the anode. Both materials employ the intercalation

mechanism where lithium ions can move in and out of crystal planes within layers of cobalt octahedra and grapheme. The advantage of intercalation mechanism is minimal structural change of the material upon cycling, allowing thousands of cycles. Additionally, evolution of the organic solvent used in lithium ion batteries was also an important factor in the development of lithium ion batteries. Before the use of ethylene carbonate and dimethylcarbonate mixtures, propylene carbonate was used. However, propylene carbonate would continuously decompose on the surface of graphite during charge voiding any electrical energy put into the cell. The addition of ethylene carbonate enabled formation of a stable solid electrolyte interface (SEI) layer that coats the surface of graphite and prevents further decomposition of the electrolyte. While lithium ion batteries have higher specific energy densities than other technologies such as Ni-Cd and Ni-MH, the use of lithium metal as the anode would further improve its energy density due to lithium metal's high specific capacity. The problem with using lithium metal as the anode in organic liquid electrolyte is the formation of lithium dendrites which causes short circuiting of the battery and potential thermal runaway of the cell. The use of electrolyte additives and solid electrolytes has been explored in the quest to enable lithium metal as the anode in lithium ion batteries.

1.3. All-Solid-State Thin Film Batteries

All-Solid-State thin film batteries are a particular type of rechargeable lithium ion batteries. In these batteries, thin films of cell components on the orders of microns in thickness are deposited by physical vapor deposition techniques such as radio

frequency (RF) magnetron sputtering and pulsed laser deposition. This technology was first realized with the deposition of a solid electrolyte, lithium phosphorus oxynitrde, by Bates et al. in 1992 [5]. Lithium phosphorus oxynitride (LiPON) has an ionic conductivity of 2 x 10^{-6} S/cm and more importantly is stable on contact with lithium metal. Due to their compact size, lithium ion thin film batteries have applications in microelectromechanical (MEM) devices, radio frequency identification (RFID) tags, and lab-on-a-chip devices. Due to the solid nature of the electrolyte, lithium metal can also be used as the anode dendrite formation is limited. A cross sectional schematic of an all-solid-state battery is shown in Figure 1.7. With the use of lithium metal, thin film batteries could potentially exceed the energy density of conventional lithium ion batteries using organic electrolytes. However, manufacturing costs of physical vapor deposition and additional mass of substrate and packing place limitations on the practical applications of thin film batteries. Nonetheless, thin film batteries have the potential to be the next generation of lithium ion battery technologies and the thin film geometry offers a unique platform for characterization of electrode-electrolyte interfaces.

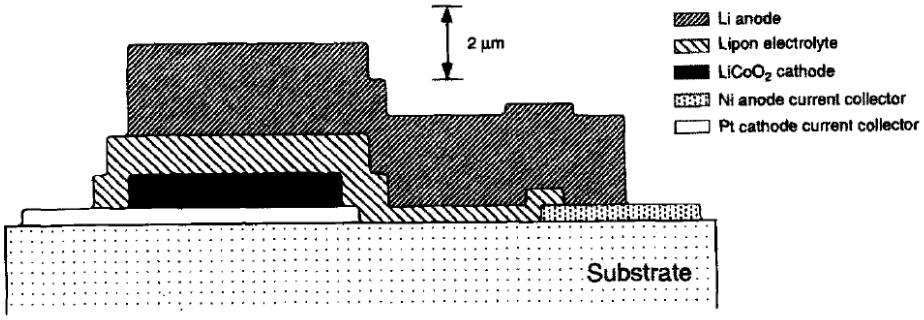

Figure 1.7 Cross-sectional schematic of an all-solid-state battery using $LiCoO_2$ as cathode, LiPON as electrolyte, and lithium as the anode [6]

1.3.1 Radio Frequency Mangetron Sputtering

Radio frequency (RF) magnetron sputtering deposition is a physical vapor deposition process where gas atoms are ionized by an alternating voltage in the radio frequency range. The plasma formed by ionized gas atoms and electrons are confined near a target by magnets. When gas ions collide with the target, target material is ejected and deposit on the substrate. Usually the process is conducted with careful control of gas pressure in the range of mTorrs. Radio frequency alternating voltage allows dielectrics and oxides to be used as target material due to build up of electric charge when a constant DC voltage is applied. Therefore, lithium ion battery electrode materials such as $LiCoO_2$, and silicon can be deposited along with electrolyte materials such as LiPON. Figure 1.8 shows a schematic of the RF magnetron sputtering chamber.

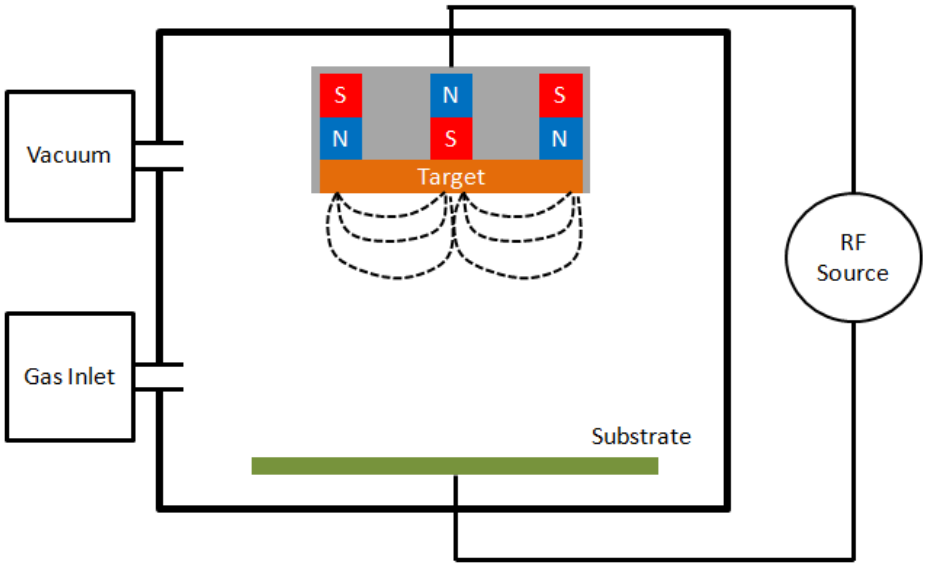

Figure 1.8 Schematic of a RF magnetron sputtering chamber.

Chapter 2. Background

2.1. Lithium Ion Solid State Electrolyte Thin Films

Lithium ion solid state electrolyte is the most important component in the functioning of a lithium ion thin film battery. It allows ionic transport between the cathode and anode thin films and should be stable against both electrodes. Lithium phosphorus oxynitride (LiPON) thin films deposited by RF magnetron sputtering satisfy multiple requirements of solid state electrolyte thin films needed to be useful in a thin film battery. It has an ionic conductivity of 2 x 10^{-6} S/cm, is stable against lithium metal, and has a wide 5.5 V stability window [5, 7]. LiPON thin films are deposited by sputtering Li_3PO_4 in pure N_2 gas which results in a film composition of $Li_{3.3}PO_{3.9}N_{0.17}$ determined through PIGE measurements. The introduction of nitrogen into lithium phosphate not only increased its ionic conductivity by 30 fold, but is also crucial in stabilizing the electrolyte film against lithium metal. The increase in ionic conductivity is believed to be the result of change in the structure of the amorphous thin film from one consisting of PO_4^{3-}, $P_2O_7^{4-}$, $P_3O_{10}^{5-}$ monomer and linear chain polymers to a cross linked structure with nitrogen as the cross link center. This structural change is shown in Figure 2.1. The stability of LiPON against lithium metal is thought to be caused by the formation of a thin Li_3N passivation layer from LiPON upon contact with lithium. This is confirmed through in situ XPS studies and theoretical computations [8-10]. While other solid state electrolytes such as lithium lanthanum titanate, lithium vanadium silicate, and lithium lanthanum zirconate exist, they will not be covered within the scope of this thesis.

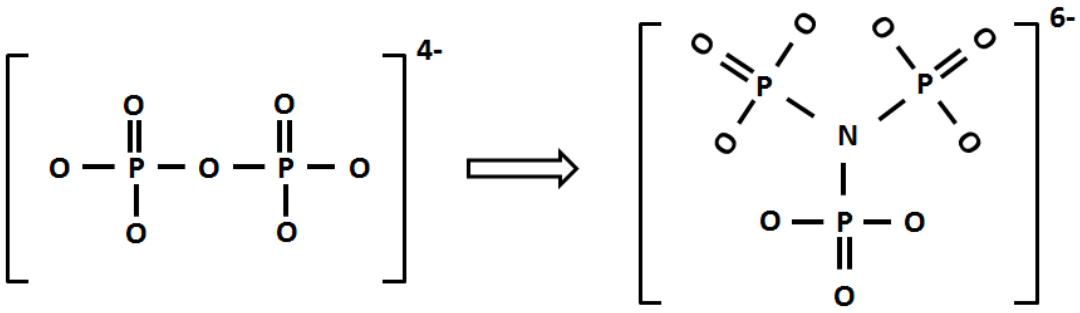

Figure 2.1 Transition from linear phosphate linear chain structure to a nitrogen center cross linked chain structure hypothesized in LiPON electrolyte which would increase the ionic conductivity

2.2. Lithium Ion Cathode Thin Films

Lithium cobalt oxide ($LiCoO_2$) is one of the first lithium ion cathode materials used in a full commercial lithium ion battery cell manufactured by Sony Inc. It was first discovered by Mizushima et al. at Oxford university under Professor John Goodenough in 1980 [11]. $LiCoO_2$ is a member of the lithium transition metal oxide ($LiMO_2$, where M = V, Mn, Co, Ni) material series with a layered rock-salt structure. This structure is based on a close-packed network of oxygen atoms with the Li^+ and M^{3+} ions ordering on alternating (111) planes of the cubic rocksalt structure. The ordering of positive ions causes a distortion of the cubic lattice to a hexagonal symmetry (R-3m) with ABCABC stacking of the oxygen planes [12]. A schematic diagram of the crystal structure of $LiCoO_2$ is shown in Figure 2.2. During electrochemical delithiation, several phase transformations were thought to occur. For $0.75 < x < 0.93$ in Li_xCoO_2, a first order phase transition is observed between two hexagonal phases with different c-lattice parameters due to repulsion between the oxygen layers. Near $x = 0.5$, there is an additional phase transition to a monoclinic unit

cell with lithium ordering [12, 13]. Figure 2.3 shows an overall phase diagram of $LiCoO_2$ electrochemical delithiation.

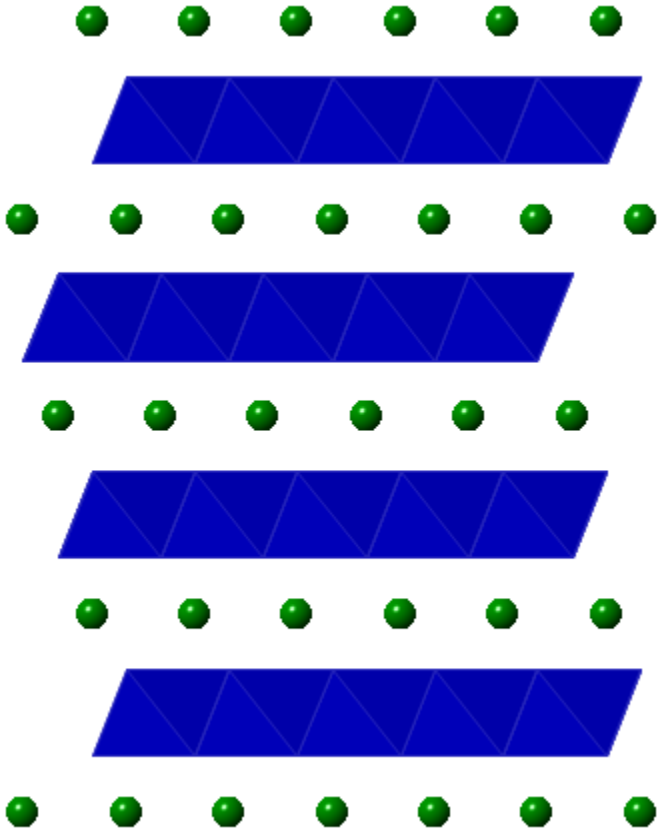

Figure 2.2 Crystal structure of $LiCoO_2$ where cobalt octahedral are shown in blue and lithium ions are shown in green. Cobalt ions and lithium ions occupy alternating layers separated by oxygen planes with ABCABC stacking.

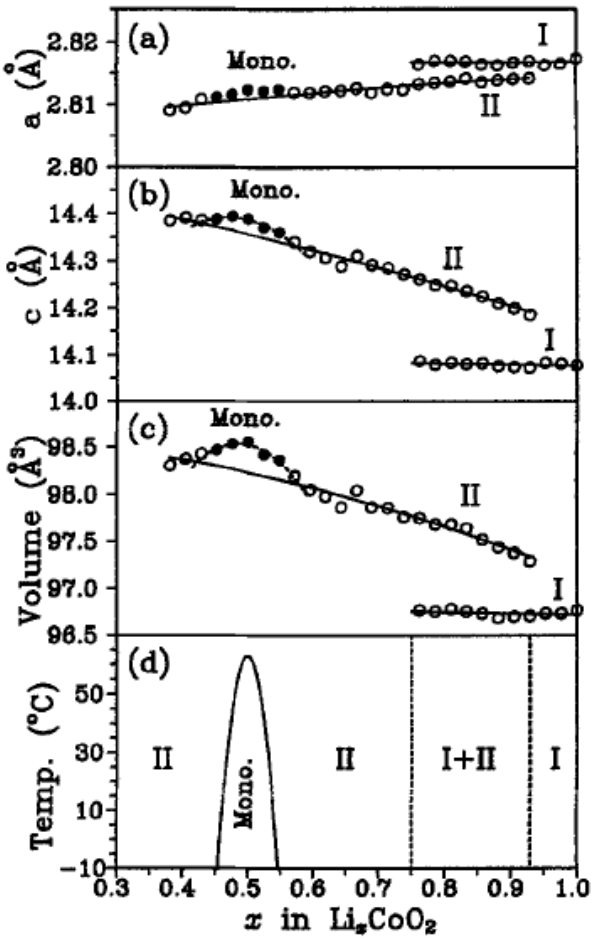

Figure 2.3 Unit cell constants a (a), c (b), and cell volume (c) as a function of lithium concentration x in Li_xCoO_2. Combined with the electrochemical results, (a), (b), and (c) determine a global phase diagram (d) for Li_xCoO_2 [12]

Other than conventional solid state synthesis, $LiCoO_2$ can also be deposited as a thin film using RF magnetron sputtering. In Wang et al. [6], mixtures of Ar and O_2 in a 3:1 ratio was used to sputter a $LiCoO_2$ target at 50W. Afterwards, the as-deposited thin films were then heated in air at a rate of 5 °C/min, held at either 500 or 700 °C for 2 hours, and finally cooled to room temperature at a rate of 1 °C/min. It is necessary to heat the as-deposited film to 700 °C; otherwise, the films will not be crystalline and do not exhibit proper electrochemical activity.

2.3. Lithium Ion Anode Thin Films

Silicon is one of the most promising anode materials for lithium ion batteries. The lithiation of silicon proceeds through an alloying reaction to a theoretical maximum composition of $Li_{22}Si_5$ which corresponds to a specific capacity of 4200 mAh/g compared to fully lithiated graphite which has a specific capacity of 372 mAh/g [14, 15]. During room temperature electrochemical cycling, it is shown that the terminal phase of lithiated silicon actually is a metastable $Li_{15}Si_4$ phase which crystallizes at room temperature [16]. Due to such significant lithiation however, large volume changes occur which cause rapid decay of the capacity. The decay mechanism is thought to be a combination of mechanical fracture leading to pulverization and loss of active material and constant side reactions on surfaces new materials exposed after contraction of the anode material [15].

Silicon anode can also be deposited as a thin film through various vacuum deposition methods such as thermal evaporation and RF-magnetron sputtering. Takamura et al. deposited 50 nm thin films of silicon by thermal evaporation and demonstrated stable high specific capacities of 3600 mAh/g at 2C rate for 200 cycles corresponding to maximum lithiation of $Li_{15}Si_4$ phase [17]. However, thicker 300-440 nm silicon films provided only about ~2000 mAh/g at 1C rate with decreasing retention. It was later shown by Li et al. that silicon films thicker than a critical thickness of 100 nm will form cracks in the film after repeated cycling causing loss of capacity (Figure 2.4) [18]. Silicon thin film anodes would be readily applied in an all-solid-state lithium ion thin film battery to study the effects of interfacial phenomena at the anode-electrolyte interface and its volumetric expansion during lithiation.

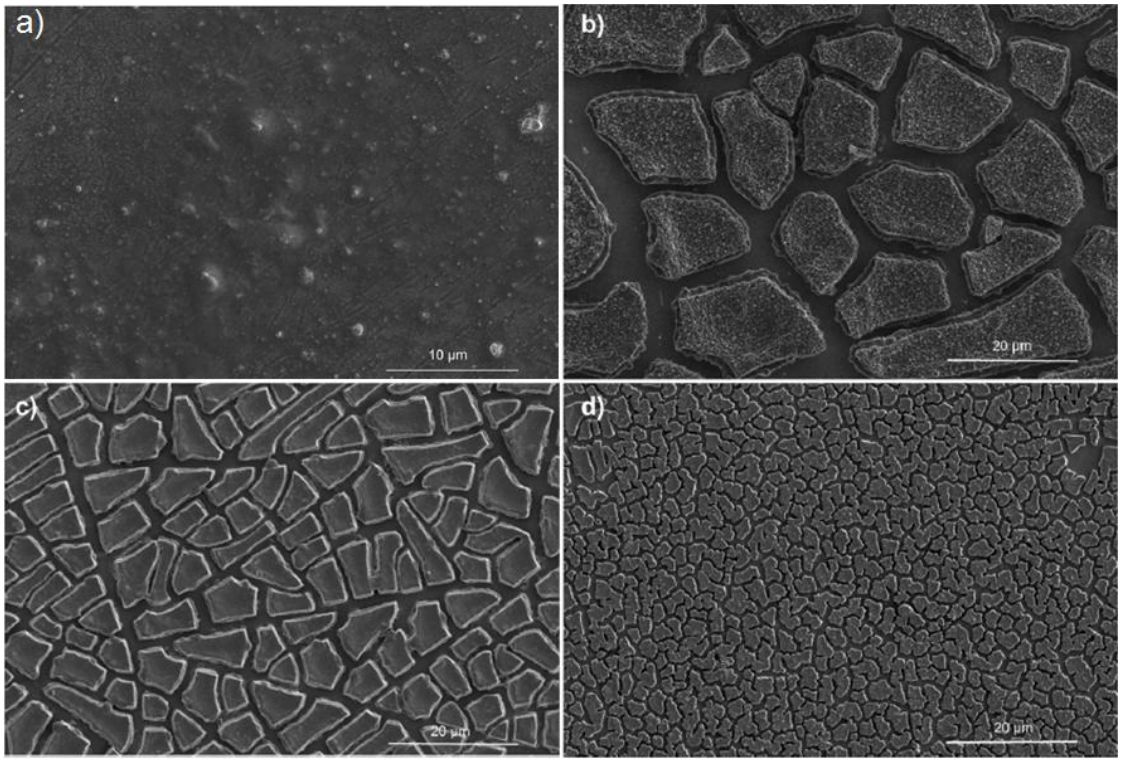

Figure 2.4 SEM images of cycled silicon thin films of various thicknesses after 10 cycles. a) 100nm thick, b) 1000nm thick, c) 500nm thick, and d) 200nm thick. [18]

Finally, lithium metal can also be easily deposited through thermal evaporation method. With a low melting point of 180.5 °C, lithium can be deposited at a rate of about 15 µm/hour in a titanium crucible. Lithium metal was used as the anode in earlier all-solid-state thin film batteries, although exposure to atmosphere must be carefully controlled and an encapsulation layer is usually used [6, 19, 20].

Chapter 3. Advanced Microscopy Techniques

In order to characterize material properties at a high level, highly specialized analytical techniques are necessary. These techniques allow the researcher to fabricate samples at the nanoscale and probe structural, chemical, and electronic bonding information that has not been previously accessible. In this thesis, the focus will be on two major techniques: Focused Ion Beam Microscopy and Transmission Electron Microscopy. Firstly, focused ion beam microscopy is a fairly recent research methodology where gallium ion beams are used to image samples, and more importantly to nanofabricate samples for characterization. Secondly, transmission electron microscopy is a highly advanced analytical tool aimed at characterization with atomic resolution of materials coupled with spectroscopic analysis of chemical composition and bonding. It is important to understand the mechanisms by which these microscopy techniques operate in order to properly interpret observed phenomena and cautiously avoid beam induced damages and artifacts.

3.1 Focused Ion Beam Microscopy

Focused Ion Beam Microscopy or FIB for short has become a heavily used technique in both industrial and academic fields. Starting from the 1980s, FIB instruments were used by the semiconductor industry as equipment for failure analysis and repair of integrated circuits. With the commercialization of FIB instruments, research laboratories began using it in research of various fields. In focused ion beam, a finely tuned beam of ions, usually gallium ions, is accelerated and focused by

electrostatic lenses and rastered over the desired sample area. The resulting ion-solid interactions not only produce secondary electron emissions that can be used for imaging, but also cause sputtering of the sample material that can be used for micromachining.

3.1.1 Principles of Focused Ion Beam

The capabilities of a focused ion beam begin at the ion source. Though there are many ion source technologies available, the most reliable and widely used ion source is the liquid-metal ion source (LMIS) [21]. There are a number of different types of LMIS sources such as In, Bi, Sn, and Au; however, Ga based sources are the most widely used due to low melting temperature (30 °C), low volatility, and low vapor pressure. The basic design of the ion source consists of a metal reservoir that contains a heating element to melt the metal source and a needle tip usually made of tungsten. During operation, molten metal such as liquid gallium flows from the reservoir to the needle tip (with an end radius of about 10 μm). Near the tip, a large negative potential between the needle and an extraction electrode generates an electric field of magnitude 10^{10} V/m. Due to the forces of electrostatics and surface tension, the liquid gallium forms a Taylor cone at the tip of the needle that has an approximate radius of 5 nm. The combination of a sharp tip and high electric field causes field emission of gallium ions to form an ion beam that can be focused by lenses in the ion beam column.

Most ion beam columns use two electrostatic lenses (a condenser and objective lens) to define the beam and then focus it on the sample. There are also additional

beam-defining apertures to select the beam diameter and current, deflection plates to raster the beam over the sample surface, and stigmation poles to ensure a spherical beam profile. Electrostatic lenses are used over electromagnetic lenses due to the high mass/charge ratio of the gallium ion. The electromagnetic lenses required for proper focusing of gallium ion beams would be too large to be built and used practically. Schematics of the ion beam and ion source compared to e-beam sources used in SEM are shown in Figure 3.1. Most ion beams are also fitted with an additional e-beam source to create a dual beam system where the sample can be analyzed by both beams.

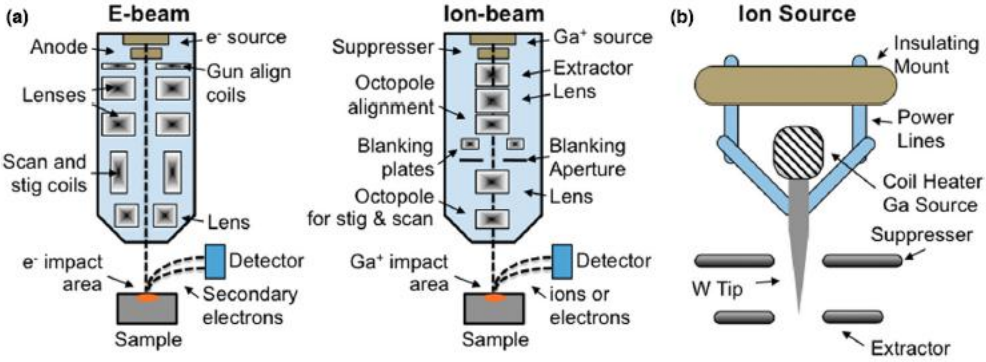

Figure 3.1 Schematic diagram of the dual beam FIB/SEM systems [22]

3.1.2 Focused Ion Beam Imaging

After an ion collides with a mass of solid material, ion-solid interactions are the main resulting phenomena. During and after the initial collision, the incident ion undergoes a variety of elastic and inelastic processes such as:

- Ion reflection and backscattering
- Electron emission
- Electromagnetic radiation
- Atomic sputtering and ion emission

- Sample damage and heating

After the incident ion has lost all of its kinetic energy, it will be implanted within the sample material surface. During elastic collisions, the incident ion transfers translational energy to atoms of the sample material causing displacement, sputtering, and potential secondary collisions where the displaced atom has enough energy to displace additional atoms. For a gallium ion with 30 keV of energy, an interaction volume of approximately 10 x 5 x 5 nm^3 to100 x 50 x 50 nm^3 is expected depending on sample density. During inelastic collisions, energy is lost to electrons that are ionized and emitted as secondary electrons or electromagnetic radiation. These processes are summarized in Figure 3.2.

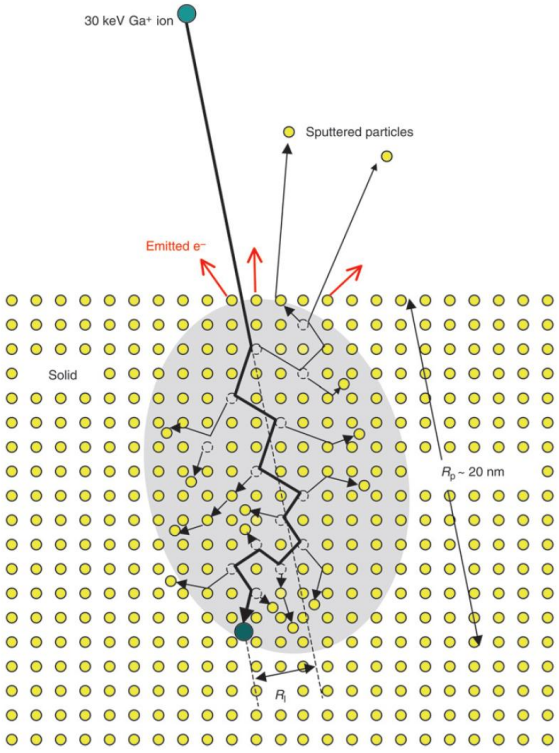

Figure 3.2 Schematic of a series of collisions generated by a 30 keV Ga^+ ion on a crystalline lattice. [21]

Focused Ion Beam imaging is done by detecting the secondary electrons that are produced by the inelastic collisions of the incident ion and sputtered atoms. Usually 1-10 ion induced secondary electrons are provided per incoming 5-30 keV Ga^+ ion. Ion beams are not as finely focused as electron beams leading to lower resolution; however, ion induced secondary electrons offer various different contrast mechanisms that are not available for electron induced secondary electrons. This difference is clearly shown in Figure 3.3, where the secondary electron image resulting from an electron beam is compared to the image resulting from an ion beam.

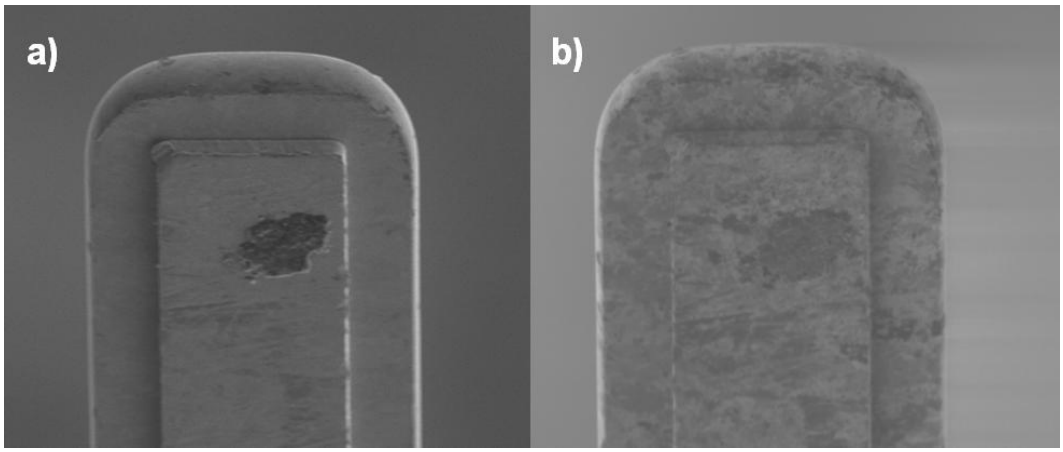

Figure 3.3 Secondary electron image induced by (a) electron beam and (b) ion beam on a copper grid.

The main difference between electron beam and ion beam induced secondary electrons is the “channeling contrast” due to crystal orientation of sample material. Additionally, ion beam induced secondary electrons also provide contrast due to surface morphology and differences in material. The different contrast mechanisms are shown in Figure 3.4. When certain crystal planes of the crystalline sample material line up perfectly with the ion beam, less ion-solid interactions occur on the surface of

the material leading to fewer secondary electrons emitted. However, when the ion beam has to collide through various atoms of the crystal planes that happen to be in the direction of velocity, there will be much higher chances of ion-solid interactions leading to higher number of electrons emitted.

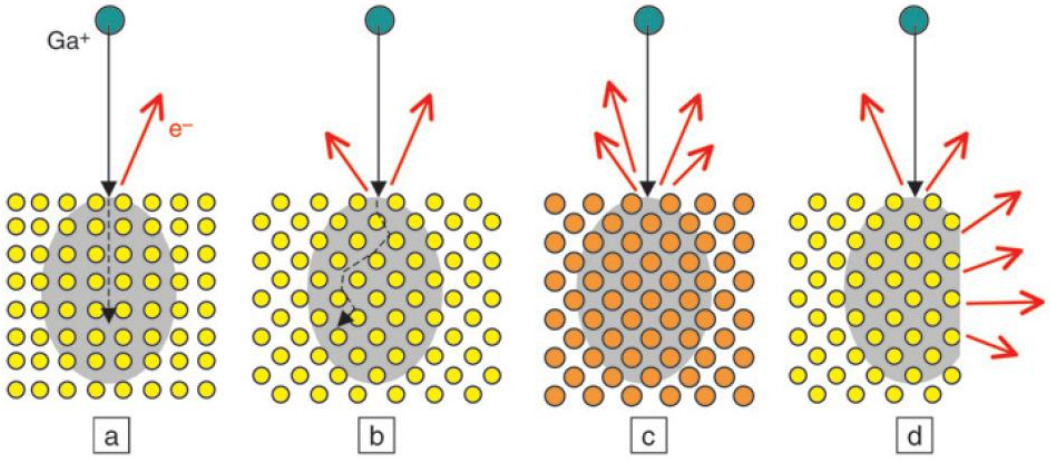

Figure 3.4 Schematics showing the influence of (a), (b) crystal orientation, (c) atomic mass, and (d) surface geometry. The atoms in (c) have a higher Z-number than atoms in (a), (b), and (d). [21]

3.1.3 Focused Ion Beam Milling and Deposition

Ion beam milling is usually divided into two categories: unassisted milling and assisted milling. In unassisted milling, the elastic collisions sputter away sample material from the surface. The milling rate is dependent on the material's molecular weight and density. The milling rate is linearly proportional to the beam current and typical milling rates are shown in Table 3.1 [23].

Table 3.1 Sputter yield and milling rate of different materials [23]

Material	Sputter Yield (Atom/Ion)	Milling Rate ($\mu m^3/nC$)
Gold (Au)	18	2.55
Chromium (Cr)	3.5	0.28
Silicon (Si/SiO_2)	2.1 (Si)	0.25 (Si) / 0.30 (SiO_2)
Silicon Nitride (Si_3N_4)	0.5	0.21

In assisted milling, additional gases are introduced into the FIB system to chemically assist the sputtering of material. This process allows the ion beam to mill faster and avoids re-deposition of sputtered material [24-26]. In chemically assisted milling of silicon/silicon dioxide, xenon difluoride gas is flowed into the FIB chamber by an injection needle. The powerful fluorinating agent is adsorbed onto the sample's surface, and reacts with the sputtered silicon atoms to form silicon tetrafluoride gas and xenon gas which desorb from the sample surface easily. This reaction is summarized in equation 3.1 and the overall process is shown in Figure 3.5.

$$SiO_2\ (s) + 2XeF_2\ (g) \rightarrow SiF_4\ (g) + O_2\ (g) + 2Xe\ (g) \qquad \textbf{(Equation 3.1)}$$

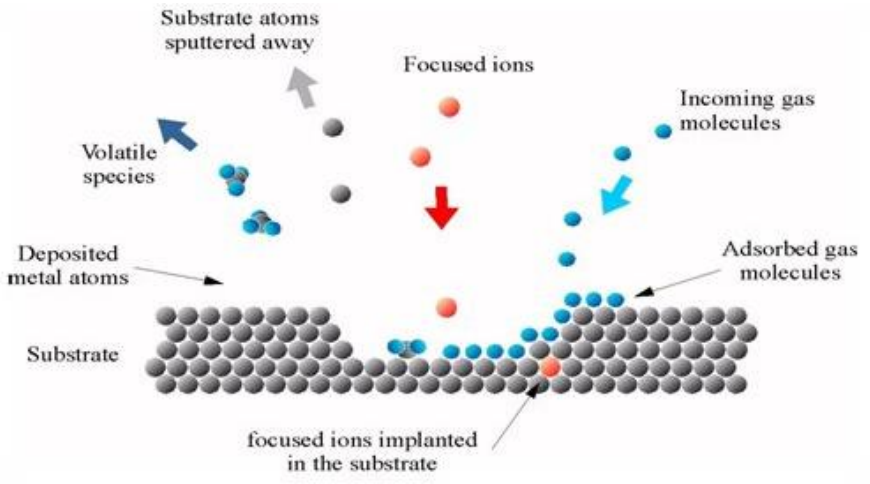

Figure 3.5 Schematic diagram of chemically assisted ion beam etching [27]

In addition to the use of certain gases for assisted milling, particular gas precursors with metal ions can be used for ion beam induced deposition of material for various uses. FIB-assisted chemical vapor deposition occurs when a gas precursor, such as methylcyclopentadienyl (trimethyl) platinum $(CH_3)_3(CH_3C_pPt)$, is absorbed onto the sample surface and bombarded by the incoming gallium ions. Secondary electrons produced by electron beam and ion beam striking the sample surface results in the reduction of the metal ion and the subsequent deposition of metallic element. The best current range used for ion beam deposition is usually in the range of 2 – 6 $pA/\mu m^2$. This process is demonstrated in Figure 3.6.

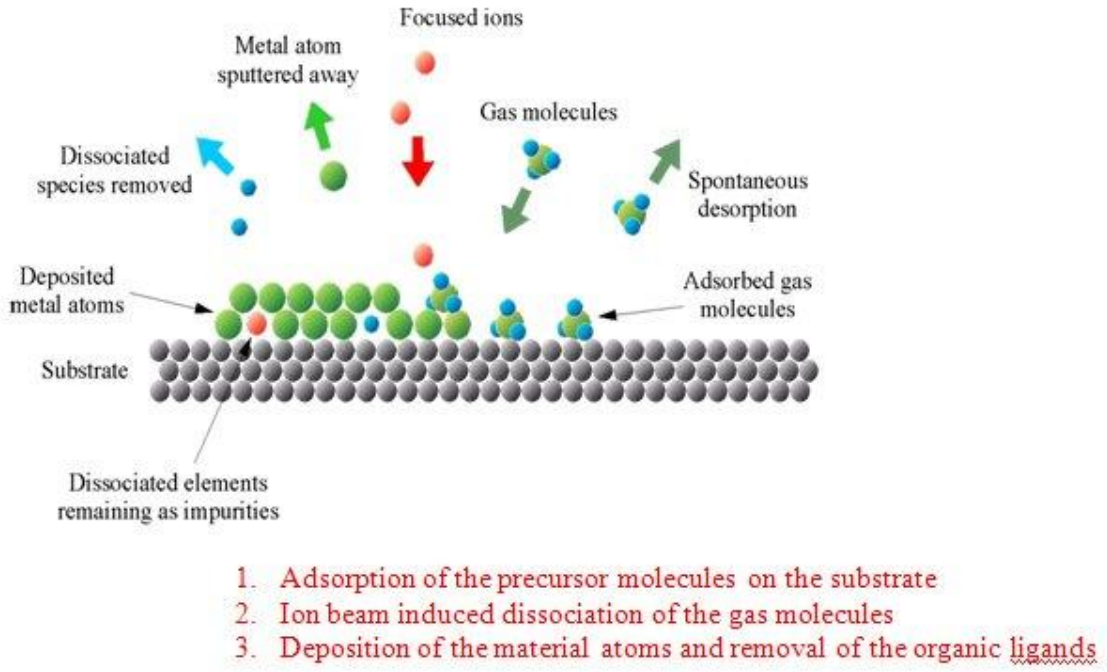

Figure 3.6 Schematic diagram of ion beam deposition [27]

3.2 Transmission Electron Microscopy

Transmission Electron Microscopy or TEM for short is a powerful analytical tool used by material scientists to study the dynamic structural, compositional, and electronic bonding changes that occur within the material of interest. It is a microscopy technique in which a beam of electrons is emitted from a source, accelerated by a high voltage field (200-300kV), and refined by multiple electromagnetic lenses that focus the beam. An image is then formed when the beam of electrons is passed through an ultra thin sample (100 nm thickness), magnified, and detected by digital CCD cameras.

Optical microscopes are limited in their ability to resolve objects smaller than a few hundred nanometers by the wavelength of visible light. Development of UV microscopes only increased resolving power by a factor of two and introduced additional technical difficulties. In 1928, a team of PhD students including Ernst Ruska and Bodo von Borries at the Technological University of Berlin worked on advances to a Cathode Ray Oscilloscope design under the supervision of professor Adolf Matthias. Once they applied de Broglie's hypothesis of wave-matter duality, they realized that electrons would have a much smaller wavelength than visible light and could be used to enable resolving power capable of distinguishing atoms. The wavelength of an electron can be calculated with relativistic corrections by Equation 3.1. For an electron accelerated by a 200 kV field, its de Broglie wavelength is 2.5 picometers providing enough resolving power for atomic bonds.

$$\lambda_e \approx \frac{h}{\sqrt{2m_eE(1+\frac{E}{2m_ec^2})}} \qquad (Eq.3.1)$$

3.2.1 Principles of Transmission Electron Microscopy

The transmission electron microscope is a highly complex instrument composed of multiple components. Generally, it includes a column of vacuum system for which the electrons can travel, an electron source, a series of electromagnetic lenses to refine, shape, and magnify the electron image, and finally detectors to capture the image. Inside the electron beam column, pressures of at least 10^{-7} Torr need to be maintained to create an environment with minimal electron gas collisions and to prevent electrical arcs at the TEM cathode at high voltages.

The electron source consists of several components to produce a beam of highly energized electrons. Electrons can be generated through two types of mechanism, thermionic emission and field emission. In thermionic emission, a filament with high melting point and low work function such as tungsten or lanthanum hexaboride is heated to a temperature where the thermal energy of the electrons are higher than its work function leading to emission. Then, the emitted electrons are converged by a negatively charged Wehnelt Cylinder, at the expanse of less electrons emitted, and finally accelerated to a positively charged anode. In field emission, a very strong electric field 10^{9} V/m is used to extract electrons from a metal filament and then accelerated further to the full potential. Field emission electrons produce a more intense electron beam but require higher vacuum columns on the order of 10^{-10} Torr.

After the electrons are generated and accelerated to the set high voltage, they are focused by several electromagnetic lenses that act in the same principle as an optical convex lens. Two lenses after the electron source called condenser lenses shape and refine the electron beam before the electron beam contact the sample. The

objective lens forms an inverted initial image which is then magnified by an intermediate lens and two projector lenses. Figure 3.7 shows a schematic of the TEM column with all the components.

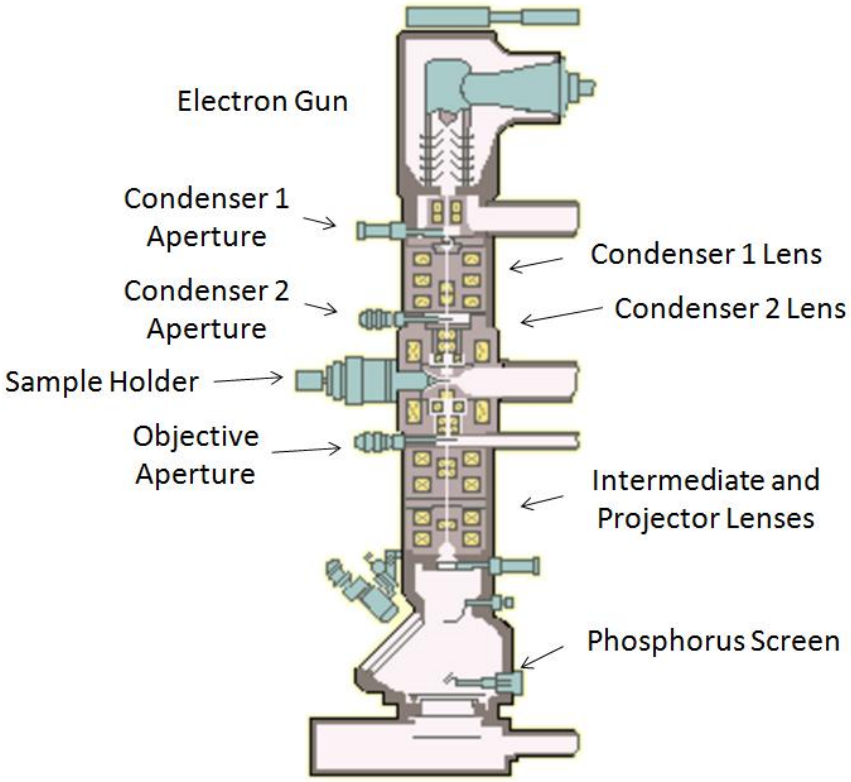

Figure 3.7 Schematic of the TEM column including all its components.

The interactions of the electrons with the sample causes contrast changes in the image formed by the electrons. This contrast provides an image of the sample and is affected by various factors such as sample thickness, sample Z-number, crystallinity, and crystal orientation. Additionally, when the back focal plane is focused on the imaging plane, electron diffraction patterns of the sample can be captured as well.

3.2.2 Scanning Transmission Electron Microscopy

A TEM can also be modified with deflection coils to raster the focused beam across the sample to form an image when combined with appropriate detectors. This mode of operation is called Scanning Transmission Electron Microscopy (STEM). Schematic ray diagrams of TEM and STEM modes are shown in Figure 3.8.

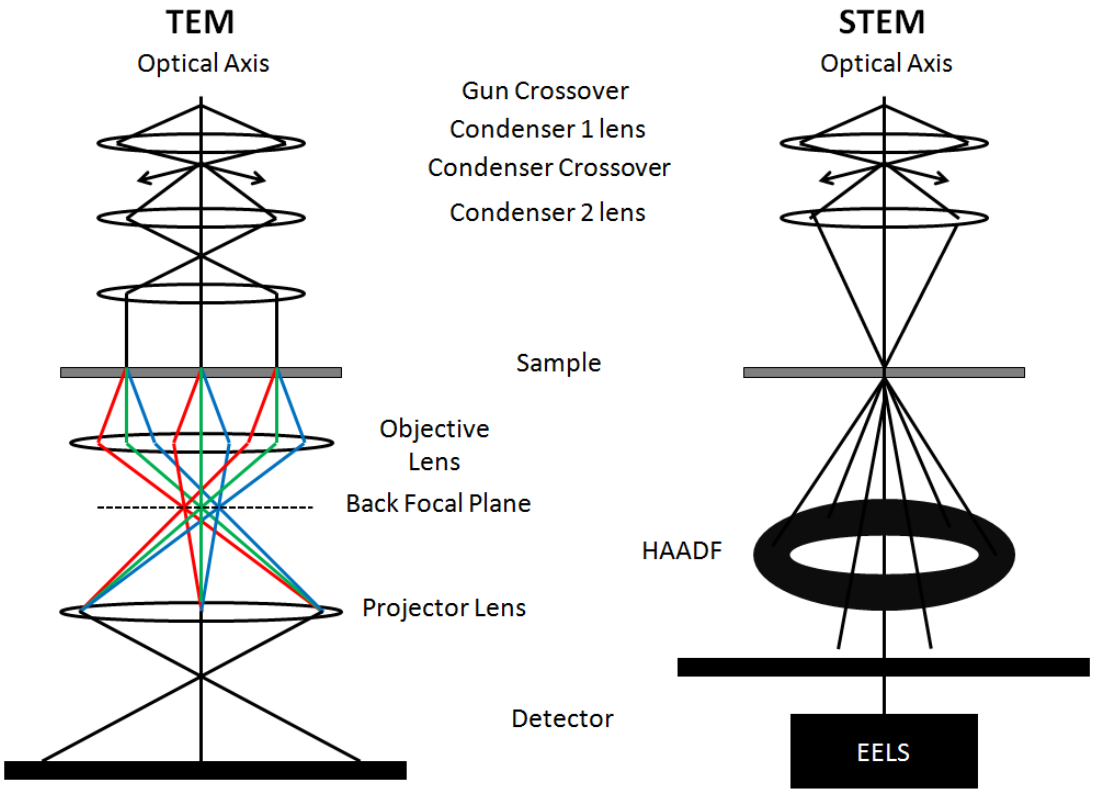

Figure 3.8 Ray Diagrams of TEM and STEM

In TEM mode, a broad beam interacts with the specimen. Elastic scattering is used in the formation of an images by electrons transmitted through the sample. Diffraction contrast dominates in low and medium magnification while phase contrast dominates high-resolution images (HRTEM). In TEM mode, magnification is

determined by the imaging lenses. In STEM, a focused beam (or a probe) is used to illuminate the sample. For example, the probe size can be around ~0.2nm in a JEOL 2100F. Such a small probe is used to localize the signals coming from the specimen, i.e. obtain high spatial resolution. To form a STEM image, the beam is scanned on the sample, parallel to the optic axis. The scattered beam can be collected by an annular detector to form dark fields (ADF) STEM image, and the direct beam can be detected by a BF detector to form BF-STEM images. When the inner angle of an annular detector is more than three times larger than the objective aperture, also called High Angle Annular Dark Field (HAADF) detector, the intensity of the image can be directly correlated to atomic number Z (Z-contrast). Thus, HAAD-FSTEM involves much simpler interpretation than HRTEM. All the imaging modes in STEM can perform high resolution lattice imaging. The magnification of the STEM images is not controlled by the lenses of the microscope, but the scan dimensions on the specimen. Due to this scanning process, it takes longer to acquire a STEM image than a TEM image. As a result, stability is crucial in STEM observation.

In this thesis, only low to medium resolution TEM and selected area electron diffraction was used in TEM mode. A lot of the characterization and data analysis was carried out in STEM mode. More specifically, STEM-HAADF imaging and electron energy loss spectroscopy (EELS) were used in STEM mode.

3.2.3 Electron Energy Loss Spectroscopy

When high energy electrons interact with the atoms of the sample, a vast majority of the electrons undergo elastic scattering or do not interact at all. However, some electrons will interact with the sample inelastically and in the process lose kinetic energy. This energy loss can be used to provide compositional and electronic bonding information about the characterized sample and be quantified using electron energy loss spectroscopy. There are various mechanisms by which incident electrons can interact with the sample, but can be mainly divided into two components: low loss energy spectra and high loss (also known as core loss) energy spectra.

The low loss energy spectra consist of electrons that have lost approximately 0 to 150 eV of kinetic energy after interacting with the sample. They are dominated by a zero loss peak which consists of electrons that underwent elastic scattering and have not lost any kinetic energy. When the primary electrons interact with the collective excitations of valence electrons, plasmon peaks form. Finally, primary electrons can also excite an electron from the inner or core energy states to an unoccupied state in the valence band. For light elements such as lithium, the transition from K-shell to the valence shell only requires 55 eV. The interpretation of chemical and electronic bonding information can be complicated in this region to the overlapping nature of all these possible signals.

In the high loss energy spectra region, electrons have lost significant kinetic energy after promoting an inner or core shell electron (K, L, or M) to the valence band. These transitions require specific ionization energies leading to ionization edges in the electron energy loss spectra with distinct energy values. These energy values

can be used to identify the particular shell transitions and atomic number. The intensity of these ionization edges can be directly related to the amount of element present and be used to quantify the composition. It is particularly useful for the detection of light elements such as lithium because energy dispersion x-ray spectroscopy cannot detect light elements.

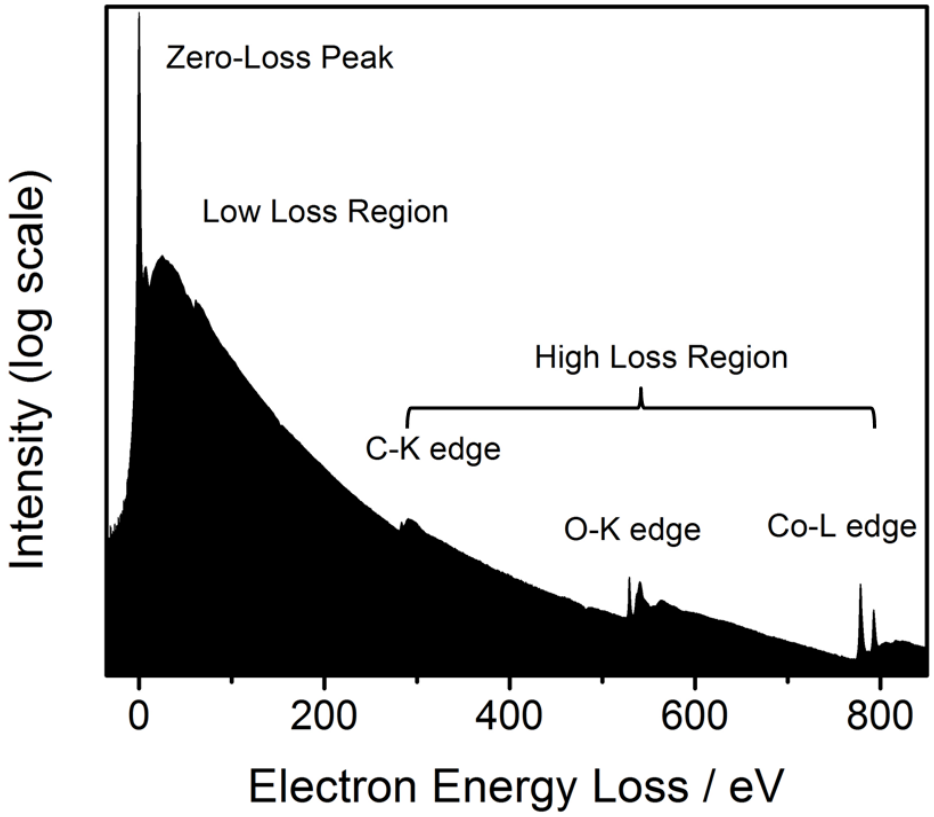

Figure 3.9 Electron energy loss spectrum of $LiCoO_2$ demonstrating typical features of a zero loss peak, low loss region and high loss region

In addition to elemental information, fluctuations of intensity after the initial ionization edge provide information about the electronic bonding of the probed atom such as coordination, oxidation state, and type of bonding. This region of fluctuations is designated as energy loss near edge structure (ELNES) and is closely tied with the

density of states (DOS) of the unoccupied states of the probed atom. These unfilled energy levels are a function of the overall electron distribution due to the atom and its neighbors. Thus, the energy loss of the incident electrons carries the information on the distribution of the unfilled states.

These fluctuations are especially distinctive for the L_3 and L_2 edges of transition metals and can be used to obtain information about the oxidation state and coordination of transition metals with their neighboring atoms such as oxygen anions. The L_3 and L_2 edges are two ionization edges that result from electron transition from occupied 2p orbital to unoccupied 3d orbital. In the case of the 2p orbital, the electronic spin ($\pm$1/2) can couple with the angular momentum (l = 1) to give a total quantum number j of 3/2 (1+1/2) and 1/2 (1-1/2). The $2p^{3/2}$ transition is denoted as L_3 and has a lower binding energy than the $2p^{1/2}$ transition which is denoted as L_2. Each transition has a degeneracy of 2j + 1, implying an ideal 2:1 ratio of L_3/L_2 peaks. However, the actual ratio varies wildly in 3d transition metals due to spin-spin coupling effects [28-30]. These variations can be used to identify the occupation number of the 3d orbitals and hence the oxidation state of the transition metal. This relationship has been investigated for several transition metal element systems such as Fe, Mn, Co, and Cr and a few databases have been built up [31-37]. Finally, the effective charge of the transition metal can also cause a shift in the binding energy of the various electronic states. These shifts then lead to chemical shifts of the edge onset. For example, the L_3 onset of Co^{2+} has a lower energy than the L_3 onset of Co^{3+}. In Figure 3.10, the Co-L edges are shown for CoO, Co_3O_4, and $LiCoO_2$. The gradual

shift of the Co-L edge to a lower energy can be observed from Co^{3+} in LCO and Co^{2+} in CoO. In addition, the L_3/L_2 ratio also changes depending on oxidation state.

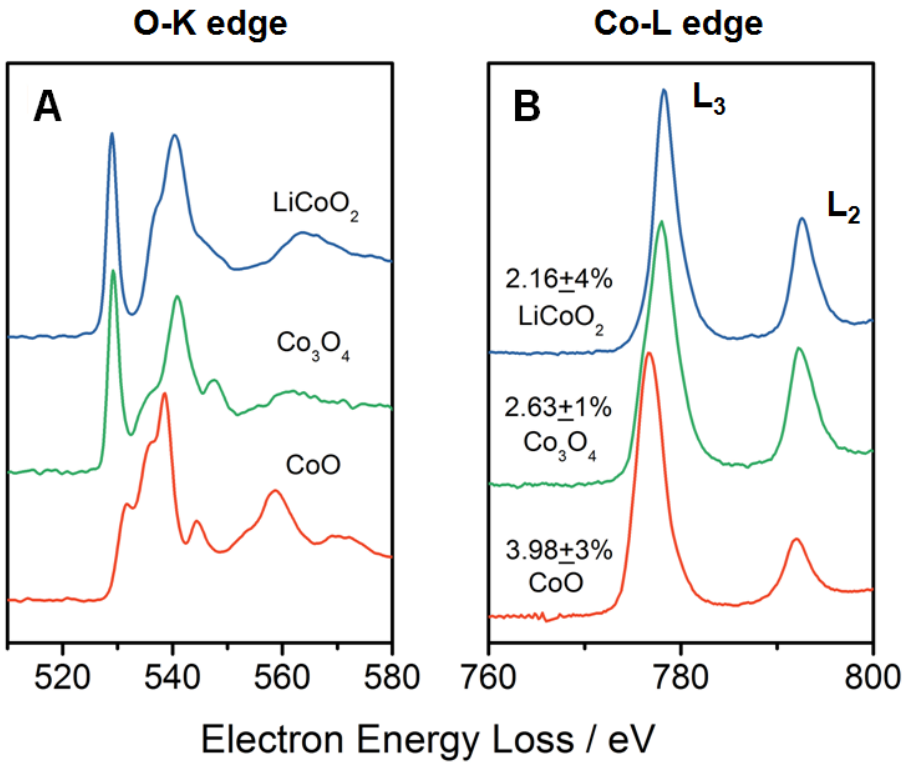

Figure 3.10 Electron energy loss spectra taken from CoO, Co_3O_4, $LiCoO_2$ sample standards a) O-K edge and b) Co-L edge

Chapter 4. Optimization of FIB Fabrication and TEM Characterization

This chapter focuses on the recent development and optimization of analytical electron microscopy to understand the dynamic changes in the bulk and interfaces of electrodes and electrolytes within all-solid-state batteries. Three major aspects are covered: 1) design and fabrication of all-solid-state batteries that remain functional after careful focused ion beam (FIB) processing; 2) enablement of *in situ* biasing in both FIB/SEM and transmission electron microscope and/or scanning transmission electron microscope (TEM/STEM); and 3) development of the fundamental understanding of the dynamic chemical and electronic processes at the solid/solid interfaces of electrode/electrolyte by high resolution imaging and electron energy loss spectroscopy (EELS). Our goal is to apply analytical microscopy to gain new insights that can help us make significant inroads towards understanding the basic science of ion transport, charge transfer and related phase transformations in electrochemical systems at the nanometer scale.

4.1 Introduction

In situ electrochemical operation in the ultra-high vacuum column of a TEM has been pursued by two major strategies. In one strategy, a "nano-battery" is fabricated from an all-solid-state thin film battery using a focused ion beam (FIB). The electrolyte is either polymer based or ceramic based without any liquid components. The second strategy involves liquid electrolytes. Although the latter approach more closely resembles the actual operating conditions of the widely-used functional

battery, the extreme volatility of the organic electrolytes presents a significant challenge for designing an *in situ* cell suitable for the vacuum environment of the TEM. Ionic liquids can used to replace the conventional polycarbonate based electrolytes without the tedious silicon nitride window sealing cell setup. More recently, it has been reported that Li_2O can be used as a low-voltage electrolyte for lithiation in Si/Sn/Ge and FeF_2 electrode materials.[38-41] However, Li_2O is unstable upon high voltage charging. Therefore, it would not be suitable for high voltage delithiation of transition metal oxides, a common class of materials used as the positive electrode in lithium ion batteries.

Significant progress has been made in the past few years on the development of *in situ* electron microscopy for probing nano-scale electrochemistry. Both strategies mentioned above are pursued in the research community. Yamamoto et al. reported the dynamic visualization of electric potential in an all solid state battery by electron holography and EELS.[42] They emphasized the need for thicker electrolyte while preparing the cross-section using FIB to avoid short-circuiting during the biasing process. Their experimental set-up consisted of an electrolyte that was too thick (90 μm) and only a smaller portion of the cross-section was thinned down to be observed in the TEM while the whole stack was biased. In spite of the *in situ* observation in TEM, the problem with this configuration was that the thinner part (~ 60 nm) observed in TEM had higher resistance than other parts of the cross-section and led to very minimal electrochemical activity. More recently, there has been tremendous progress on *in situ* studies using Si nanowires,[38, 43] Ge nanowires,[40] and SnO_2 nanowires[44, 45] as anode materials. Ionic liquid was mostly used as electrolyte. A

schematic of the experimental set-up is shown in Figure 4.1. With the similar setup, Feng et al.[39] successfully used Li_2O as the electrolyte and lithiated FeF_2, a conversion type electrode material. A novel "necking" phenomena was revealed in the nano-composite materials by this *in situ* TEM technique.

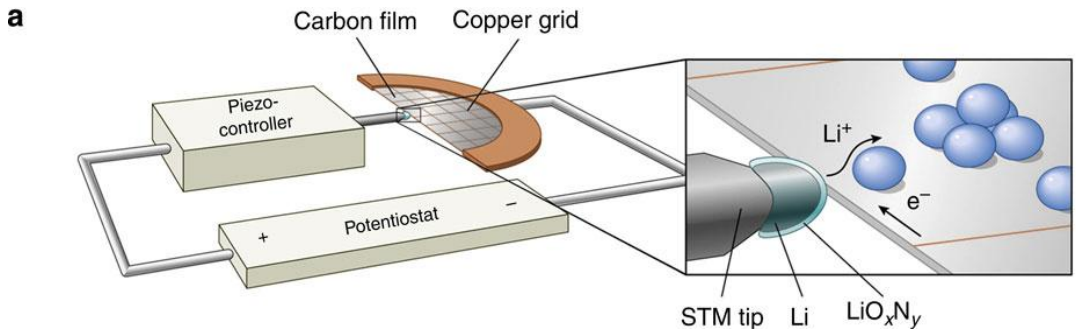

Figure 4.1 From [39], schematic of the electrochemical cell used for *in situ* TEM measurements. (b) Time-lapse images from a collection of particles that react with lithium coming from the lower right. The reaction proceeds immediately in region (I), but is delayed and absent in regions (II) and (III), respectively. Scale bar, 10 nm.

Despite the success of *in situ* biasing experiments of individual nanowires and nanoparticles, there are several drawbacks to the approach, such as:

1. The chemistry of individual nano-materials seems to be unique and generalizing the results to an electrochemically active system is debatable (particularly when the individual and ensemble effects of nano-materials are different).

2. Ionic liquid is of low vapor pressure, and use of IL in the UHV column may induce long-term damage to the microscopes.

3. Electrode/electrolyte interface is very important in energy storage devices, which cannot be addressed directly by these studies.

Considering the above points, our approach has unique advantages because our starting point is an electrochemically active solid-state battery stack. This type of all-solid-state sample can be used to study the interface effects *in situ* while monitoring electrochemical and structural changes with high spatial resolution. We demonstrate that the FIB processed cross-section is still electrochemically active and *in situ* TEM can be used as an advanced tool to monitor the electrode/electrolyte interface during the operation of the battery.

4.2 Focused Ion Beam (FIB) Fabrication and Electrochemical Biasing of Nano-Batteries

The eventual success of *in situ* analytical Transmission Electron Microscopy depends on the fabrication of less than 100nm thick all-solid-state lithium ion batteries that are electrochemically active. As one of the few methods capable of such fabrication, Focused Ion Beam (FIB) technique has been used for Transmission Electron Microscopy (TEM) specimen preparation and semiconductor circuit editing quite extensively.[46, 47] Major concerns with FIB have been the surface damage, re-deposition, and preferential sputtering due to high current density.[48, 49] Several articles on the FIB damage to materials during preparation of specimens have proposed possible methods to reduce this damage.[50-53] FIB fabrication of electrochemically functional all-solid-state nano-batteries depends on two main factors: limitation of structural damage caused by high ion beam current and avoidance of shorting caused by re-deposition during milling processes.

Using an all-solid-state battery with Si, LiPON, and $LiCoO_2$ as anode, electrolyte, and cathode respectively as the typical system, functional nano-batteries have been fabricated using a two-step procedure with a specific set of beam parameters. The successful preservation of electrochemical functionality depends on several parameters; most importantly, the ion beam current and the pixel dwell time. For typical FIB fabrications, beam energy and current are given more importance compared to pixel dwell time. Here we demonstrate that pixel dwell time to be a very important parameter. To reduce the fabrication time and damage induced by FIB, a two-step fabrication process was utilized. The first step is a high current ($\leq$ 2.8 nA) milling process followed by a low current (0.28 nA) cross-section cleaning process while maintaining the 30 kV incident beam. During the first step high current leads to a large amount of re-deposition across the stack and the second step cleans the cross-section. Figure 4.2 (a & b) shows the cross-section SEM images of the Si/LIPON/$LiCoO_2$ battery stack which clearly depicts the effect of this two-step fabrication process. High ion beam current (> 0.28 nA) during the surface cleaning process tends to heat the amorphous electrolyte and worsen re-deposition across the stack.

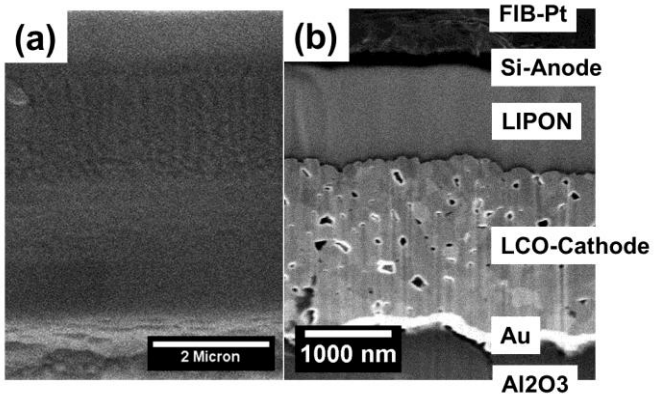

Figure 4.2 SEM images of the all-solid-state battery (effect of two-step fabrication process). a) After step one: milling process. b) After step two: cross-section cleaning [54]

The second important parameter is the pixel dwell time, defined as how long the ion beam dwells on each pixel during a scanning process. Higher dwell time also leads to heating and increasing re-deposition, causing loss of electrochemical activity of the battery stack. Figure 4.3 shows the effect of pixel dwell time on the electrochemical activity of a sputtered micro-battery stack fabricated by FIB. The stack was charged under constant current mode (typically with a current density of about 100 $\mu A/cm^2$) *in situ* in a FIB system. The normal size of the nano-batteries fabricated is a 2µm x 10µm rectangle with the thickness of the whole battery stack.

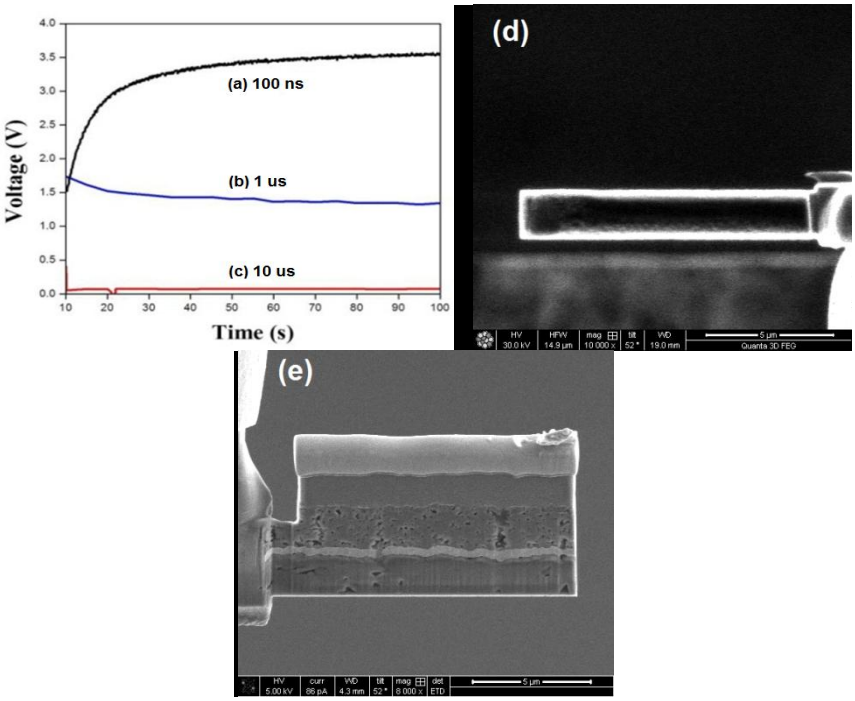

Figure 4.3 Electrochemical voltage profile of all-solid-state batteries fabricated by FIB. a) 100ns pixel dwell time, b) 1 µs pixel dwell time, c) 10 µs pixel dwell time. d and e) shows the typical dimensions of a nano-battery from top-view and side-view. [54]

In Figure 4.3 (a), the charging profile for a nano-battery fabricated using 100 µs pixel dwell time shows hardly any voltage, indicating shorting across the stack. Figure 4.3 (b) shows the charging curve for a nano-battery fabricated using 1 µs pixel dwell time, and the voltage was lower than the expected 3.6 V. Figure 4.3 (c) shows the charging profile for a nano-battery fabricated using 100 ns pixel dwell time and the voltage raised to 3.6 V. For all the three cases, the charging current density was 100 $\mu A/cm^2$. Nano-batteries fabricated using 100 ns pixel dwell time are highly consistent and repeatable with 3.6 V voltage plateau which agrees well with the voltage profile of macro-batteries in literature[55]. Subsequent to the successful nano-battery fabrication, we scaled down to fabricate even thinner nano-batteries.

The specific procedures of electrochemically biasing the batteries inside the FIB are fairly simple and straight forward. A micron slab consisting of the whole battery stack is lifted out of the all-solid-state thin film battery using typical TEM sample preparation procedures[46]. The liftout procedure must be conducted with the aforementioned maximum FIB current setting and pixel dwell time parameters. Once this sample is mounted on a typical OmniProbe copper grid for TEM samples via Pt-welding, a small cleaning cross section is used to expose the whole battery stack near the welding area. Afterwards, a second Pt-welding is used to connect the previous Pt-weld (which is connected to the Cu grid) to the exposed Au-bottom current collector. This ensures an electrical connection from the FIB stage to the cathode of the nano-battery. In order to isolate the top anode Silicon layer, cleaning cross sections are applied from a side-view to remove a portion of the battery down to the lithium cobalt oxide layer. Finally, the nano-battery is milled to the desired size by cleaning cross sections from the top view. The anode connection is made by physically contacting the Omniprobe micromanipulator to the top surface of the nano-battery. Most focused ion beam models will support outside electrical connections to the stage and omniprobe via electrical ports, hence establishing electrical connections from the nano-battery to an external battery cycler. Figure 4.4 demonstrates the procedures involved in the fabrication and biasing of a nano-battery.

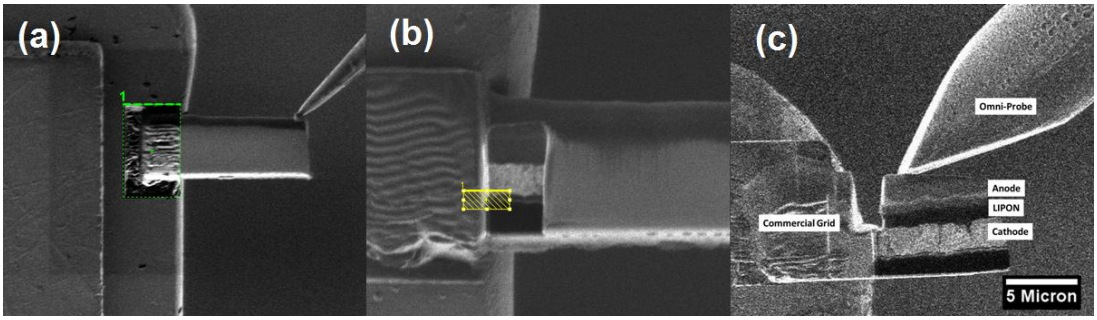

Figure 4.4 a) Mounting of nano-battery after the liftout. b) Cleaning cross section to expose battery layers and Pt-welding for electrical connection. c) Electrical contact to the nano-battery after cleaning the cross section.

4.3 Beam Damage Control in TEM/STEM

After the successful fabrication of nano-batteries with careful FIB parameter control, electron beam damage under scanning transmission electron microscopy (STEM) and electron energy loss spectroscopy (EELS) with a highly focused electron beam must be controlled and minimized in order for the useful analytical information to be extracted. The most critical aspect related to the non-destructive lithium transport evaluation in electron microscopes is the stability of the solid-electrolyte under the intense electron beams. Current densities in modern STEM imaging and EELS have increased significantly due to high focusing capabilities of the modern microscopes, leading to e-beam damage of nano-materials. [56-59] Materials, depending on their physical and thermal properties respond to e-beam dosage in different ways with threshold doses for damage-less imaging. E-beam dose is calculated by multiplying the current density and the exposure time in each pixel and indicated by the number of electrons/nm^2. Threshold doses reported in literature vary from as small as 5 x 10^2 e^- /nm^2 for 100 keV incident energy of the electrons to about 10^7 e^-/nm^2 for 200 keV. [57-60] The contributing factors for the e-beam induced damages are: (i) atomic

displacements, (ii) e-beam sputtering, (iii) e-beam heating, (iv) electro-static charging, and (v) radiolysis. [56] At high incident energies, most of the energy lost by the electrons is due to inelastic scattering which can eventually heat up the sample locally if the thermal conductivity of the sample is low. [56] For electrically-insulating samples at high current densities, lateral migration of ions is possible due to electrostatic charging induced electric fields across the samples. [56] Similarly, radiolysis (e-beam degradation) induced mass loss is also possible. For example, fluorine loss in AlF_3 and metallic Al-nanoparticle formation has been observed due to radiolysis. [56] Lithium phosphorous oxynitride (LIPON) is amorphous, electronically non-conducting and has low thermal conductivity. LIPON is a commercialized solid-electrolyte and has been used in all-solid-state batteries for a long time now [61, 62]. Among the above mentioned aspects of damage, e-beam heating, electro-static charging and radiolysis are all relevant for this work considering the physical, electrical and thermal properties of the solid-electrolyte LIPON. In this chapter, we report the stability of LIPON under both high flux electron and ion beams and present how the beam induced instability can affect the functionality of the nano-batteries and quantitative analysis of EELS data. This type of analysis must be conducted for any solid electrolyte since they are intrinsically susceptible to beam damage.

LIPON is highly sensitive for both e-beam and ion beam damage. Large electron dose leads to decomposition of the electrolyte which is not desirable for the functionality of the battery. The mechanism of LIPON damage can be attributed to three factors (i) electrostatic charging, (ii) beam heating and (iii) radiolysis. Figure 4.5 shows the STEM images recorded after EELS mapping in the region indicated by the

box in each image. Figure 4.5 (a) & (b) show that the LIPON is undamaged while (c) & (d) show that the LIPON is damaged as seen by the dark contrast in most of the pixels. The legends in each figure indicate the electron dose used for EELS mapping which clearly shows that there is a threshold dose of about 0.5 x 10^7 e^-/nm^2, below which no damage can be observed. Both the cathode and anode have very high threshold and do not show any damage at this dose level. These are representative images from many observations and irrespective of pixel size and dwell time. Beyond the threshold dose, damage can be observed.

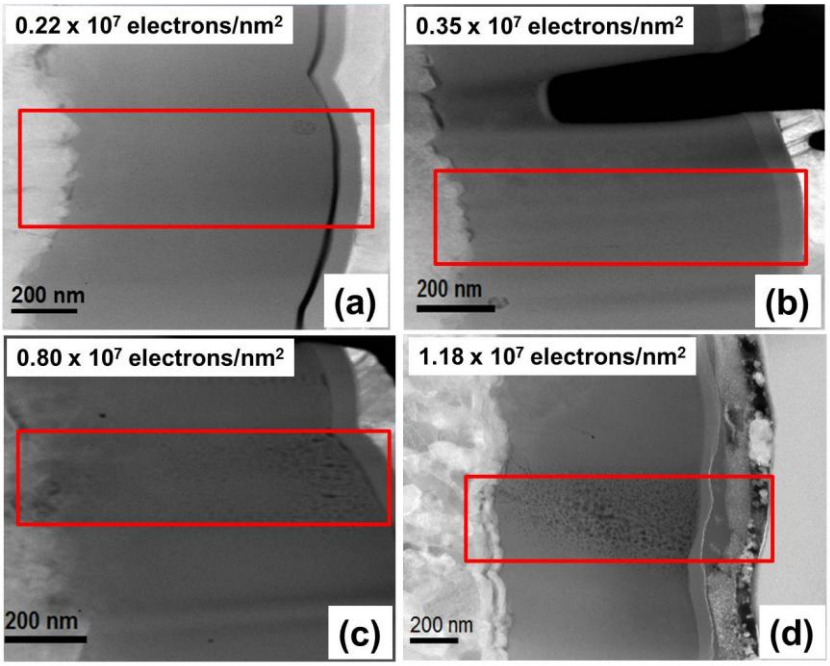

Figure 4.5 Electron dose effect on LiPON during STEM/EELS mapping at various dosage. a) and b) show no observable damage while c) and d) show formation of voids in LiPON [54]

This damage also manifests significant changes in the EELS spectrum edge of elements, more specifically on the Li K-edge. The damaged region shows lower intensity for Li K-edge (as shown in Figure 4.6 and the inset) for the spectra collected

from the same sample but with different electron doses. The lower intensity of lithium K-edge indicates that high electron dose induced damage causes lithium loss. This could be due to localized heating and/or by the electrostatic charging induced electric field which can drive away lithium in LIPON. It is important to note that LIPON has high lithium ion conductivity at high temperatures [63].

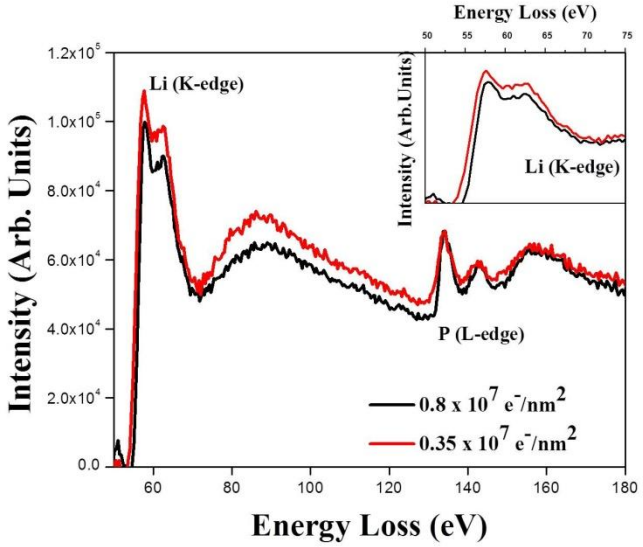

Figure 4.6 Electron dose effect on EELS signal of Li-edge. Larger dose not only damages the LIPON, but also decreases the Li signal intensity.

Figure 4.7 shows a series of bright field TEM images recorded at regular time intervals demonstrating the time evolution of damage in the LIPON electrolyte. Electrolyte damage is in the form of small voids which cluster to form a large void as shown by the low magnification image in Figure 4.7 (f). Similar bubble formation was observed during imaging in a scanning electron microscope operated at 10 kV with equal to or longer than 10 µs dwell time. Such a bubble formation in LIPON is plausibly due to dissociation of N_2 at higher dose; this is typically referred as radiolysis. Radiolysis is predominant in polymers and ionic crystals such as NaCl with

similar dose thresholds [64]. Consequently, imaging with SEM needs to be minimized during FIB fabrication processes to avoid electrolyte damage. Furthermore, LIPON electrolyte is highly sensitive to air/moisture specifically when its cross-sections are thinned down to 100 nm. Swollen electrolyte layer filled with voids was observed if the FIB prepared samples were not transferred to the TEM as soon as possible (preferably less than 15 minutes). This highlights the importance of immediate transfer of nano-batteries from FIB to TEM for *in situ* TEM biasing experiments.

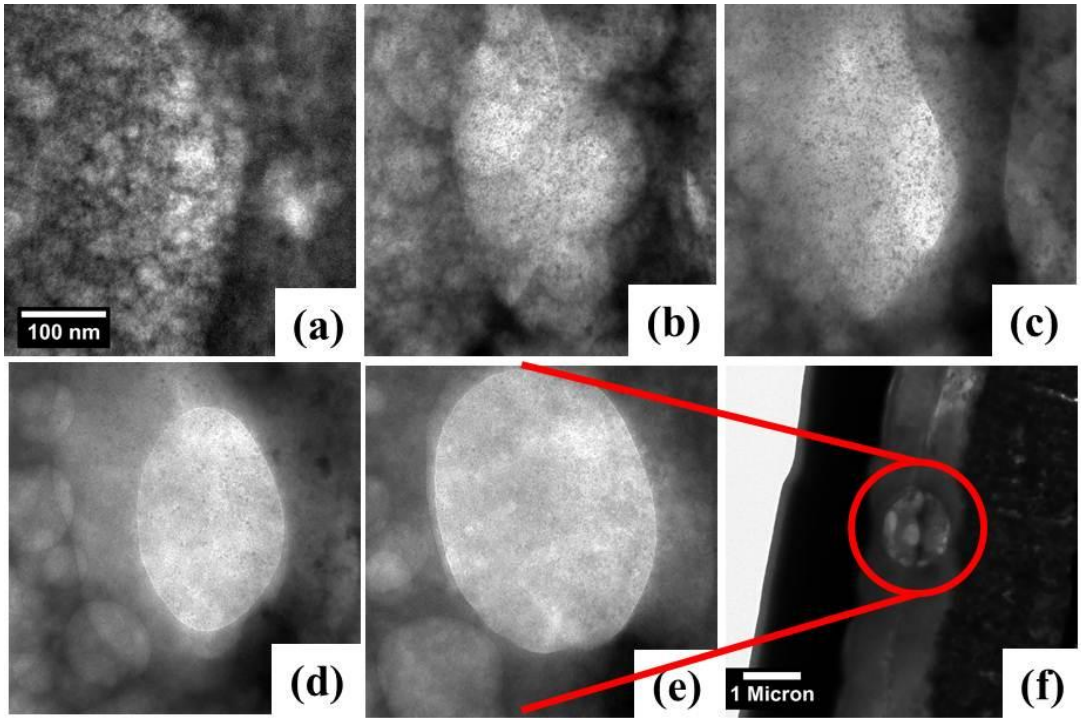

Figure 4.7 The series of images from a) to f) shows the evolution of electrolyte damage as the small voids begin to cluster together to form large voids.

4.4 Design of TEM/STEM Biasing Holders

The strict thinness requirements of TEM samples coupled with the need for electronic biasing of the solid-state batteries demand the creation of new TEM/STEM sample holder designs that fulfill these needs. These designs must accommodate the

individual and separate electrical connections to the cathode and anode of the thin battery sample and the sample holder must have the electrical connections outside of the TEM where it could be connected to a potentiostat. Through exploratory work, a few experimental designs and new TEM holders have emerged and been tested. These designs include TEM holder designs from NanoFactory and ProtoChips, as both manufacturers produce TEM holders capable of electrically biasing the TEM sample.

The main components of successful electrical biasing of the TEM sample include the large TEM holder, sample carrier (where the TEM sample is mounted), and electrical connections from the sample to the sample carrier then finally to the outside end of the TEM holder. Many designs navigate through these obstacles with their own challenges. At the time of this writing, the NanoFactory designs have been used the most for experimentation. Firstly, a design which includes a thinned solid-state battery electrically connected to a sample carrier that serves as connectors to both the cathode and anode (separately of course) is used. The first design is illustrated in Figure 4.8 for clarifications. The semi-circular gold coated pad is a custom made pad from TEMwindows.com with about a 2.85mm diameter and a 200nm surface coating of SiN. The spacing between the two gold pads is 50 micron. The sample carrier is cut horizontally at the square window so that there will be easy access while working with Focused Ion Beam.

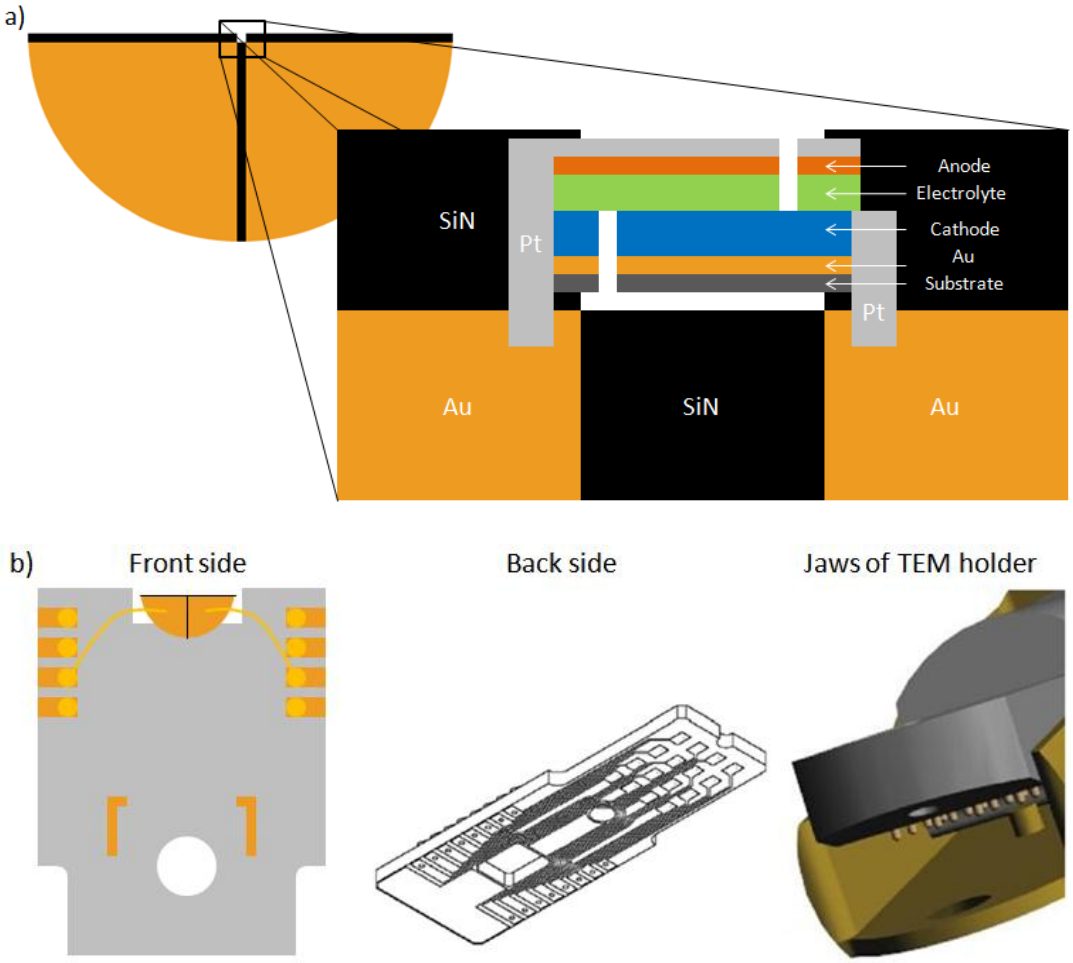

Figure 4.8 First NanoFactory design with connections to both the cathode and anode. a) The thin film battery sample is mounted on a SiN grid with two gold pads which is wired to the connections of the sample carrier. b) The sample carrier is then loaded on to the TEM holder with jaws that make pin hold connections to the sample carrier. Figures courtesy of NanoFactory.

Secondly, a design in which the sample carrier makes one electrode connection and a piezo-controlled tip makes the second electrode connection is also explored. This design is illustrated in Figure 4.9 for clarifications. The technical difficulties with this design lie with the piezo-controlled tip used for connection. When the TEM holder is placed within the TEM, the connection must be made with the tip using manual controls of the piezo-tip. Since the TEM beam will only provide a two-

dimensional planar view of the solid-state battery, the depth information can only be obtained via trial and error. This process takes time and considerable skill to execute properly without physically damaging the solid-state battery. Models made by NanoFactory, such as the Multimodal Optical NanoProbe, are suitable for electric biasing of solid-state thin battery in TEM column. One connection is made via the piezo-controlled tip and the second connection is simply made through the OmniProbe grid, which is conducting and is contacting the O-ring that holds it in place. The TEM holder itself will have leads connecting to the O-ring and piezo-controlled tip separately.

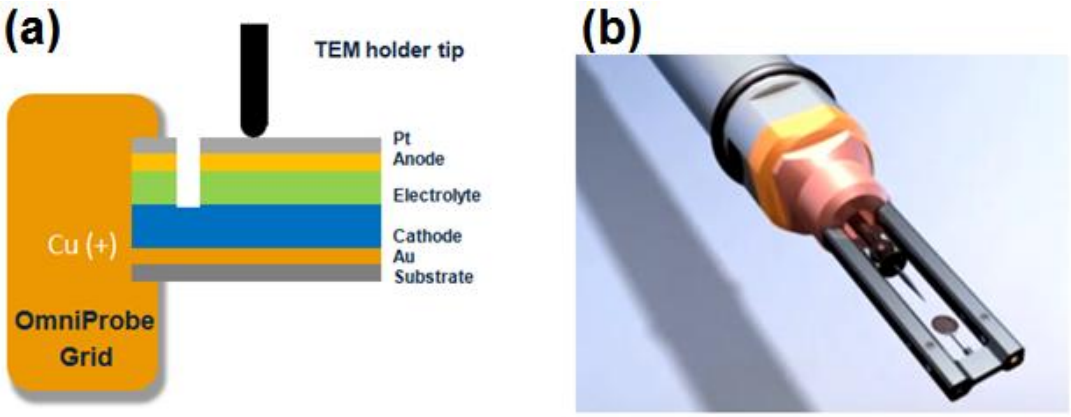

Figure 4.9 (a) shows the electrical connection schematic of the nano-battery, (b) shows an overall view of the second NanoFactory design with connection to one electrode and a piezo-controlled connection to the second electrode. Courtesy of Brookhaven National Lab.

There are some advantages of one design over the other. The first design ensures contact to both electrodes, but the physical dimension of the SiN gap requires the nano-battery to be quite large, which can be difficult to work with using FIB. The second design is not limited by physical dimension restrictions, but the connection

needs to be made in the TEM without a stereo view, which can be tricky due to lack of depth information.

In addition to the NanoFactory design, the ProtoChips Aduro TEM holder is also capable of electrically biasing TEM holders. Such designs have not been experimented with by our group but serve as potential alternatives. However, there are also other potential challenges that these TEM holder designs do not address. For example, the inability to protect the TEM sample from atmospheric conditions during sample carrier mounting on the TEM holder or sample transfer from FIB to TEM can be detrimental to lithium ion battery electrode components that are sensitive to air moisture, especially in the super thinned state. In our opinion, the next generation TEM holders for *in situ* TEM will comprise of designs that eliminate the presence of air exposure conditions. A sample design by us is illustrated in Figure 4.10.

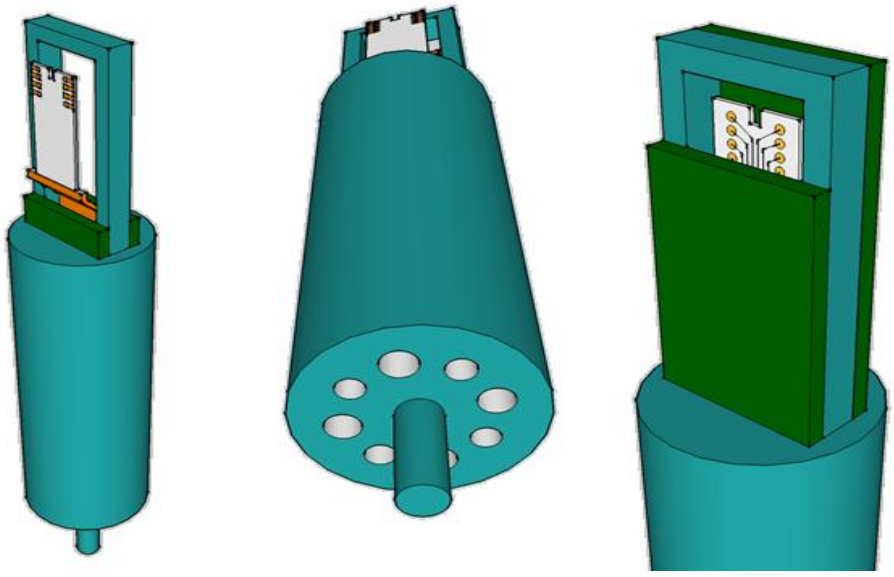

Figure 4.10 Future designs of TEM holder with vacuum sealable capability for *in situ* TEM as envisioned by the authors.

The most important part of this design is a pair of closable doors on both sides of the frame that enclose the TEM sample carrier and keep the contents in vacuum. These doors (drawn with green parts) should be controlled remotely via radio frequency signals or similar technology, allowing opening and closing inside FIB or TEM to permit access. In the open door state, the sample carrier will be out of plane of the frame, allowing FIB interactions such as ion beam milling, Pt welding, and OmniProbe manipulations, which would be blocked by the frame top otherwise. While the doors are closing, the sample carrier will shift back in plane with the frame and allow full closure. Ideally, the sample carrier (white part) should be separable from the connection (orange part) for changing of the sample carriers. The sample carrier can allow multiple connections (eight connections denoted here) while it will be inserted into the orange connector. On the bottom side, there is a central rod that will fit into the slots of any standard modern SEM/FIB machines and other pin holes for the electrical connections. Once the samples are prepared and the vacuum doors closed, this TEM holder head can be connected to the rest of the TEM holder with an inverted part that will make all the necessary connections with the TEM holder head. With the future physical fruition of this design, many new capabilities will be available for *in situ* TEM experiments without the constraints of air exposure.

Chapter 4, in full, is a reprint of the material “Analytical Electron Microscopy – Study of All-Solid-State Batteries” as it appears in Handbook of Solid State Batteries 2nd Edition, Ziying Wang, Ying Shirley Meng, World Scientific, 2015, pp 109-131. The dissertation author was the co-primary investigator and author of this book chapter. All the experiments and writing were performed by the author.

Chapter 5. Ex situ Characterization of Anode-Electrolyte Interface

Understanding the role of interfaces is important for improving the performance of all-solid-state lithium ion batteries. To study these interfaces, we present a novel approach for fabrication of electrochemically active nano-batteries using focused ion beams and their characterization by analytical electron microscopy. Morphological changes by scanning transmission electron microscopy imaging and correlated elemental concentration changes by electron energy loss spectroscopy mapping are presented. We provide first evidence of lithium accumulation at the anode/current collector (Si/Cu) and cathode/electrolyte (Li_xCoO_2/LiPON) interfaces, which can be accounted for the irreversible capacity losses. Inter-diffusion of elements at the Si/LiPON interface was also witnessed with a distinct contrast layer. These results highlight that the interfaces may limit the lithium transport significantly in solid-state batteries. Fabrication of electrochemically active nano-batteries also enables in situ electron microscopy observation of electrochemical phenomena in variety of solid-state battery chemistries.

5.1 Introduction

For almost two decades, lithium ion batteries have been used heavily in consumer electronics worldwide. It is envisioned that they are potential candidates for large scale high power applications including electric vehicles. High power applications require ultrafast lithium transport between the active electrodes through electrolyte in a battery. In spite of ultrafast lithiation of isolated nano-materials [38,

41, 43], similar power densities have not been realized in actual devices. Such discrepancies indicate that active electrode materials alone are not responsible for the poor rate performance. There have been ample indirect evidences that both cathode and anode electrode/electrolyte interfaces can play a major role in lithium ion transport [65, 66]. Nevertheless, most of the *ex situ* as well as *in situ* investigations are concentrated on the performance of either cathode or anode but not the whole system including electrolyte simultaneously [44, 45, 67, 68]. Recently, significant interest has developed to investigate the interfaces in lithium ion battteries both theoretically [69, 70] as well as experimentally [71, 72]. In this respect, an all-solid-state battery is an ideal system to investigate the structural, morphological and chemical changes in the cathode, anode, electrolyte and their interfaces simultaneously. Previous attempts have not yielded promising results; neverthesless, Ruzmetov et al. investigated the scaling limits of the solid-electrolyte and claimed that it is detrimental to electrochemical performance when the electrolyte thickness is reduced down to 100 nm [73]. Yamamoto et al. investigated a solid-state battery with ultra-thick electrolyte (~ 90 μm) using electron holography [42], however only a small portion of the battery near the cathode/electrolyte interface was made electron transparent for their holography investigation. Brazier et al. investigated the diffusion of heavy elements across the cathode/electrolyte interface by *ex situ* transmission electron microscopy (TEM) and energy dispersive x-ray (EDX) analysis [66]. Despite the analysis of heavy elements, the EDX detection limit prevents lighter elements, like lithium, from being quantitatively analyzed. Along with the aforementioned characterization techniques, scanning transmission electron microscopy (STEM) coupled with electron energy loss

spectroscopy (EELS) are advanced techniques to characterize structural, morphological and chemical changes with a unique combination of high spatial, temporal resolution and chemical sensitivity. With state of the art STEM/EELS, one can achieve sub-nanometer resolution, sub-second temporal resolution and the detection of light elements (such as lithium) down to a few atomic percent [74]. It is equally important to minimize electron beam (e-beam) induced damages for proper quantitative measurements, which is currently lacking in the literature. Enabled with this technique, lithium concentration mapping across interfaces in nano-batteries would help with the discovery of new phenomena at the nano-scale which may be otherwise impossible. However, direct application of STEM/EELS on all-solid-state batteries and e-beam damage quantification have not been reported in literature to the best of our knowledge. The foremost obstacle is the difficulty in fabricating electrochemically active thin (~100nm) all-solid-state nano-batteries. In this letter, we elucidate the first instance of focused ion beam (FIB) fabrication of such functional all-solid-state nano-batteries and report for the first time, direct evidence of interfacial related phenomena in lithium ion batteries. Lithium accumulation at the cathode/electrolyte interface was observed during normal charging and an additional phosphorous/silicon inter-diffused layer at the electrolyte/anode interface was observed under an overcharged condition. STEM/EELS chemical mapping highlights that the cathode/electrolyte interface is the chief limiting factor for lithium transport. The current *ex situ* study is a crucial step in achieving *in situ* TEM observations of all-solid-state lithium ion batteries.

5.2 Experimental

Micro-all-solid-state batteries have been deposited by sputtering and the results presented here deal with the Alumina/Pt/$LiCoO_2$/LiPON/a-Si/Cu full cell. More detailed deposition conditions are described in an earlier paper [55]. The nano-batteries (cross-sectional thickness ranging from 100 nm to 2000 nm, while the area was ranging from 100 μm^2 to 20 μm^2) are fabricated using a FIB-SEM dual beam systems (Helios Nano Lab, FEI). The samples for (S)TEM imaging and EELS were prepared by standard FIB lift-out and thinning procedure (< 80 nm thickness). Subsequent to the fabrication of nano-batteries, STEM/EELS studies are performed at 200 keV on a JEOL 2100F machine. EELS spectra were recorded in STEM mode, with an energy resolution of about 1.1 eV, as judged by the FWHM of the zero-loss peak (ZLP). Lithium mapping was generated by fitting the pre-edge background using a polynomial function in the Gatan Digital Micrograph software. To avoid significant overlap with the Co M-edge, only a 5 eV window (from 52.5-57.5 eV) of the Li K-edge was selected for the 2D mapping. Energy window of 102 to 107 eV for Si L-edge and 132 to 137 eV for P L-edge was used to map the integrated intensity of elements.

5.3 Electrochemical bias of FIB fabricated thin film batteries

We start with an electrochemically active micro-battery with Au and Cu as current collectors for the cathode ($LiCoO_2$) and anode (Si) respectively. The fabrication of such thin film batteries have been reported previously [7, 55, 75]. The

optical and cross-sectional SEM images of the micro-batteries used for this study are shown in Figure 5.1. The thickness of the active layers in the current set of batteries were about 2 µm for the cathode, 1.2 µm for the electrolyte and 80 nm for the anode.

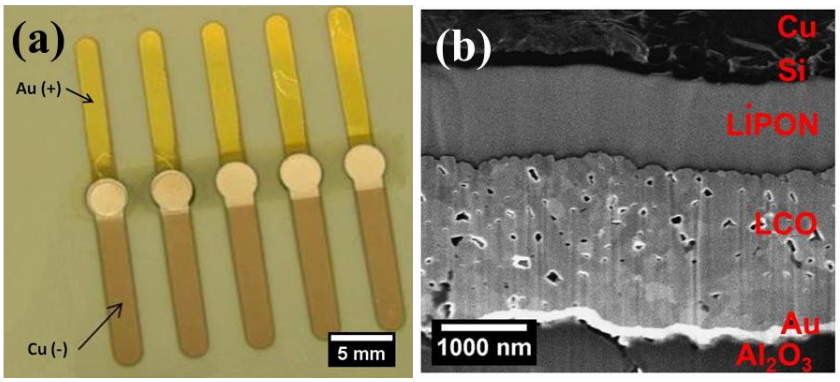

Figure 5.1 Optical (a) Cross-sectional SEM (b) images of the micro-batteries

In order to study the electrochemical activity of the nano-batteries, they were biased in the FIB immediately after fabrication either using the complete isolation or the pseudo-isolation scheme from the thin film battery. Figure 5.2 shows the fully isolated and pseudo-isolated FIB biasing schemes. Left image shows the case where the nano-battery is a liftout from the micro-battery mounted on a grid and biased using the omni-probe as the contact for anode and the grid as contact for the cathode. In this scheme, both the cathode and anode are limited to their maximum theoretical capacity 140 µAh/cm^2 (charged to Li_xCoO_2, x=0.5) and 80 µAh/cm^2 (forming $Li_{15}Si_4$ phase) respectively. Note that in this cell, the cathode has almost double of the anode's capacity. Middle and right images show the case where only the anode is isolated form the thin-film battery by FIB milling down to the electrolyte. In such a case, the cathode in principle has unlimited capacity compared to the anode. This enables the

cathode to transport lithium several times higher than the capacity of the anode. This is how the overcharged sample reported in the manuscript has been prepared.

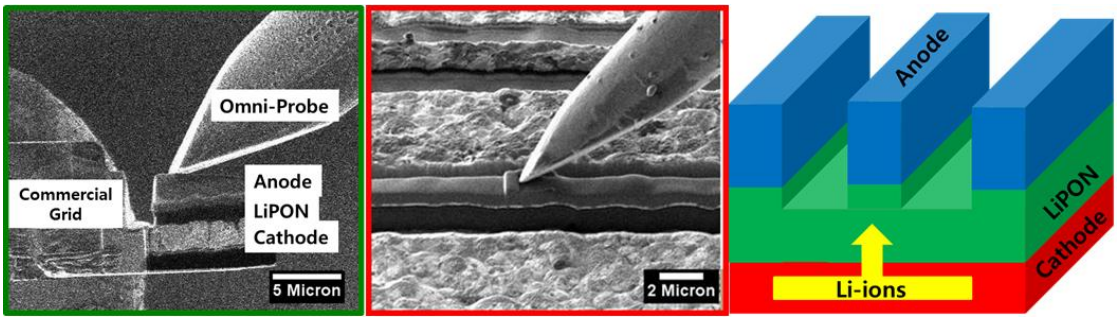

Figure 5.2 Isolated and Pseudo-isolated nanobatery biasing schemes

The nano-batteries were charged galvanostatically (typically with a current density of about 100 μA/cm^2, equivalent to 1.25C rate) *in situ* in a FIB using the omniprobe as shown in Figure 5.3.

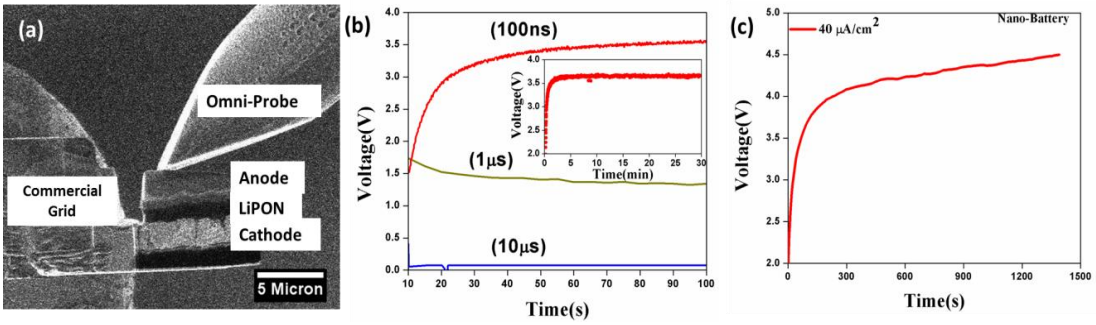

Figure 5.3 (a) SEM image of a typical FIB biasing of a nano-batetery using omni-probe. Electrochemical voltage profile of FIB fabricated all-solid-state (b) nano-battery at different fabrication pixel dwell times but fixed biasing current density of 100 μA/cm^2 and (c) nano-battery at two different biasing current densities and inset in (b) shows the top view SEM image of the nano-battery.

Firstly, the successful fabrication of electrochemically active nano-batteries requires very specific optimization of the FIB process, and pixel dwell time was found to be the most important factor. The charging profile for a nano-battery fabricated using a 10 μs pixel dwell time displays hardly any voltage as shown in Figure 5.1 (b), indicating shorting across the stack, while the charging curve for a nano-battery fabricated using 1 μs pixel dwell time shows a voltage lower than the expected 3.6 V. However when the nano-battery was fabricated using a 100 ns pixel dwell time, the charge profile shows the voltage reaches 3.6 V. In addition, the inset in Figure 5.1 (b) shows that the charging profile, when extended to 30 mins (equal to 50 $\mu Ah/cm^2$), plateaus at 3.6V throughout the entire charging period. Nano-batteries fabricated under these conditions are highly consistent and repeatable with a 3.6 V voltage plateau which agrees well with the voltage profile of micro-batteries [55]. The electrochemical activity preserved in the nano-batteries while using smaller pixel dwell time is possibly due to minimization of localized heating and compositional changes of the LiPON electrolyte. Following the successful nano-battery fabrication, we scaled down the cross-section thickness to 200 nm and Figure 5.1 (c) displays the charging profile for 40 $\mu A/cm^2$ current density. The typical current density (100 $\mu A/cm^2$), used for thicker nano-batteries, was too high leading to a large polarization causing the voltage limit to be attained much faster in these thinner nano-batteries. Meanwhile, a 40 $\mu A/cm^2$ current density yields a profile with a plateau higher than the expected 3.6 V indicating the current density is still too high. As we have reached the lowest limit of our current source at 40 $\mu A/cm^2$ (using 1 pA as the absolute biasing current), we are in the process of developing a fA current source for future

experiments. Cycling performance of the nano-batteries in the FIB were also investigated and the first 10 cycles (Figure 5.4) were similar to the micro-batteries previously reported [55] which shows a considerable amount of capacity loss.

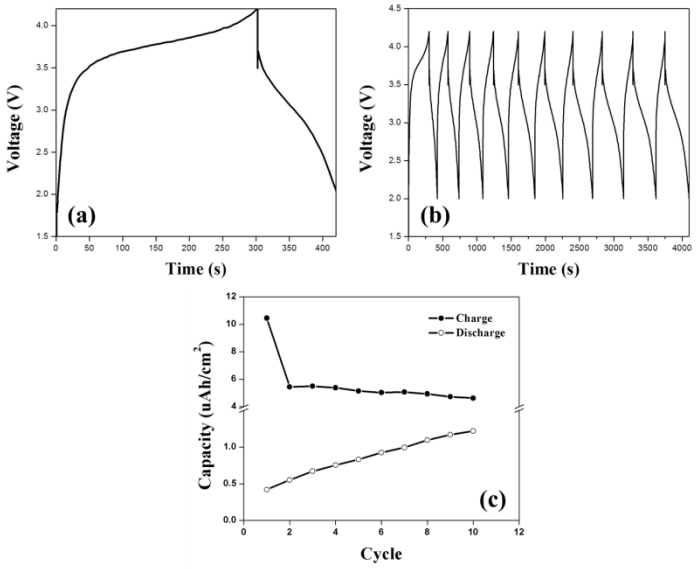

Figure 5.4 (a) First cycle data and (b) 10 cycle data of the isolated micro-batteries (c) Charge and discharge capacities for the 10 cycles.

5.4 *Ex situ* STEM/EELS Characterization of Anode-Electrolyte Interface

With the developed optimized FIB process, electrochemcially active nano-batteries were fabricated and then charged to different states using the pseudo-isolated scheme. They were further thinned by FIB and investigated by *ex situ* STEM and EELS to understand the structural, morphological and chemical changes. Results for three different samples presented here are (i) *pristine*, (ii) *charged:* to 80 μAh/cm^2 at a rate of 1.25C (iii) *overcharged:* to about 260 μAh/cm^2 at a rate of 100 times the

charged sample (more details in section 2 of the supplementary data). There are signficant morphological and chemical changes, although no detectable structural changes were found from the electron diffraction analysis within all active layers (Figure 5.5). The diffraction pattern indicates that the Si anode and LiPON electrolyte are amorphous while the LCO cathode is polycrystalline in nature as identified from the ring indices. For the charged and overcharged samples, there was hardly any change in the structure as the anode and electrolyte remain amorphous while the cathode was still crystalline (as identified from the ring indices). In the present case, the diffused rings in the anode diffraction pattern indicate that the silicon did not form the crystalline phase. The pristine LiPON electrolyte is amorphous and no structural change was observed as expected during cycling the nano-battery.

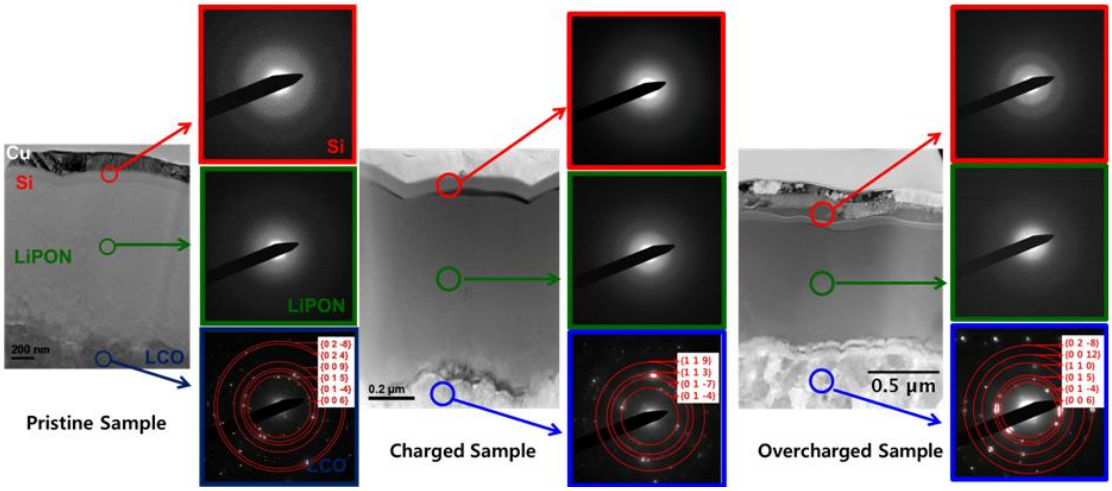

Figure 5.5 Pristine, Charged and Overcharged sample diffraction pattern of cathode, electrolyte and anode regions.

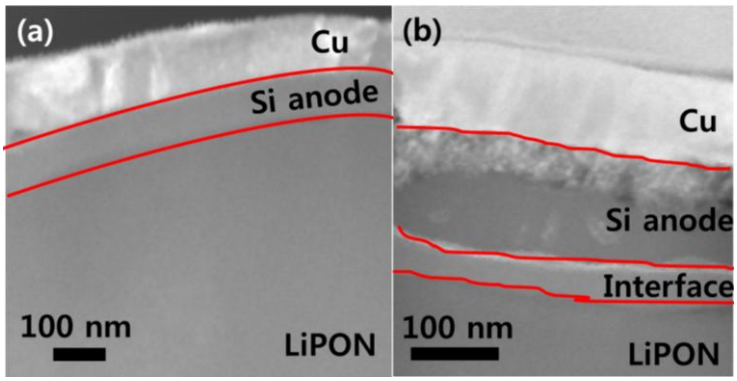

Figure 5.6 Cross-sectional annual dark-field STEM image of the anode region for (a) pristine (b) overcharged samples.

As shown in Figure 5.6, there is remarkable difference of the anode regions in the pristine and overcharged samples, with a sharp interface between anode and electrolyte in the former versus broad/thick interface in the latter. The anode thickness increased significantly from 85 nm in the pristine to about 140 nm in the overcharged sample corresponding to an expansion of about 165%, which may be due to first stage of lithiation of amorphous silicon anodes according to the literature [76, 77] and detailed discussions are given in the supporting information. In other cases, the different contrast in the silicon copper interface is normally attributed to inter-diffused interface upon cycling as observed by STEM/EDX analysis[78]. Howevver, we present additional diffrences based on lithium concentration analysis described later in this manuscript. To correlate morphological changes with the chemical changes, EELS 2D mapping was performed on all three samples. Figure 5.7 (a, b & c) shows the data for pristine, charged and overcharged samples respectively. The 2D mapping of Li, P and Si (shown in red, green and blue colors respectively) is shown in the left image, corresponding STEM image in the middle and the lithium concentration

mapping on the right (increasing lithium concentration from green to red). For the pristine sample, the bright red and blue regions in the cathode and anode respectively clearly demonstrate the pristine state of LCO and Si. The interface sharpness (as discussed above) is also clearly evidenced in these concentration maps. However, vital information can be obtained from the lithium distribution across the stack. The variation of lithium concentration by four color gradients with increasing concentration from blue to red. For the pristine sample, lithium is concentrated in the cathode and the electrolyte while absent in the anode.

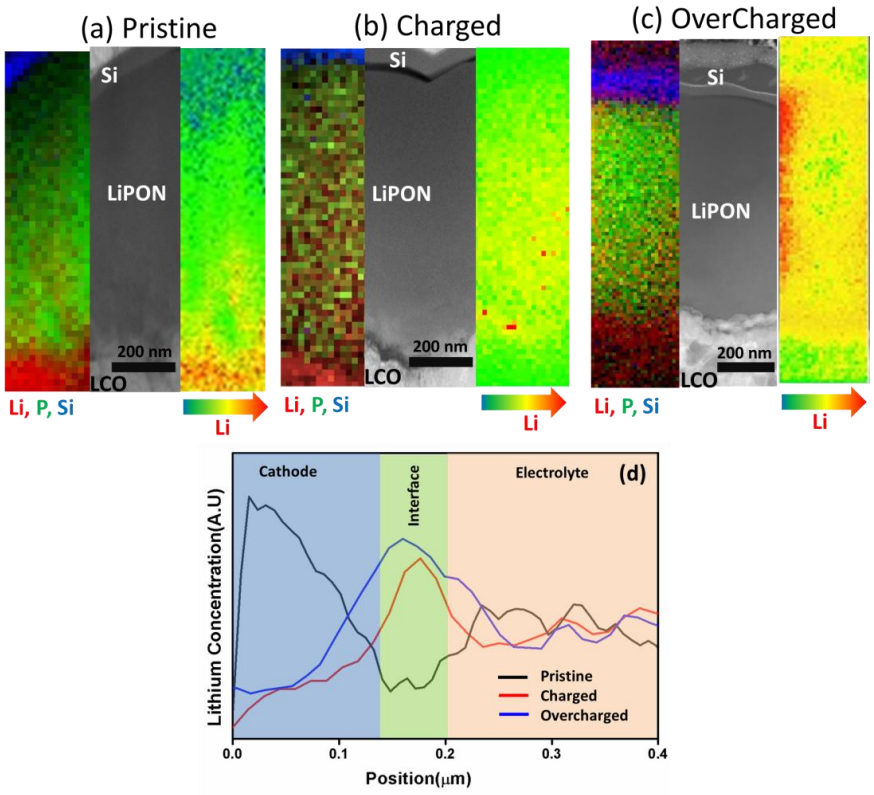

Figure 5.7 Elemental distribution mapped by EELS for pristine (a), charged (b) and overcharged (c) samples and lithium concentration profile (d), indicating lithium accumulation at the cathode/electrolyte interface.

In the charged and overcharged samples, the lithium has been transported to the anode, which can be seen from the green color in both cathode and anode, indicating similar concentrations of lithium in both electrodes. Interestingly, some pixels near the cathode/electrolyte interface reveals a high concentration of lithium, indicating accumulation at this interface. More detailed line scan analysis of the lithium concentration at this interface is presented in Figure 5.7 (c). It is clearly seen that the lithium concetration is high in the cathode of pristine sample while the charged and overcharged samples are lithium depleted. Decrease of lithium concentration near the cathode/electrolyte interface of the pristine sample was observed in several data sets and it is possibly due to preparation process. In contrast, an increased concentration is seen at the cathode/electrolyte interface for the charged and overcharged samples. This provides strong evidence that lithium accumulation occurs at this interface, which may play a significant role in the overall performance of the battery. The possible reason for lithium accumulation is unclear at the moment and requires more study which has been planned to be done in the near future. The stability of active layers under e-beam during STEM/EELS are important for lithium quantification which was performed as part of this work and reported in section 6 of the supporting information. Apart from lithium accummulation at the cathode/electrolyte interface, an additional anode/electrolyte interface of lithium accumulation was evident for the overcharged sample. A more detailed spectral investigation was carried out at the anode/electrolyte interface of the overcharged sample. Figure 5.8 displays the low loss EELS spectra across the anode/electrolyte interface indicated by numbers “0 to 7”.

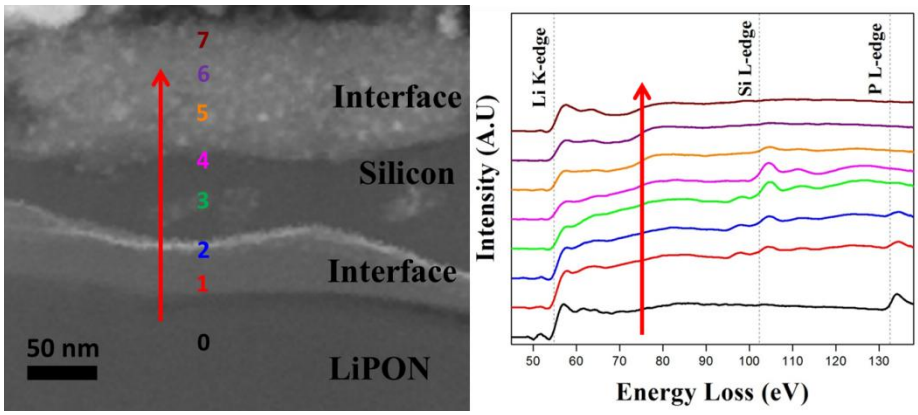

Figure 5.8 Annual dark-field STEM image of the anode/electrolyte interface in the overcharged sample (a) and the EELS spectra (b), recorded from 8 different sites, as labelled in the image.

It is clearly seen that position 0 is from the LiPON electrolyte where Li K-edge and P L-edge peaks can be observed while the Si L-edge is not present. The spectra from position 1 & 2 are from the interface region where all three, Li K-edge, Si L-edge and P L-edge peaks are present. This interdiffused interface region is clearly distinct compared to the pristine sample (which exhibits a sharp interface). In the spectra from position 3, 4 & 5 we can see that the Li K-edge and Si L-edge peaks are present while no P L-edge is visible indicating a lithiated silicon anode. However, spectra from position 6 and 7 show an intense Li K-edge peak while no significant Si L-edge peak. Possibly lithium plating occurs at the Si/Cu interface, as indicated by high lithium concentration. Lithium accumulation at the silicon/metal interface has been observed recently by other groups well [71]. Additionally lithium plating at the LiPON/Cu interface in solid-state batteries while cycling at moderate current densities have been reported previously [79]. They observed more than 45% irreversibility was

observed at the first cycle due to lithium plating while after 100 cycles only 20% of the initial charge capacity was reversible [79]. From our set of spectral analysis, we note the formation of a phosphorus-silicon inter-diffused layer in the silicon/LiPON interface upon prolonged lithiation. This interface layer shows both microscopic contrast and chemical changes. The lithium loss at the end of first cycle and subsequent cycles in solid-state batteries can be attributed to interfacial changes and lithium plating observed in the present study. Significant amount of stress due to volume expansion is possibly accommodated by the inter-diffused interfaces on both sides of the anode and interface limited reaction rate [80]. These observations highlight that interfaces are the key limiting factor in solid-state lithium ion batteries.

5.5 Conclusion

To summarize, we have successfully fabricated electrochemically active all-solid-state nano-batteries for the first time and investigated the interfacial chemical changes by *semi-quantitative* STEM/EELS analysis. Lithium mapping in electrochemically active nano-batteries shine light on interface-limited Li transportation across the stack. The lithium accumulation at the cathode/electrolyte interface is significant, while an additional phosphorous-silicon inter-diffused anode/electrolyte interface with lithium plating at the Si/Cu interface in the overcharged sample is evidenced by both microscopic and chemical changes. More importantly, we demonstrated that crucial information on interface related issues is obtainable only through the all-solid-state battery approach. The results presented here reveal the importance of interface engineering of all-solid-state lithium ion batteries in

order to improve the reversibility of lithium insertion and improve cycling and rate performances. This study also shows the viability of *in situ* TEM cycling of all-solid-state nano-batteries and lays the ground for exploration of new solid state chemistries at nano-scale.

Chapter 5, in full, is a reprint of the material "Interface Limited Lithium Transport in Solid-State Batteries" as it appears in the Journal of Physical Chemistry Letters, Dhamodaran Santhanagopalan, Danna Qian, Thomas McGilvray, Ziying Wang, Feng Wang, Fernando Camino, Jason Graetz, Nancy Dudney, and Ying Shirley Meng, 2014, 5, 298-303. The dissertation author was a co-primary investigator and author of this paper. The author wrote the STEM-EELS analysis of anode-electrolyte interface part.

Chapter 6. In situ Characterization of Cathode-Electrolyte Interface

Behaviors of functional interfaces are crucial factors in the performance and safety of energy storage and conversion devices. Indeed, solid electrode-solid electrolyte interfacial impedance is now considered the main limiting factor in all-solid-state batteries rather than low ionic conductivity of the solid electrolyte. Here, we present a new approach to conducting *in situ* scanning transmission electron microscopy (STEM) coupled with electron energy loss spectroscopy (EELS) in order to uncover the unique interfacial phenomena related to lithium ion transport and its corresponding charge transfer. Our approach allowed quantitative spectroscopic characterization of a galvanostatically biased electrochemical system under *in situ* conditions. Using a $LiCoO_2$/LiPON/Si thin film battery, an unexpected structurally disordered interfacial layer between $LiCoO_2$ cathode and LiPON electrolyte was discovered to be inherent to this interface without cycling. During *in situ* charging, spectroscopic characterization revealed that this interfacial layer evolved to form highly oxidized Co ions species along with lithium oxide and lithium peroxide species. These findings suggest that the mechanism of interfacial impedance at the $LiCoO_2$/LiPON interface is caused by chemical changes rather than space charge effects. Insights gained from this technique will shed light on important challenges of interfaces in all-solid-state energy storage and conversion systems and facilitate improved engineering of devices operated far from equilibrium.

6.1 Introduction

All-solid-state lithium ion batteries have the potential to become the next generation of energy storage devices through the promise of higher energy density and better safety.[81] The use of solid state electrolyte enables the use of lightweight metallic lithium as the anode while substituting the commonly used flammable organic electrolyte. While the ionic conductivity of certain solid state electrolytes has converged on and in some cases surpassed organic liquid electrolytes,[82-85] their wide spread application has been limited by the large interfacial resistance between the solid electrolyte and electrode.[81, 86-88] In the case of amorphous lithium phosphorus oxynitride (LiPON) as the solid electrolyte, many studies have focused on methods to reduce the interfacial resistance through post deposition heat treatment and off-axis deposition.[89, 90] However the physical mechanism for the high lithium ion transfer impedance is still unclear. Space charge effects were thought to be the cause of interfacial resistance between high voltage spinel and LiPON,[91] while computational studies have indicated thermodynamic instability at various solid electrolyte - electrode interfaces.[92, 93] To truly understand the chemical reactions and phase transformations that occur at the electrode-electrolyte interface, dynamic analytical characterization of interfacial behavior far from equilibrium, i.e. without relaxation and air exposure, is required and would be invaluable in designing advanced functional systems with low interfacial impedance.

Indeed, *ex situ* analytical characterization of solid-solid interface was first explored by Brazier et al. where a focused ion beam processed cross section of a

cycled thin film battery was characterized in the TEM.[94] Such preparation of a nanobattery offered an unprecedented high resolution characterization of the solid electrolyte – electrode interface. However, the lack of electrochemical activity in the nanobatteries fabricated through their approach meant that dynamic changes could not be characterized under *in situ* conditions. Since then, *in situ* transmission electron microscopy has made great strides via other approaches involving the use of ionic liquids and liquid cells to observe morphological changes in lithium ion battery materials. Despite the advances, these approaches have not succeeded in the simultaneous application of three important experimental conditions: quantitative chemical characterization, galvanostatic current control, and *in situ* environment. *In situ* TEM studies exploring lithiation of anode nanowires lack electrochemical current control which prohibits quantitative interpretation of the observed structural, morphological, and chemical changes with respect to redox potentials, and more importantly, state of charge.[38-40, 43-45, 95, 96] Quantitative analytical characterization is inherently difficult in liquid cells as spatial resolution is diminished by the presence of a silicon nitride membrane and core-loss signal in electron energy loss spectroscopy (EELS) is overwhelmed by multiple scattering from the liquid electrolyte.[97-99] Using electron holography, Yamamoto et al. observed the electric potential distribution at the $LiCoO_2$ - Ohara solid electrolyte interface under *in situ* conditions.[42] However, the electrochemical cell was biased using cyclic voltammetry which did not offer state of charge control and substantial quantitative analysis of interfacial phenomena was not provided. Therefore, a new methodology is

needed to provide *in situ* structural and quantitative chemical probing of interfacial phenomena in all-solid-state batteries.

Here, we demonstrate a new approach to *in situ* scanning transmission electron microscopy (STEM) coupled with electron energy loss spectroscopy (EELS) characterization of interfacial phenomena using solid state batteries with simultaneous galvanostatic biasing. Our novel approach utilizes a carefully designed and controlled focused ion beam (FIB) fabrication procedure which enables electrochemically active nanobatteries to be galvanostatically biased in the FIB or TEM column.[100] With *in situ* biasing, we can avoid reactions due to air exposure and allow characterization of electrochemical systems without relaxation. Additionally, quantitative characterization of all-solid-state electrochemical systems is not hindered by the cell membranes or liquid electrolytes present in liquid cells. We have previously shown lithium plating at the anode/current collector interface along with inter-diffusion of elements at the anode/electrolyte interface by using *ex situ* STEM-EELS analysis.[100] In this study, we report successful *in situ* STEM-EELS characterization of the cathode/electrolyte interface by galvanostatically biasing a solid state nanobattery. We discovered a disordered interface layer derived from layered $LiCoO_2$ inherent to the $LiCoO_2$/LiPON interface, suggesting that chemical instability leading to the formation of an ionic resistive layer is the main mechanism of interfacial impedance.

6.2 Experimental

We deposited solid-state batteries consisting of 2 µm $LiCoO_2$ (cathode theoretical capacity of 140 µAh/cm^2 up to $Li_{0.5}CoO_2$), 80 nm amorphous Si (anode

theoretical capacity of 66.7 μAh/cm^2 assuming $Li_{3.75}Si$), and 1.5 μm lithium phosphorus oxynitride LiPON electrolyte with Au and Cu as cathode and anode current collectors. The cathode and electrolyte were deposited by RF-magnetron sputtering, while Au, Cu, and Si were deposited by DC sputtering. Cross sectional ion-beam image of the solid-state battery is shown in Figure 6.1A. In order to measure the bulk performance of the as deposited solid-state batteries, we cycled a cell at C/10 for five cycles and C/2 for an additional twenty cycles while limiting full cell capacity to 3000mAh/g relative to the silicon anode. A bonding layer of 10 nm Co was used to increase the adhesion of the batteries with the substrates. A 100 nm-thick Au film was deposited by DC sputtering on high-purity alumina (99.6%) as the cathode current collector. The cathode, 2 μm $LiCoO_2$, was fabricated by RF magnetron sputtering of a home-made $LiCoO_2$ target in ultra-pure Ar atmosphere (99.999%). After deposition of the cathode layer at room temperature, the films were annealed at 750 °C in pure oxygen for 2 hours to crystallize $LiCoO_2$. LiPON solid electrolyte was fabricated using RF sputtering of a home-made Li_3PO_4 target in pure N_2 (99.999%). The anode was 80 nm N-type doped Si, and the anode current collectors were 80 nm Cu. The full cell cycled thin film batteries had an additional 200 nm LiPON layer that was used to protect the batteries and avoid any possible side reaction with the atmosphere. There is an initial irreversible capacity loss on the first cycle with coulombic efficiency of 75% as shown in Figure 6.1B, while subsequent cycles had coulombic efficiencies of nearly 100%. Since the cathode has almost twice the capacity of the anode, the cathode is able to provide more charge/discharge capacity on the second cycle. Once we have established proper bulk electrochemistry of the all-solid-state thin film battery, we

used other samples fabricated using the same procedure for *in situ* TEM experiments. The first cycle irreversibility in contrast with subsequent high coulombic efficiencies is the focus of STEM-EELS studies conducted.

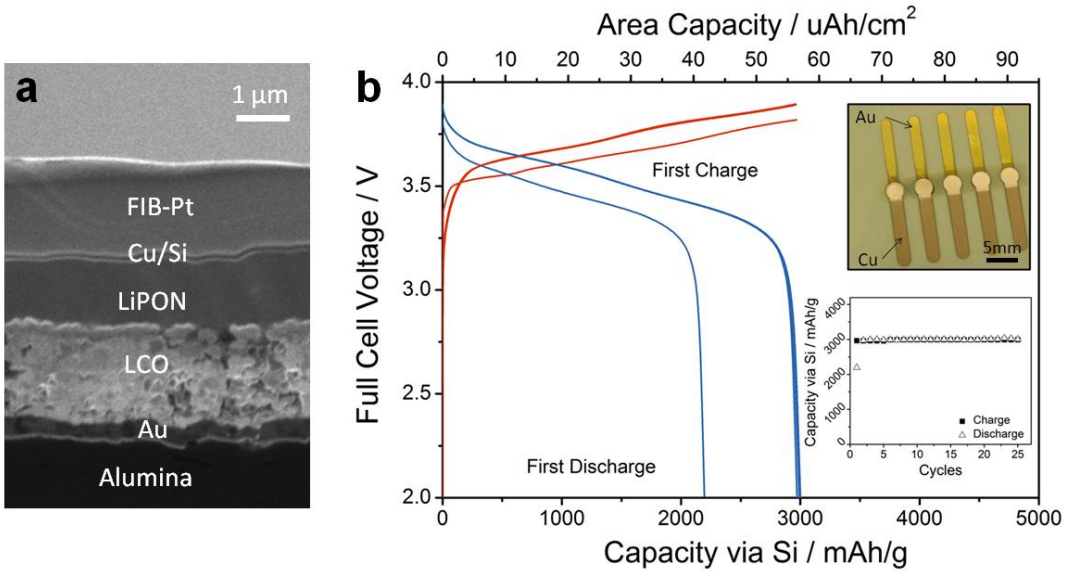

Figure 6.1 RF-magnetron sputtered all-solid-state batteries. a, Cross sectional ion-beam image of the solid-state battery shows all the solid-state components. b, The cycling profile of the solid-state batteries where the red lines denote charge profiles and the blue lines denote discharge profiles. The insets show the optical image of the solid-state batteries and the capacity vs. cycle over 25 cycles.

In order to perform *in situ* experiments, we devised a set of FIB fabrication conditions that will retain electrochemical activity in a nanobattery that can be charged galvanostatically in the FIB chamber or transferred to a TEM column for *in situ* galvanostatic biasing. A set of optimized beam current and pixel dwell time conditions was required to minimize ion damage and preserve electrochemical activity. The process of ion beam optimization and effects of pixel dwell time are detailed in our previous publications.[100, 101] For typical FIB liftout and fabrication techniques,

beam energy and current are given more importance compared to pixel dwell time. Our procedures emphasize that pixel dwell time is the most important factor along with proper beam current control for timely FIB fabrication. After a high current (< 3.0 nA, 30 kV) regular cross section milling, a low current (<0.3 nA, 30 kV) cleaning cross section was used to clean off the re-deposition. All processes were conducted with 100 ns pixel dwell time to avoid heating damage to the electrolyte and re-deposition that could cause loss of electrochemical activity. The pristine sample was prepared using the optimized procedures and thinned to ~ 80 nm in the FIB without electrochemical biasing. The *ex situ* sample was made from a 2 µm by 10 µm rectangular nanobattery charged to 4.2 V in the FIB chamber and subsequently thinned down to ~ 80 nm for TEM. The *in situ* sample was made from a 1 µm by 10 µm triangular nanobattery which was transferred to the TEM and charged to 4.2 V with the e-beam off to avoid accumulation of beam damage on LiPON. Schematic of the experimental setup is shown in Figure 6.2A. The tip of the triangular geometry is thin enough (~ 80 nm) for EELS characterization (Figure 6.2B) and the electrochemical profile is shown in Figure 6.2C.

As the LiPON electrolyte is highly sensitive to electron beam dosage, we have determined the optimal electron dosage to avoid significant beam damage for low loss EELS data collection in our previous publications.[100, 101] STEM/EELS images and spectrums were collected on a JEOL 2100F located at the Center for Functional Nanomaterials at Brookhaven National Laboratory. The beam energy is 200 kV. For all spectrums, the second smallest aperture was used where the beam density measured

by the fluorescent screen was 2.4 pA/cm^2. The beam diameter was focused to approximately 0.2 nm. The energy resolution of the electron energy loss spectra is approximately 1 eV. For low loss mapping and spectrums, a 0.1 s pixel dwell time and 0.2 eV/channel dispersion were used. The pristine sample and *ex situ* sample had 20 nm pixel size for the mapping and later binned to 60 nm pixel size, while the *in situ* sample had pixel size of 60 nm. For high loss spectrums, a 20 s pixel dwell time, 40 nm pixel size, and 0.2 eV/channel dispersion were used. Selected area electron diffraction (SAED) was collected with the smallest objective aperture (~150 nm in diameter) to avoid diffraction from multiple layers. STEM-EELS analysis comparing the morphology, structure, lithium concentration profile, and chemical bonding of different layers in these three samples will be presented and discussed.

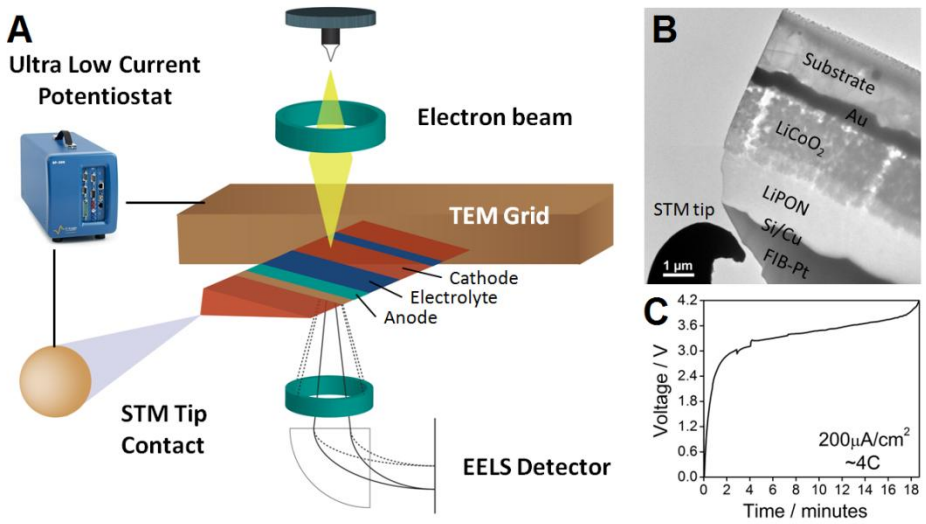

Figure 6.2 Schematic of *in situ* TEM biasing of nanobattery. a, Schematic of the experimental setup of nanobattery mounted on a TEM grid shows the triangular geometry of the cell. The cathode is electrically connected to the grid and a piezo-controlled STM tip makes contact with the anode current collector. b, TEM bright field image of STM tip connecting a nanobattery. c, Electrochemical profile of the *in situ* cell galvanostatically charged in the TEM.

6.3 Structural Characterization of Cathode-Electrolyte Interface

High angle annular dark field (HAADF) images of the pristine sample displayed distinct layers of the expected solid-state components (Figure 6.3A). We also conducted elemental mapping by low loss EELS to show the expected distribution of Li, P, and Si in their respective components. Selected area electron diffraction showed amorphous silicon with the copper current collector (Figure 6.3B) and amorphous LiPON electrolyte (Figure 6.3C) as expected. We observed however, an unexpected and previously unreported interfacial layer, 250-300 nm thick, between $LiCoO_2$ (cathode) and LiPON (electrolyte) in all samples. This disordered interface layer is derived from LCO and hence it will be referred to as the disordered LCO layer while rest of the LCO layer will be referred to as the ordered LCO layer. The disordered LCO layer showed diffuse rings in selected area electron diffraction that do not index to layered lithium cobalt oxide structure with R-3m symmetry (Figure 6.3D), while the ordered LCO layer showed distinct spots for a polycrystalline layered LCO (Figure 6.3E).

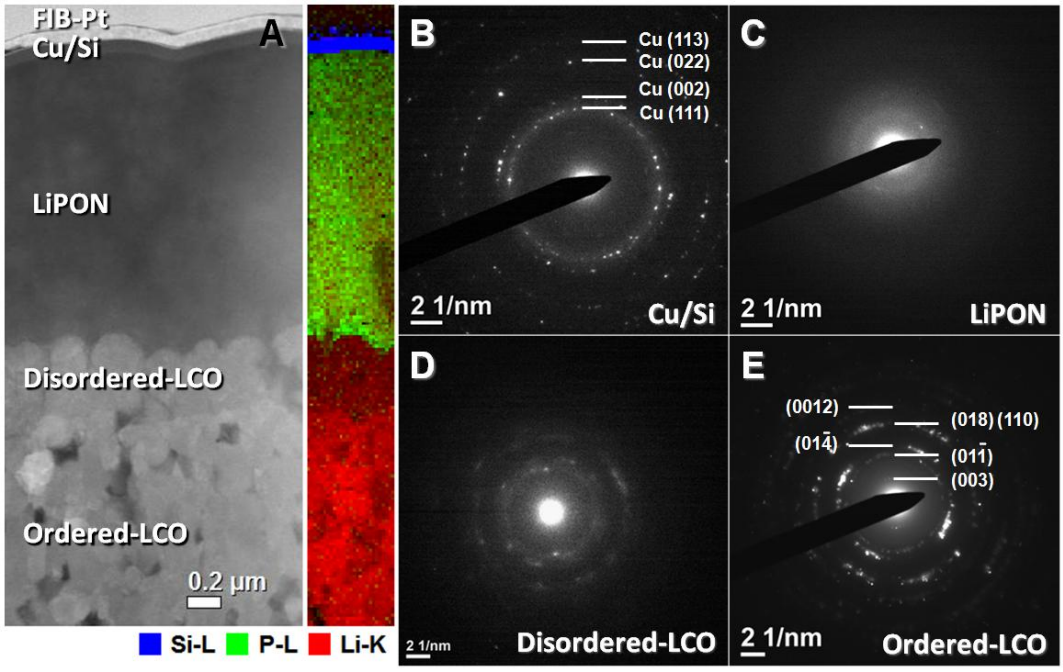

Figure 6.3 Scanning transmission electron microscope imaging of solid-state battery. a, High Angle Annular Dark Field (HAADF) image of the nanobattery stack along with elemental mapping of Li (red), P (green), and Si (blue). b-e, SAED obtained from (b) Cu/Si, (c) LiPON, (d) disordered LCO layer, and (e) ordered LCO layer.

From the integrated radial intensity of the electron diffraction pattern (Figure 6.4), we can reasonably speculate that the interfacial layer is composed of a highly disordered solid-solution of Li_2O and CoO in rocksalt structure decomposed from layered LCO. The broadness of the rocksalt peaks indicates that there is variation in the lattice parameter of the disordered phase. This could be caused by non-uniform local lithium to transition metal ratio leading to local lithium excess and local lithium deficiency domains. Despite the disordered nature of the interfacial layer, lithium conduction is still possible in percolating channels that could arise in regions with lithium excess stoichiometry as proposed by Lee et al.[102]

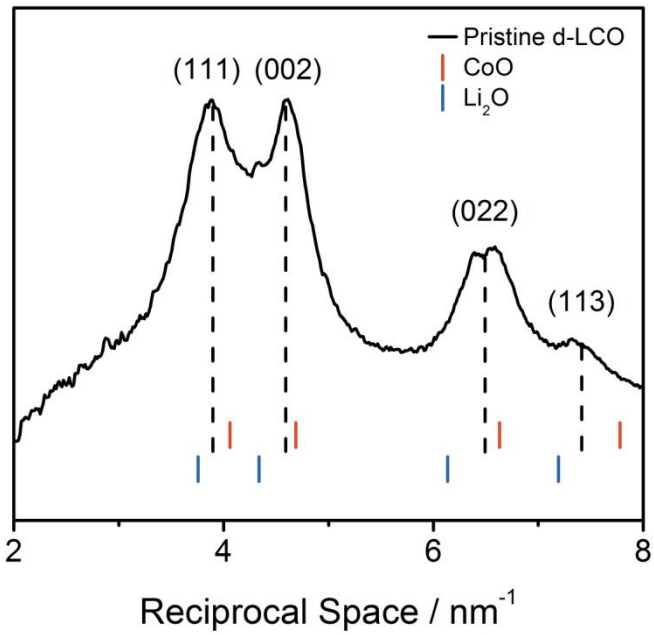

Figure 6.4 Integrated radial intensity pattern of electron diffraction of the pristine disordered LCO layer. Multiple diffraction patterns of the pristine disordered LCO layer were averaged together. The peak positions indicate that the phase is rocksalt-like and could be a solid solution of Li_2O and CoO.

6.4 STEM-EELS Characterization

Having discovered a distinct interfacial layer between the cathode and electrolyte layers, we conducted low loss EELS mapping of the interfacial region to explore the ionic transport of lithium. Given the convoluted nature of Li-K edge with Co-M edge and the shifting of Li-K edge based on chemical environment, an integration window of 5 eV spanning from 55 eV to 60 eV was chosen. It is important to note that intensity contributions in this integration window can only arise from metallic lithium or lithium containing compounds such as lithium carbonate, lithium oxide[103] or LiPON with small potential contributions from CoO rocksalt. This is because $LiCoO_2$ standards resulted in slight negative intensity due to Fano

Resonance[104] and Co_3O_4 standards showed minimal intensity in the energy range (Figure 6.5).

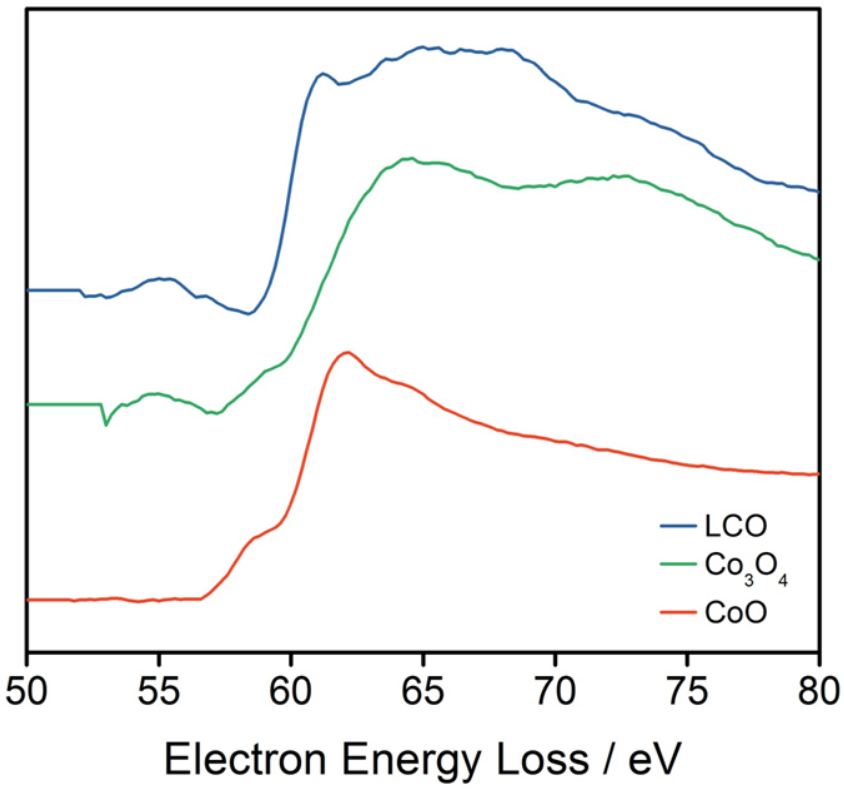

Figure 6.5 Low loss spectra taken from CoO, Co_3O_4, and $LiCoO_2$ standards

Compared to the pristine sample (Figure 6.6A), the *ex situ* (Figure 6.6B) sample has significant integrated intensity in the disordered LCO layer contouring to the physical morphology of the LiPON/disordered LCO interface. This confirms our previous study where *ex situ* lithium accumulation was observed at the LCO/LiPON interface.[100] Integrated intensity mapping of the *in situ* sample (Fig. 6.6C) also

showed increased counts in the disordered layer indicating lithium accumulation occurs during charging.

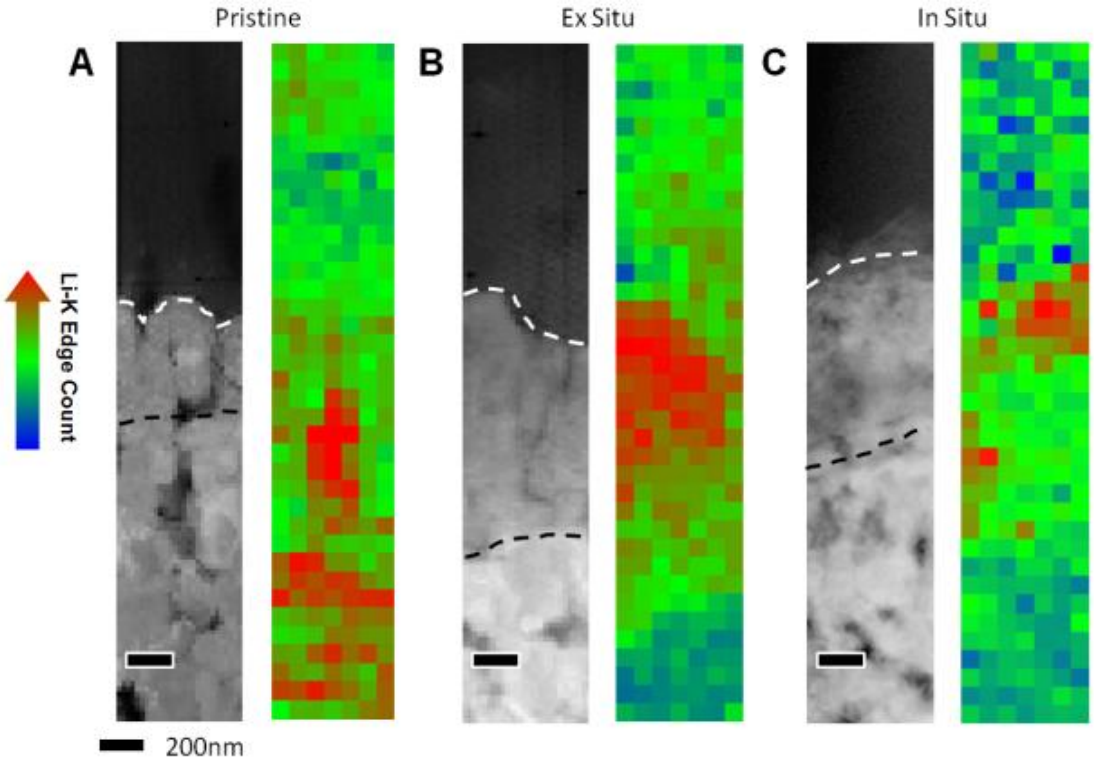

Figure 6.6 HAADF image of the nanobattery stack along with Li K-edge concentration mapping of **(a)** pristine, **(b)** *ex situ*, and **(c)** *in situ* samples with scale bar represents 200 nm.

Figure 6.7 shows selected spectra taken from LiPON, disordered LCO layer, ordered LCO layer, and their interfaces from the three samples. For the *in situ* sample, Li-K edge intensity is fairly low in LiPON due to *in situ* charged LiPON that is more sensitive to beam effects. After electrochemical charging, small changes in the solid state electrolyte can cause this particular region of the sample to be more susceptible to e-beam induced charging and heating since the electrolyte is inherently more

insulating than the electrodes. This can result in beam damage even in the optimized beam conditions. These findings must be taken into consideration along with more quantitative high loss EELS analysis to complement the interpretation.

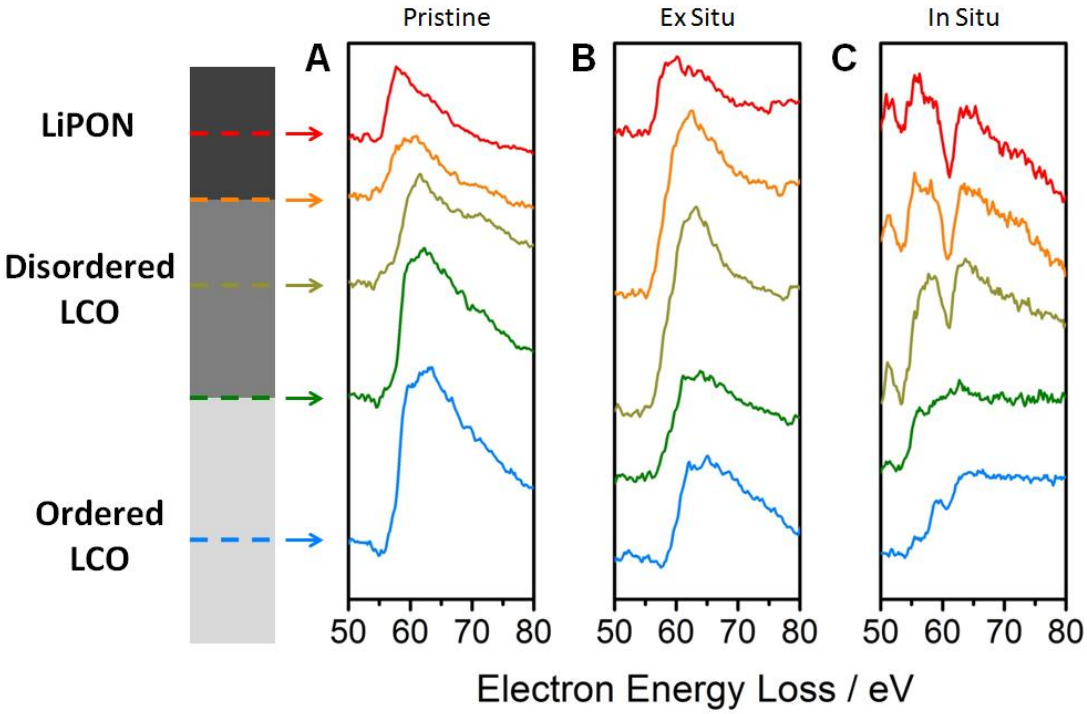

Figure 6.7 Li K-edge spectra from various parts of the layers are displayed for (d) pristine, (e) *ex situ*, and (f) *in situ* samples.

Furthermore, high loss EELS conducted on LCO layers revealed chemical changes in Co-O bonding structure during lithium ion transport. By simultaneously probing O-K edge and Co-L edge, we can observe changes in chemical bonding between oxygen 2p orbitals and cobalt 3d orbitals.[105] Through theoretical calculations and experimental results, it has been demonstrated that O-K pre-edge is a strong indicator of hybridized bonding between transition metal atom and oxygen atom.[106-108] Conversely, disappearance of O-K pre-edge is normally accompanied

by formation of oxygen vacancies, structural changes such as transition metal migration, and reduction of transition metal resulting in ionic bonding that occurs in rocksalt structures.[109-112] Additionally, analysis of the ratio between Co L_3 and L_2 white lines is complementary to changes in O-K edge as the hybridization of oxygen 2p and cobalt 3d is highly affected by the oxidation state of the cobalt ion. Upon analyzing these high loss EELS features of the three samples, we can begin to understand the chemical changes that occur *in situ* and *ex situ*.

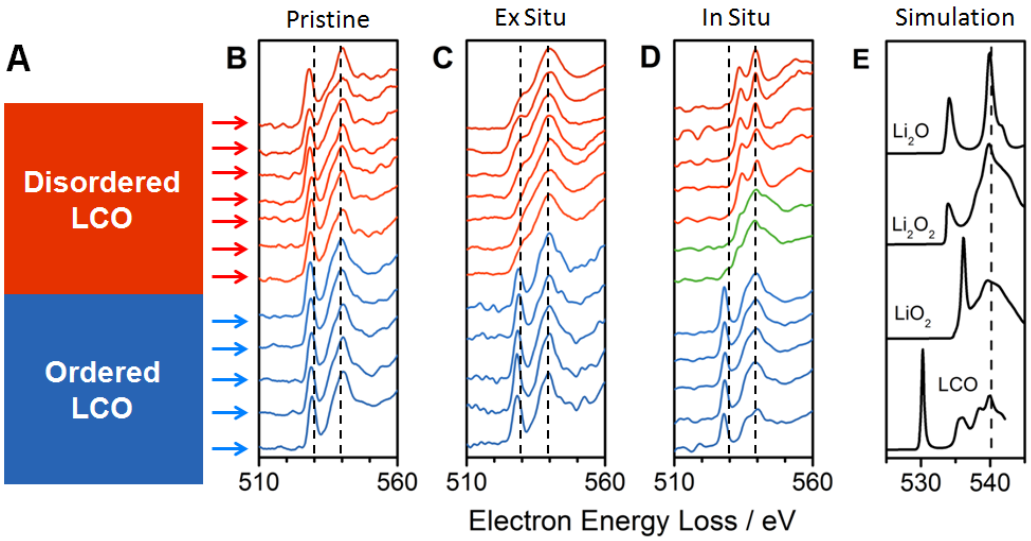

Figure 6.8 O-K edge Electron Energy Loss Spectra. a, Schematic of the spatial location of each line scan. b-d, O-K edge from the disordered LCO layer (red) and ordered LCO layer (blue) are shown for (b) pristine sample, (c) *ex situ* sample, and (d) *in situ* sample. The green spectra show O-K edge from the disordered LCO/ordered LCO interface. e, FEFF9 EELS simulation of $LiCoO_2$, Li_2O, Li_2O_2, LiO_2 O-K edge.

We analyzed the high loss edges at various positions of the LCO layers (Figure 6.8A) in the three samples to observe changes in the chemical bonding of oxygen with cobalt. In the pristine sample (Figure 6.8B), O-K pre-edge (~530 eV) is present in the disordered LCO layer as well as the ordered LCO layer even though the interfacial layer is highly disordered. This implies that the local cobalt and oxygen bonding in the

pristine disordered LCO layer is still similar to the hybridization of cobalt 3d and oxygen 2p orbitals observed in typical layered lithium cobalt oxide. Co L_3/L_2 ratio (Figure 6.9 red line) expectedly remains fairly stable around ~2.15 which corresponds to mostly Co^{3+} throughout both the LCO layers.[113] In the *ex situ* sample (Figure 6.8C), oxygen evolution after relaxation and air exposure during transfer from FIB to TEM cause O-K pre-edge to decrease significantly in the disordered LCO layer. After enough relaxation time, the combination of CoO rocksalt formation as observed by SAED of the disordered LCO layer in *ex situ* charged nanobattery (Figure 6.10) along with oxygen evolution reaction resulted in a more ionic bond between Co 3d orbital and O 2p orbital leading to a decrease of O-K pre-edge intensity. This chemical change can also be confirmed by the increase of Co L_3/L_2 ratio (Figure 6.9 green line) to over 3.0 in the disordered layer, consistent with reduced cobalt in CoO rocksalt.

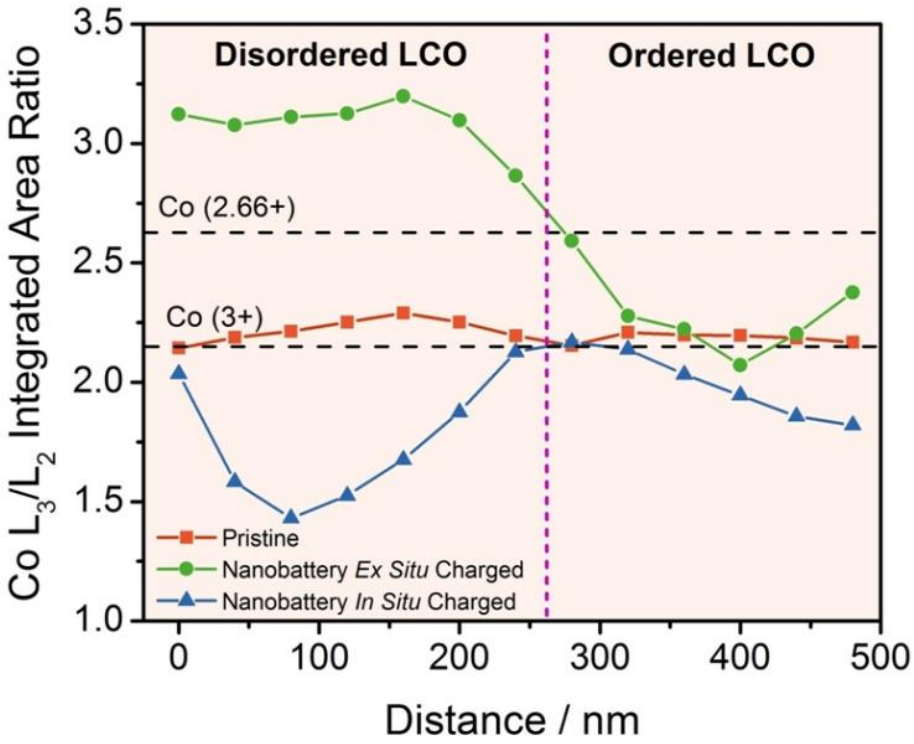

Figure 6.9 Co L_3/L_2 ratio analysis of Electron Energy Loss Spectra. The Co L_3/L_2 ratios calculated by a two-step method in the ratio of 2:1 to account for level degeneracy are shown. As cobalt becomes more oxidized, the ratio shifts to a lower value and vise versa. The dotted line denotes the separation between the disordered LCO layer and the ordered LCO layer.

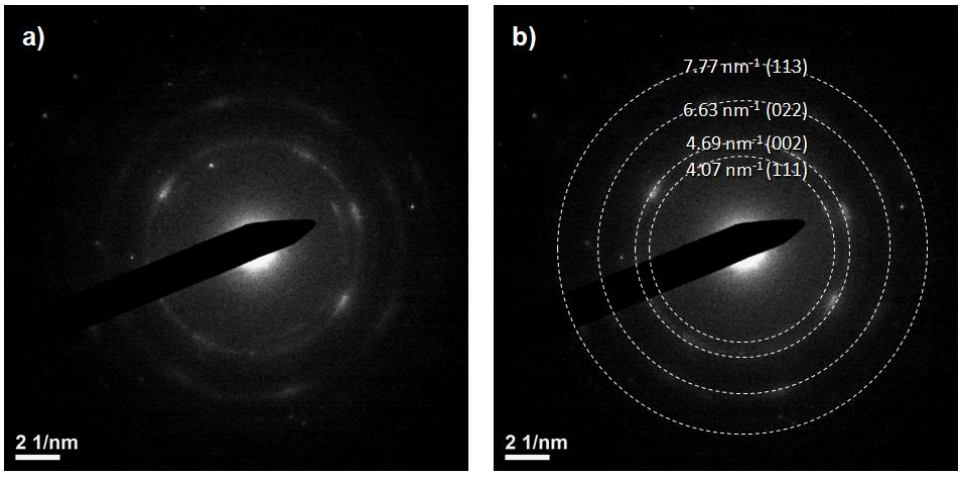

Figure 6.10 Selected area electron diffraction of the disordered LCO layer of a full cell cycled thin film battery. The diffraction spots of the layer show four rings that can be indexed to CoO rocksalt structure. (A) is the original pattern, and (B) has the rings corresponding to CoO shown.

More importantly, chemical changes that occur in the disordered layer that can be missed if the characterization is done *ex situ*. O-K pre-edge shifts to a higher energy loss in the disordered LCO layer of the *in situ* sample (Figure 6.8D). During *in situ* charging, accumulated lithium ions react with oxygen to form phase separated Li_2O or Li_2O_2. From EELS simulations using FEFF9 of O-K edge[114] based on lithium oxide and lithium peroxide (Figure 6.8E), we can see that O-K pre-edge shifts to a higher energy level of ~535eV which is consistent with *in situ* observations. It is important to note that in bulk, artifact free soft X-ray absorption spectroscopy of lithium oxide, the O-K pre-edge shift is also confirmed.[115] Thus, the shift of O-K pre-edge in the *in situ* sample is indeed caused by formation of lithium oxides and not a result of beam artifacts. At the same time, the local CoO_6 octahedron in the pristine disordered LCO is destroyed during charging with buildup of lithium oxides. Lithium oxide species formed during the *in situ* charge will react with CO_2 and H_2O present in the air to form neutral oxygen molecules, Li_2CO_3, and LiOH which further reacts to form Li_2CO_3. These factors result in the decrease of O-K pre-edge in the *ex situ* interfacial layer. It is interesting to note that at the interface between the disordered LCO layer and the ordered LCO layer of the *in situ* sample (green spectra in Figure 6.8D), O-K pre-edge has decreased in intensity. It is possible that oxygen evolution reaction and CoO formation start at this interface and propagate through the disordered LCO layer.

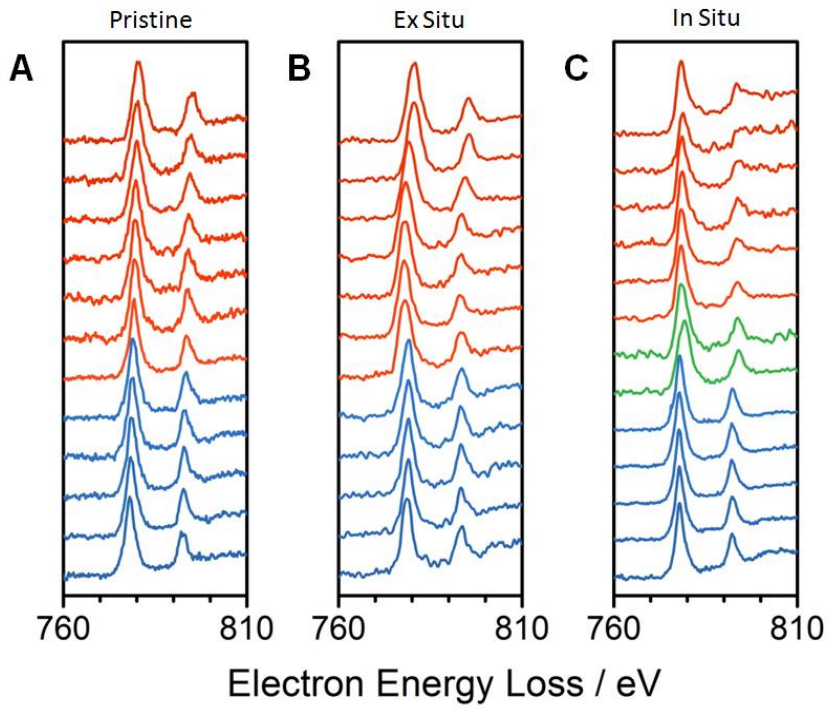

Figure 6.11 Co-L edge of EELS spectra from all three samples. The Co-L edge in (a) Pristine Sample, (b) *ex situ* sample, and (c) *in situ* sample are shown.

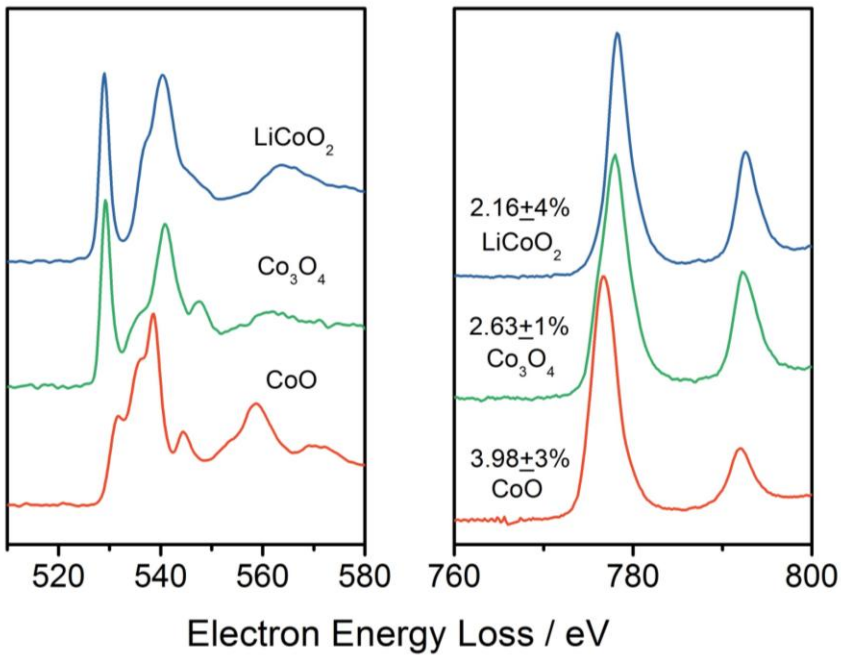

Figure 6.12 High loss spectra taken from CoO, Co_3O_4, and $LiCoO_2$ standards

The raw spectra of Co-L edge of three samples are shown in Figure 6.11. Using standards of LCO, Co_3O_4, and CoO, the L_3/L_2 ratios were calculated for Co^{3+}, $Co^{2.66+}$, and Co^{2+} respectively (Figure 6.12). We also observed Co L_3/L_2 ratio of the *in situ* sample (Figure 6.9 blue line) decreases to ~1.75 in the ordered LCO layer indicating slight oxidation of cobalt. On the other hand, the disordered LCO layer showed highly oxidized cobalt as indicated by a L_3/L_2 ratio of ~1.5 at the center of the disordered layer. There has not been enough relaxation time for oxygen evolution reaction to occur in order to charge balance. At the interface of disordered and ordered LCO layer of the *in situ* sample, we see that L_3/L_2 ratio increases again to ~2.25 confirming that oxygen evolution and CoO formation reactions begin at this interface as observed by O-K edge. Given enough relaxation time, oxygen evolution acts as electron donors that reduce oxidized cobalt atoms as rocksalt cobalt oxide forms. Although references of Co L_3/L_2 ratio for highly oxidized cobalt have been elusive due to the unstable nature of tetravalent cobalt,[116] we can take advantage of galvanostatic charge to estimate the average cobalt oxidation state. From Figure 6.2C, we estimate a total charge of 60 $\mu Ah/cm^2$ was needed to charge the cell to 4.2V. While this is far from the full capacity of the cathode, it is close to the full capacity of the silicon anode. Nonetheless, we can estimate an overall extraction of 0.21 Li ions per unit of LCO and a cobalt oxidation state of +3.21. With galvanostatic charging, we are able to correlate spectroscopic observations with the lithium content of the electrochemical system.

As seen from the STEM-EELS characterization, the disordered LCO layer is present in the pristine sample and behaves very differently from the ordered LCO layer. Firstly, the disordered layer is not caused by damages from FIB processing; as selected area electron diffraction on a FIB processed LCO thin film sample without LiPON showed crystalline structure at the surface of the film (Figure 6.13). Additionally, energy of the sputtered atoms in RF sputtering, in the range of tens of eV, is much less than 30 kV used in FIB. [117, 118] Hence, it is unlikely that the disordered layer formed as a result of the sputter deposition process of LiPON on LCO. We speculate that such a disordered structure could form as a result of an intrinsic chemical reaction between deposited LCO and LiPON causing structural changes.[92] Similarly, LiPON deposition on $LiMn_2O_4$ thin films have been shown to initially delithiate the spinel material.[119] This observation implies that it is important for the cathode material to be chemically and electrochemically stable when paired with LiPON electrolyte.

Presence of the disordered layer can have major effects on the performance of the battery. The dQ/dV analysis of full cell voltage profile clearly reveals the existence of two redox peaks at 3.55V and 3.60V on the first charge that do not provide reversible discharge capacity and do not appear on subsequent cycles (Figure 6.14). A significant portion of this first cycle full cell irreversible capacity of solid-state batteries could be due to lithium accumulation and chemical changes in the interfacial layer, as well as first cycle irreversibility of the silicon anode. It has been shown that silicon thin films of <100nm thickness has ~20% first cycle irreversibility.[14, 18,

120] Surprisingly this disordered layer has rather good lithium ion transport, though the atomistic details of this layer are still lacking. Using additional commercially RF sputtered LCO/LiPON/Li cells, we further observed that the disordered layer grows significantly thicker when cycled at 80 ^{o}C as compared to those cycled at 25 ^{o}C. The growth of this disordered interfacial layer is accompanied by rapid decay in reversible capacity after 250 cycles. Analysis of impedance spectroscopy taken every 50 cycle at the charged state showed continuously increasing interfacial resistances of the cells. These detailed findings will be published elsewhere[121].

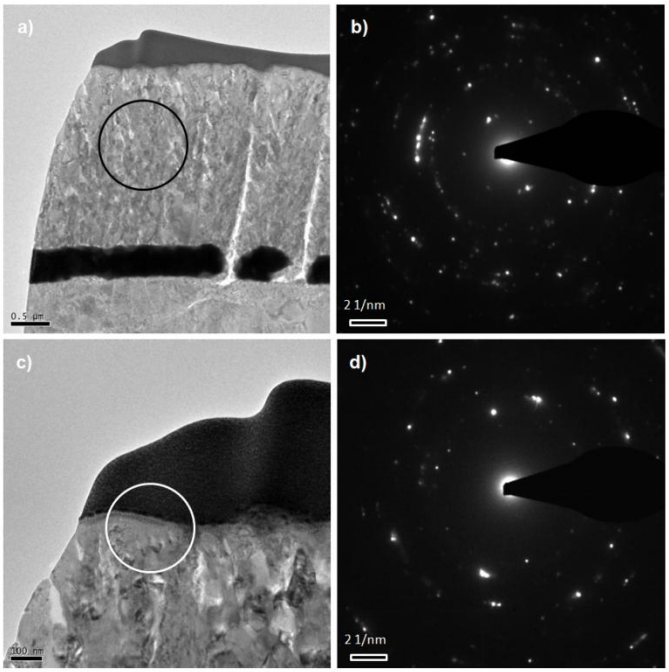

Figure 6.13 TEM image and SAED of crystalline LCO thin film processed by FIB. TEM and SAED of bulk LCO thin films are shown in (A) and (B). TEM and SAED of LCO thin film surface are shown in (C) and (D).

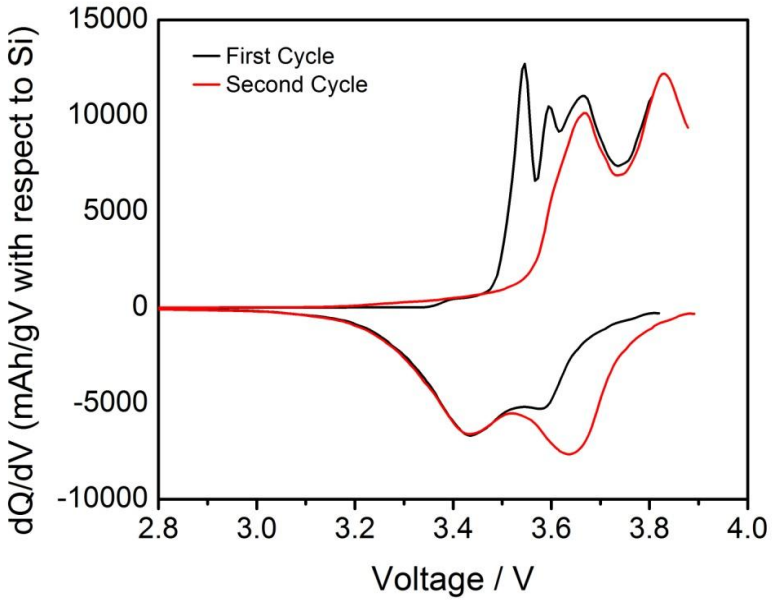

Figure 6.14 dQ/dV plot of the first two cycles of the solid-state thin film battery. The additional two redox peaks at ~3.5V and ~3.6V on the first cycle could be attributed to reactions in the disordered LCO layer.

Finally, differences between *in situ* and *ex situ* observations of O-K edge and Co-L edge highlight the importance of dynamic *in situ* characterization. *In situ* characterization monitors electronic structure changes in interfaces without prolonged time relaxation, air exposure, and other factors that could interfere with sample properties. The combination of electron diffraction, STEM imaging, and analytical EELS characterization has given critical insight into the impact of interfacial phenomena in first cycle irreversible capacity loss of solid-state batteries. With recent improvements in electron microscope and direct detectors, greater energy resolution (<0.1 eV) and higher temporal resolution (sub-millisecond) can be achieved.

Analytical information gathered through this novel technique will help scientists in the field of all-solid-state battery to establish new design rules for solid-solid interfaces and improve electrochemical performance and lifetime of such systems.

6.5 Conclusion

In conclusion, STEM-EELS characterization of solid-state batteries revealed a disordered interfacial layer between cathode and electrolyte that accumulates lithium and evolves to rocksalt CoO after cycling. This layer could form as a result of depositing cathode materials that are structurally unstable in highly delithiated states on LiPON. With *in situ* STEM-EELS characterization of solid-solid interfaces enabled through our unique procedure, we observed Li_2O/Li_2O_2 formation as an intermediate compound of oxygen evolution reaction as the disordered interfacial layer eventually formed a rocksalt structure *ex situ*. Increasing thickness of this layer would lead to rapid capacity decay as more of the cathode will be rendered electrochemically inactive. Since oxygen evolution reaction at high voltage is common in several oxide based cathode materials, it is critical to solve interfacial issues for better safety and long term cycling. Our novel methodology developed to study dynamics at the nanoscale could be applied to various solid-state devices beyond solid-state batteries, such as solid-state solar cells, metal air fuel cells, and field effect transistors.

Chapter 6, in full, is a reprint of the material "*In situ* STEM-EELS Observation of Nanoscale Interfacial Phenomena in All-Solid-State Batteries" as it appears in Nano Letters, Ziying Wang, Dhamodaran Santhanagopalan, Wei Zhang, Feng Wang, Huolin L. Xin, Kai He, Juchuan Li, Nancy Dudney, Ying Shirley Meng, 2016, 16 (6), 3760-

3767. The dissertation author was a co-primary investigator and author of this paper. All the experiment and writing were conducted by the author except for STEM-EELS data collection and the particular *in situ* charge.

Chapter 7. Ex situ Characterization of Cathode-Electrolyte Interface

All-solid-state lithium-ion batteries have the potential to not only push the current limits of energy density by utilizing Li metal, but also improve safety by avoiding flammable organic electrolyte. However, understanding the role of solid electrolyte – electrode interfaces will be critical to improve performance. In this study, we conducted long term cycling on commercially available lithium cobalt oxide (LCO)/lithium phosphorus oxynitride (LiPON)/lithium (Li) cells at elevated temperature to investigate the interfacial phenomena that lead to capacity decay. STEM-EELS analysis of samples revealed a previously unreported disordered layer between the LCO cathode and LiPON electrolyte. This electrochemically inactive layer grew in thickness leading to loss of capacity and increase of interfacial resistance when cycled at 80 ºC. The stabilization of this layer through interfacial engineering is crucial to improve the long term performance of thin-film batteries especially under thermal stress.

7.1 Introduction

Lithium-ion batteries have become the focal point of energy storage devices as portable electronics and electric vehicles applications demand ever increasing energy densities both in terms of weight and volume. While the cost per Watt-hour of commercial batteries has decreased faster than expected due to high production and more efficient manufacturing [122], specific and volumetric energy densities have

only increased 7-8% per year [81]. To truly relieve range anxiety, specific energy density higher than the current ~200 Wh kg^{-1} is needed. To satisfy this demand, lithium-ion batteries utilizing solid state electrolytes show promise of a new paradigm shift in energy storage technologies. The introduction of solid state electrolyte could, in principle, yield many advantages over conventional lithium-ion batteries. Foremost, lithium metal can be used as the anode along with a high voltage cathode to boost energy density as the solid state electrolyte would prevent lithium dendrite formation. Secondly, removal of flammable liquid electrolytes greatly improves the inherent safety of the battery.

While thin-film lithium-ion batteries utilizing solid state electrolytes have begun to be commercialized in a variety of micro-devices such as radio-frequency identification tags, microelectromechanical devices, sensors, and lab-on-a-chip systems [123, 124], significant research on the chemical and electrochemical stability of the solid electrolyte – electrode interfaces is needed before big scale application in energy storage. Indeed, solid electrolyte – electrode interfacial resistance has now become the limiting factor in many systems [81]. Recent computational studies have shown that various interfaces are not always stable chemically or electrochemically leading to loss of capacity and increase in impedance [92, 93]. Fortunately, thin-film batteries offer a convenient platform to investigate and gain insight into these interfacial phenomena due to their well defined geometry. The anode, electrolyte and cathode layers are clearly distinct over a large area, allowing for simplified analysis of various interfaces. Since the introduction of the first thin-film lithium-ion battery

using the lithium cobalt oxide (LCO)/lithium phosphorus oxynitride (LiPON)/lithium (Li) chemistry [6, 125], various reports have highlighted the role of LCO/LiPON interfacial resistance. Iriyama *et al.* has claimed that thermal treatment of the cell after LiPON deposition can reduce the interfacial resistance from 7925 Ω cm^2 to 125 Ω cm^2 [89, 90]. Additionally, a recent paper by Haruta *et al.* has shown that an off-axis deposition of LiPON can greatly reduce the interfacial resistance down to 8.5 Ω cm^2 [126]. However, all these experiments were based on electrochemical measurements via electrochemical impedance spectroscopy (EIS) and did not identify the source of impedance.

In this study, we used Scanning Transmission Electron Microscopy (STEM) and Electron Energy Loss Spectroscopy (EELS) analysis to study the LCO and LiPON interface in commercially available LCO/LiPON/Li cells. When these cells were cycled at an elevated temperature of 80 ºC, we observed continuous capacity decay and an increasing interfacial resistance contrasting stable cycling at 25 °C. Through TEM analysis of the LCO/LiPON interface, we were able to observe a distinct disordered LCO layer between the ordered LCO bulk and LiPON inherent to the solid electrolyte – electrode interface. The growth of this layer during high temperature cycling caused increasing interfacial resistance between LCO and LiPON as observed by electrochemical impedance spectroscopy. These results indicate that proper engineering of the electrode/electrolyte interface is essential for long term cell performance.

7.2 Experimental

7.2.1 Sample preparation and electrochemical testing

The all-solid-state thin-film batteries used in this study were supplied by STMicroelectronics. The cells were composed of deposited LCO, LiPON, Li layers on a mica substrate. The LCO layer is 8μm thick. The exact thicknesses of LiPON and Li layers are omitted for industrial purposes but are on the orders of a few microns. The cells were then encapsulated to prevent air exposure. The current collectors were platinum and copper for the cathode and anode, respectively. Deposition of LCO and LiPON layers were done via medium-frequency & radio-frequency sputtering, respectively, while Li was thermally evaporated. A schematic of the battery is shown in Figure 7.1a. The specific details about the deposition process are omitted for industrial purposes. The packaged thin film batteries have 1 inch x 1 inch footprint and were cycled with a rate of 1C at 25 ºC or 80 ºC via a potentiostat/galvanostat with a frequency response analyzer (Biologic SP-200). Electrochemical Impedance Spectroscopy (EIS) was conducted at room temperature every 50 cycles on each cell at the charged state. The frequency sweep was conducted from 1 MHz to 10 mHz with an amplitude of 10 mV and fitted with a complex non-linear least square fitting method. Two additional cells were aged at 60 °C for 2500 hours without cycling. One cell was left in the discharged state at 3.6 V and the other was left in the charged state at 4.2 V after a single charge. The cells were then processed using a FEI Helios focused ion beam (FIB) to produce an *ex situ* cross section of the battery stack [101]. Subsequently, these samples were characterized in a JOEL 2100F analytical electron

microscope with a 200 kV beam with an approximate energy resolution of 1 eV in electron energy loss spectra.

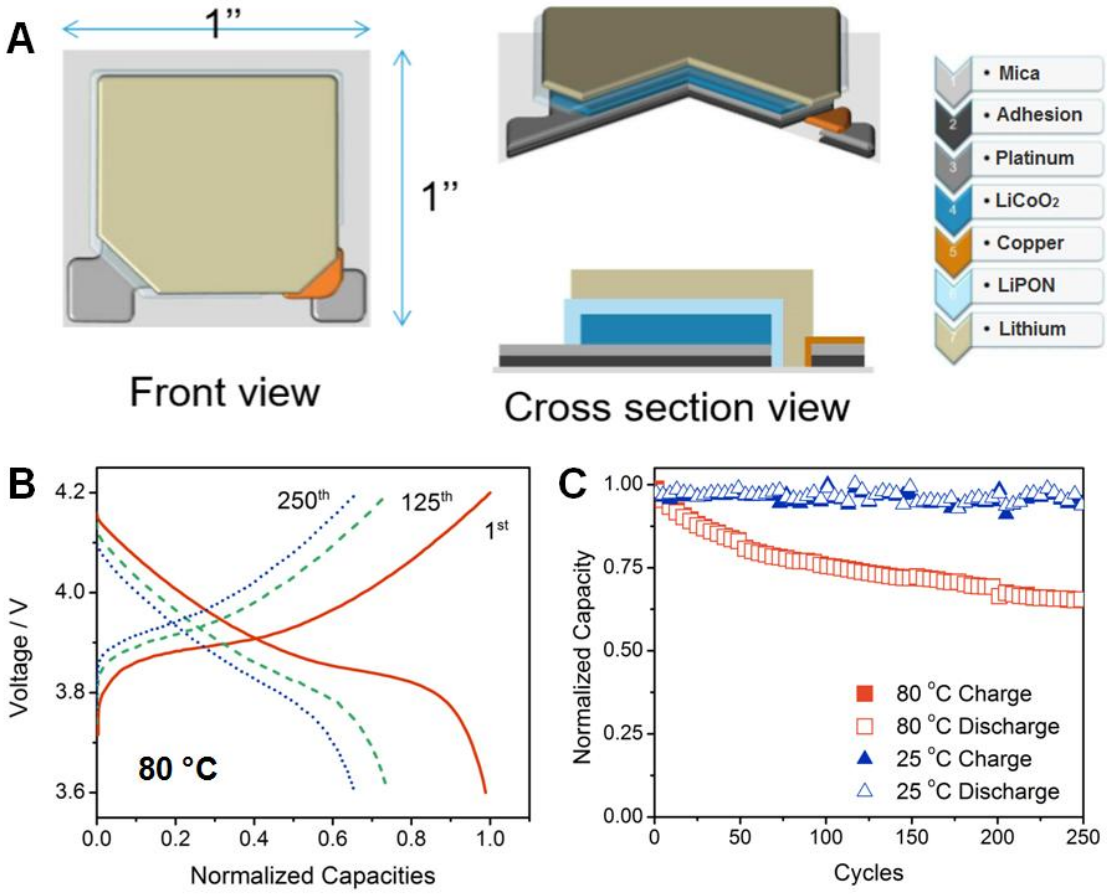

Figure 7.1 a) Schematic of the thin-film battery. The all-solid-state thin-film battery consists of a lithium cobalt oxide (LCO) cathode, lithium phosphorus oxynitride (LiPON) electrolyte, and lithium anode. The cell is encapsulated to prevent air exposure. b) Cycling profile of the 80 °C cycled cell at 1st, 125th, and 250th cycle. c) Cycling capacity of the two cells over 250 cycles. The cell cycled at 80 ºC quickly loses ~35% of its capacity over 250 cycles, while the cell cycled at 25 ºC retains its capacity.

7.2.2 Scanning transmission electron microscopy collection

STEM-EELS images and spectrums were collected on a JEOL 2100F located at the Center for Functional Nanomaterials at Brookhaven National Laboratory. The

beam energy is 200 kV. For all spectrums, the second smallest aperture was used where the beam density measured by the fluorescent screen was 2.4 pA cm^{-2}. The beam diameter was focused to approximately 0.2 nm. The energy resolution of the electron energy loss spectra is approximately 1 eV. For low loss mapping and spectrums, a 0.1 s pixel dwell time and 0.2 eV per channel dispersion were used. For high loss spectrums, a 20 s pixel dwell time, and 0.2 eV per channel dispersion were used. L_3/L_2 ratios were calculated by taking second derivative of the Co-L edge and comparing the height of the respective peaks for L_3 and L_2 in the second derivative. Selected area electron diffraction (SAED) was collected with the smallest objective aperture (~150 nm in diameter) to avoid diffraction from multiple layers. Focused Ion Beam processing of the samples were conducted on a FEI Helios nanolab. The maximum ion beam current used for regular cross sections is ~3 nA while the pixel dwell time is limited to 100 ns. The samples were extracted out of the full thin-film battery through typical lamella fabrication and thinned down to ~80 nm using 0.3 nA cleaning cross sections from both sides of the lamella.

7.2.3 Electron Energy Loss Spectroscopy Simulation by FEFF9

Electron energy loss spectroscopy simulations were conducted using FEFF9 software. The crystal structures of $LiCoO_2$, Li_2O, Li_2O_2, and LiO_2 were taken from icsd database for crystalline structures. The simulations were conducted using 200 keV beam energy, 10 mrads for collection and convergence angles. xkmax value of 4, xkstep value of 0.02, estep value of 0.01 were used. Hedin Lundqvist exchange and RPA corehole were used for electron core interactions.

7.3 Results and Discussion

7.3.1 Cell cycling performance

Cycling profile of the thin-film battery cycled at 80 ºC is shown in Figure 7.1b. The cell was cycled between 3.6 V and 4.2 V and shows the characteristic voltage profile of the LCO intercalation reaction. Electrochemical curves show a plateau at approximately 3.9 V attributed to a first order phase transition between two hexagonal phases with different c lattice parameter due to the expansion of oxygen layer spacing [12, 13]. The cell cycled at 80 ºC lost ~35% of the original capacity over 250 cycles. In contrast, the cell cycled at 25 ºC retained its capacity over the 250 cycles as seen in Figure 7.1c. These charge/discharge characteristics show the distinctive behavior of batteries composed of LCO and confirm the good performance of the fabricated thin-film batteries.

7.3.2 TEM analysis

To fully understand the underlying mechanism of capacity decay, we used STEM-EELS characterization to locally probe the LCO/LiPON interface. Using standard FIB liftout techniques, three liftouts were made from the pristine, 25 ºC, and 80 ºC cycled samples, and thinned down to ~80 nm for TEM analysis, shown in Figure 7.2a-c. It was observed that all three samples have an additional interfacial layer between LiPON and LCO. Close up TEM images of the cathode-electrolyte interfaces that more clearly distinguish the interfacial layers are shown in Figure 7.2d-f. The imaging contrast between this additional layer and LCO is small as both layers are made of similar chemical compositions. This is confirmed by analysis of EELS

taken from the interfacial layer, bulk LCO, and LiPON, both the interfacial layer and bulk LCO contain lithium, cobalt, oxygen but not phosphorus (Figure 7.3). However, structural and chemical bonding differences between the interfacial layer and bulk LCO are drastic. Firstly, selected area electron diffractions conducted on the interfacial layers of all three samples did not show diffraction patterns that would originate from highly crystalline layered lithium cobalt oxide particles (Figure 7.4a-c), contrasting clear polycrystalline diffraction rings from the bulk LCO layer (Figure 7.4d). Radial integration of the diffraction patterns comparing between the pristine, 25 °C cycled, and 80 °C cycled samples (Figure 7.5) shows that the interfacial layer contains highly disordered material. Weak diffraction signals from the pristine and 25 °C cycled samples align with reciprocal spacing of CoO rocksalt indicating that the interfacial layer contains a disordered rocksalt like cobalt oxide phase; while diffraction signals from the 80 °C align with reciprocal spacing of Li_2O. These results suggest that during cycling at elevated temperatures, a portion of the lithium and oxygen in the interfacial layer formed crystalline Li_2O along with the disordered cobalt oxide. Hereinafter, this interfacial layer and bulk LCO will be referred to as the disordered LCO and ordered LCO layers, respectively.

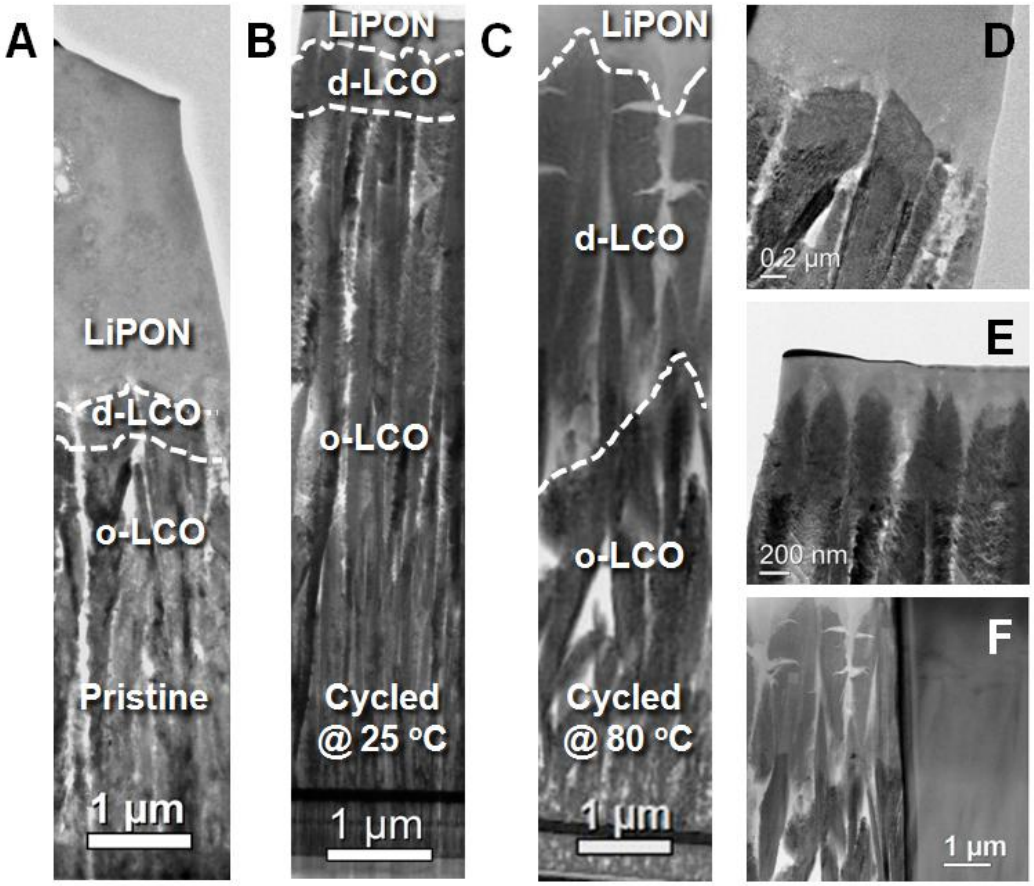

Figure 7.2 Cross-sectional TEM images of the thin-film battery showing the cathode/electrolyte interface. a) pristine LCO/LiPON interface showing ~300 nm thick disordered layer. b) 25 °C cycled LCO/LiPON interface showing minimal change to the disordered layer. c) 80 °C cycled LCO/LiPON interface showing significant growth of the electrochemically inactive disordered layer. Close up TEM images of the cathode/electrolyte interface for the pristine, 25 °C, and 80 °C samples are shown in d)-e) respectively.

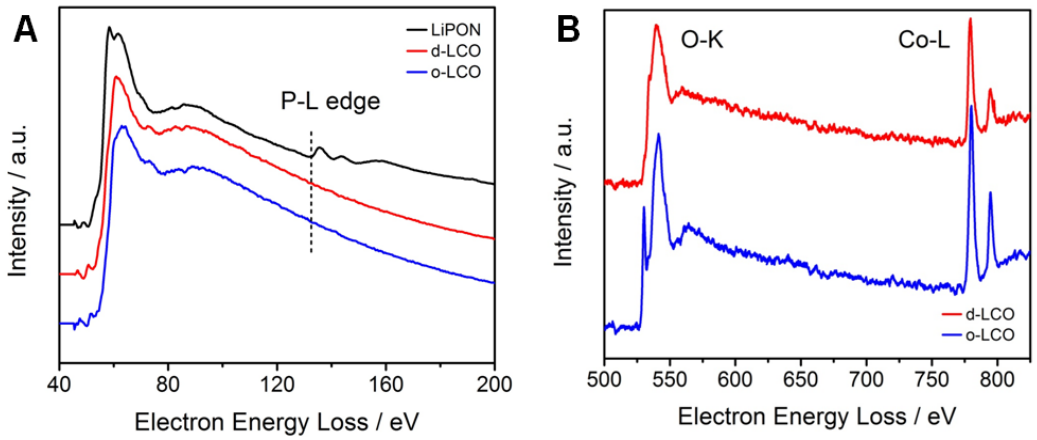

Figure 7.3 Electron energy loss spectra taken from various parts of the thin film battery sample. a) Low loss EELS shows that only the LiPON electrolyte contains the P-L edge. b) High loss EELS shows that both the disordered and ordered LCO layers contain O-K edge and Co-L edge.

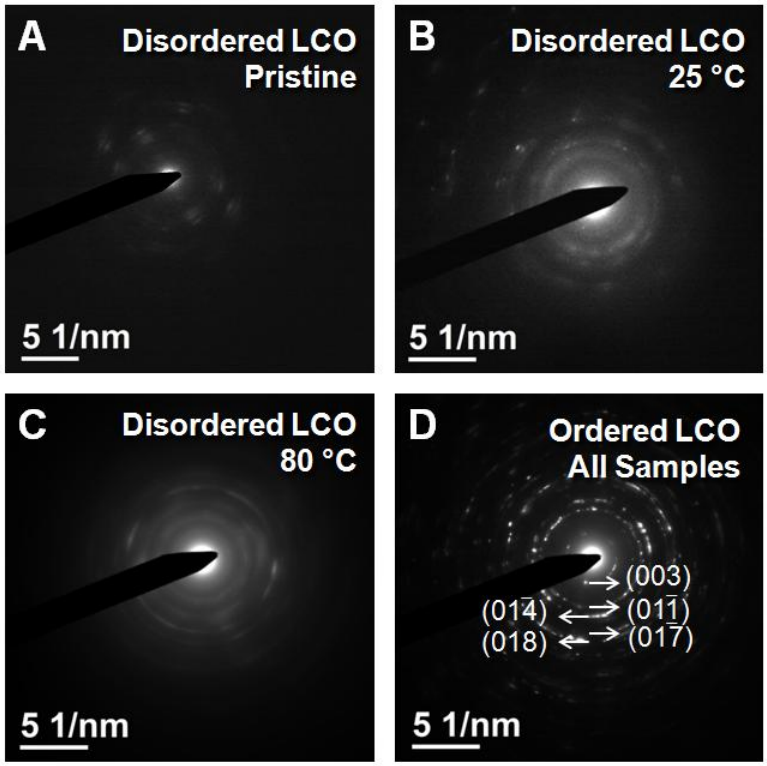

Figure 7.4 Selected area electron diffractions taken from the disordered LCO layer of the pristine, 25 °C, 80 °C samples are shown in a)-c). The disordered layers all show highly disordered diffraction rings while the ordered LCO layer show highly crystalline diffraction rings corresponding to layered oxide crystal structure as shown in d).

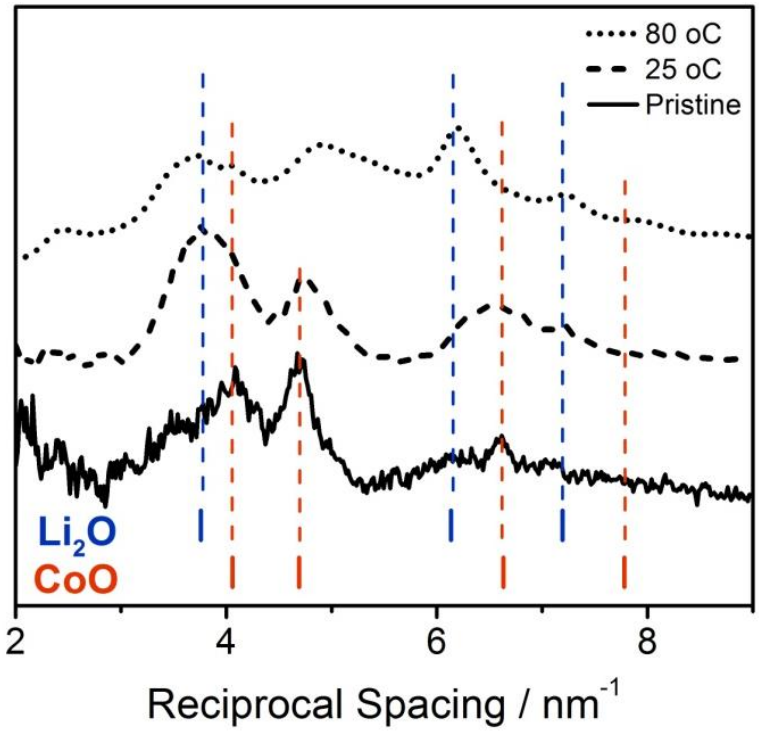

Figure 7.5 Radial intensity extracted from the selected area electron diffraction of the disordered LCO layer from the pristine, 25 °C, and 80 °C samples. In the pristine and 25 °C samples, the peak intensities align with peaks of CoO rocksalt indicating a highly disordered rocksalt like cobalt oxide phase. In the 80 °C sample, additional peak intensities align with Li_2O rocksalt crystal structure.

Comparing the 25 °C and 80 ºC cycled samples (Figure 7.2b-c), it is very apparent that the disordered layer has grown significantly at higher temperatures and has consumed approximately 4 µm of the cathode thickness. It is hypothesized that such growth will decrease the overall capacity of the cell. Without the proper layered oxide structure in the disordered layer, lithium-ions cannot be stored reversibly. However, due to the disordered nature of this interfacial layer, lithium conduction is still possible via percolation through channels that could arise in regions with lithium excess stoichiometry, as proposed by Lee *et al* [102].

7.3.3 STEM-EELS analysis

It is important to probe the chemical bonding of elements in the disordered and ordered layers to analyze the local environment of atoms. Bonding between lithium, cobalt and oxygen atoms can have a large effect on the occupancy and energy of their electronic orbitals, which in turn can be characterized by electron energy loss spectroscopy (EELS). Low loss electron energy loss spectra taken from the three samples are shown in Figure 7.6a. As the Li-K edge and Co-M edge are close in energy value and highly convoluted together, they must be analyzed together in low loss spectra. In the ordered LCO layer of all three samples, the low loss edges show peak shape corresponding to spectrum taken from crystalline lithium cobalt oxide standards. There are small but subtle differences of the low loss edges from the disordered LCO layers. In the pristine and 25 °C cycled sample, the low loss edge contains a sharp peak ~60 eV resembling spectrum taken from crystalline cobalt oxide rocksalt standard (Figure 6.5). However in the 80 °C cycled sample, there is a much stronger edge shoulder before the onset of the main edge and this peak shape is seen previously in low loss EELS of Li_2O standards [103]. These results compliment our earlier observation of disordered rocksalt like cobalt oxide in the disordered layer of pristine and 25 °C samples and presence of Li_2O in the disordered layer of 80 °C sample.

Additionally, the O-K edge is very indicative of how the oxygen atom bonds to surrounding cations such as cobalt or lithium [105-108]. O-K edge spectra taken from the disordered and ordered layer of the three samples are shown in Figure 7.6b; and as

expected, all three spectra from the ordered layer show characteristic O-K pre-edge corresponding to hybridization of Co 3d and O 2p orbitals in LCO (Figure 6.12). However in the pristine cell, the O-K pre-edge in the disordered layer is already absent as compared to the ordered layer. This implies that in these particular samples, the Co-O hybridization bonding has already converted to a more ionic bond even in the pristine state. While there was no significant difference between the disordered layer of pristine and 25 °C sample, the O-K edge of the disordered layer in the 80 ºC cycled sample shows a doublet peak with an approximately 5eV of energy spacing. From EELS simulations using FEFF9 of the O-K edge based on lithium oxide and lithium peroxide, we see that the O-K pre-edge shifts to a higher energy level of ~535 eV which is consistent with the observed spectra of the 80 °C sample.

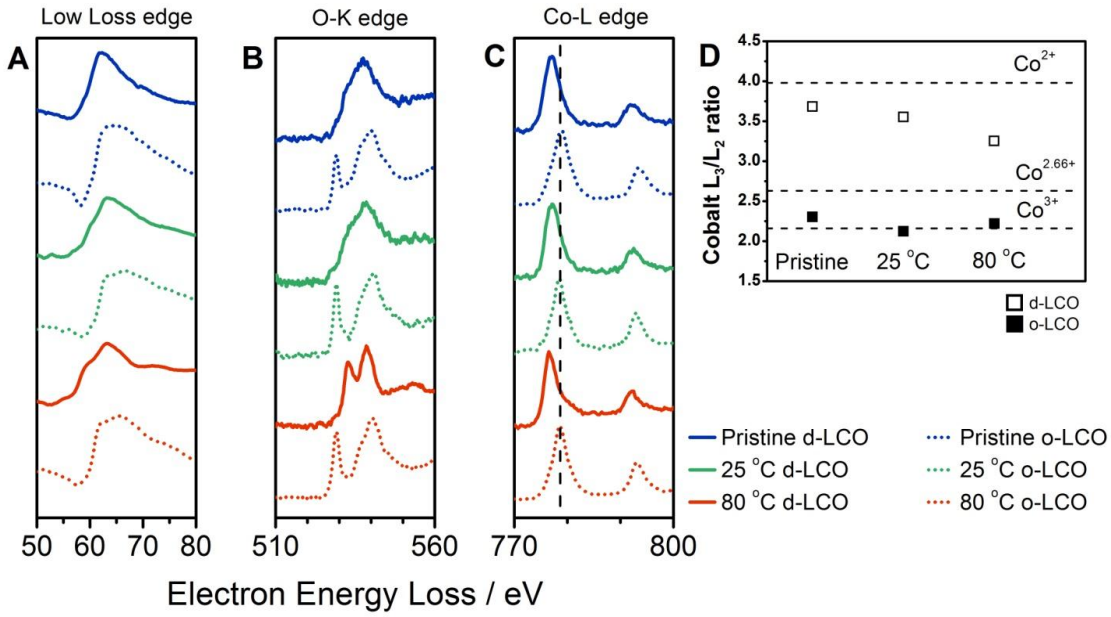

Figure 7.6 Electron energy loss spectra taken from all three samples. a) Low loss Li-K/Co-M edges, b) O-K edges, and c) Co-L edges taken from the disordered and ordered LCO layers of the pristine, 25 °C, and 80 °C samples. All the spectra taken from the ordered LCO layers show characteristic peak shapes and energies for crystalline $LiCoO_2$. Low loss Li-K/Co-M edges in the disordered LCO layer show subtle differences in the edge shoulder between the 25 °C and 80 °C sample and O-K edges show a doublet peak with 5 eV spacing in the disordered LCO layer of the 80 °C sample. Both peak shapes can be attributed to Li_2O formation. All Co-L edges from the disordered LCO layer are shifted to a lower energy level indicating reduction of cobalt.

Electron energy loss spectra of transition metal L-edge also allow quantitative analysis of the oxidation state of transition metal cations. In Figure 7.6c, the Co-L edges clearly show a shift of L_3 and L_2 edges to a lower energy level by about 1 eV in all three disordered LCO layers. Such shift is associated with transition metal cations of lower oxidation states (Figure 6.12). A more quantitative probing of the oxidation state can be obtained by calculating the L_3/L_2 ratio. Shown in Figure 7.6d, the L_3/L_2

ratio of cobalt within the ordered LCO layer remains mostly constant near ~2.2 corresponding to Co^{3+} in $LiCoO_2$. The L_3/L_2 ratio of cobalt within the disordered LCO layer, however, becomes slightly lower after cycling and much lower after cycling at 80 °C. Based on L_3/L_2 ratio calculated from $LiCoO_2$, Co_3O_4, and CoO standards, the average oxidation states of cobalt in the disordered layer of pristine, 25 °C, and 80 °C samples are estimated to be 2.1+, 2.2+, and 2.5+ respectively. Oxidation state of cobalt provides clues to the underlying mechanism of the formation and growth of the disordered layer.

7.3.4 Mechanism of disordered layer formation and growth

The disordered LCO layer is present in the pristine sample indicating that the pairing of LiPON electrolyte and $LiCoO_2$ cathode has an inherent chemical instability leading to formation of a decomposition layer. This chemical instability is also observed via theoretical computations of thermodynamic energies of decomposition products [10, 92]. After the deposition of LiPON, ~300 nm of the $LiCoO_2$ cathode film surface decompose to form a highly disordered rocksalt like cobalt oxide material as evidenced by SAED and EELS analysis. Cobalt ions within this decomposition layer are reduced to an average oxidation state of 2.1+ from 3+ through the formation of peroxide species. However, due to relatively weak intensity of O-K pre-edge in Li_2O_2 FEFF9 simulation (Figure 6.8e), only a single peak is observed for the O-K edge in both the pristine and 25 °C samples. In addition to the initial chemical decomposition, the disordered LCO layer can continue to grow into the ordered LCO layer through a combination of thermal and electrochemical activation to form a

different decomposition phase that contains more Li_2O and trivalent cobalt. It's important to first note that electrochemical activation alone does not promote the growth of the disordered LCO layer. As can be seen from the 25 °C cycled sample (Figure 7.2b), there was no change to the thickness of the disordered layer after 250 cycles. To properly compare thermal effects alone and thermal effects with electrochemical bias, two additional cells were tested without cycling. One cell was kept in the discharged state at 3.6V while the other was kept in the charged state at 4.2V after a single charge, and both cells were then heated at 60 °C for 2500 hours. TEM images of these two samples show that thermal activation alone was able to grow the disordered LCO layer to ~ 1.5 μm in the discharged sample (Figure 7.7a), while the disordered LCO layer grew to an even thicker ~ 3 μm in the charged sample (Figure 7.7b). From these two experiments, we can conclude that the main driving force for further decomposition is thermal activation and electrochemical delithiation of $LiCoO_2$ enhances the rate of decomposition. Initial heat stress during RF sputtering of LiPON on LCO could have also contributed to the initial 300 nm thickness of disordered layer. Future experiments correlating fabrication conditions and initial composition and morphology of the disordered layer could provide further insight to its formation mechanism.

Chemically, it is hypothesized that during high temperature cycling the disordered LCO layer grows through the decomposition of ordered LCO into disordered rocksalt like cobalt oxide, lithium oxide and lithium peroxide. The reduction of trivalent cobalt is charge balanced by formation of appropriate amounts

of lithium peroxide. The decomposition reaction in the disordered LCO layer of 80 °C sample can be summarized in Equation 7.1 resulting in $Co^{2.5+}$ observed through Co L_3/L_2 analysis.

$$4LiCoO_2 \rightarrow Li_2O + Li_2O_2 + Co_4O_5 \quad \text{(Equation 7.1)}$$

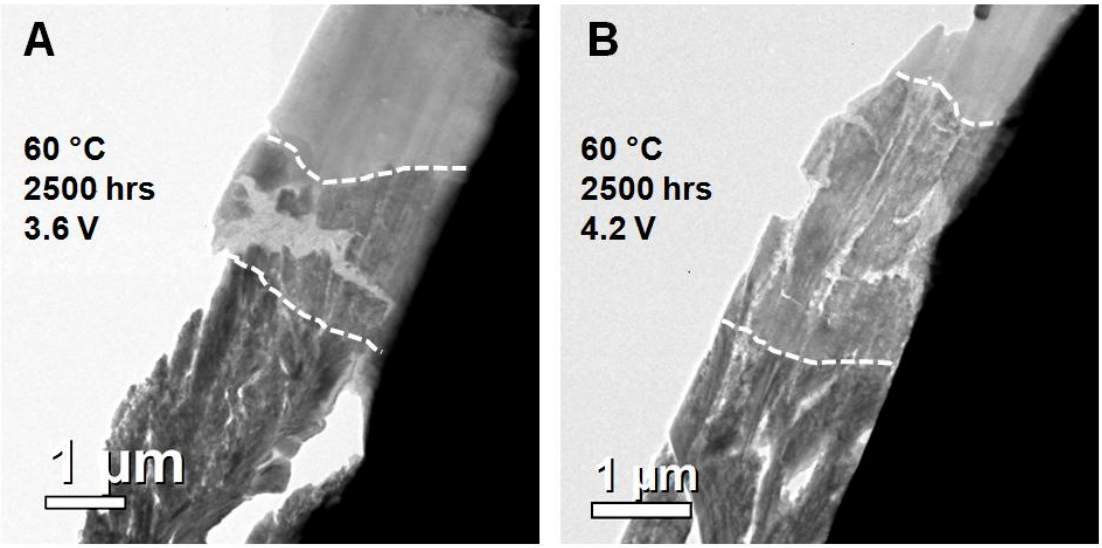

Figure 7.7 TEM images of cells aged at 60 °C for 2500 hours. One cell was kept in the discharged state (3.6 V) shown in a) while another cell was kept in the charged state (4.2 V) shown in b). The disordered LCO layer grew to about 1.5 µm in thickness in the discharged sample and about 3 µm in thickness in the charged sample.

7.3.5 Electrochemical impedance spectroscopy analysis

Electrochemical impedance spectroscopy (EIS) conducted on the cell cycled at 80 °C provides additional insight into the changes of interfacial impedance that occurs during cycling. The impedance spectra taken at the charged state every 50 cycles are shown in Figure 7.8a and show increasing interfacial impedance over 250 cycles. The impedance spectra consist of three semicircles, two in the high frequency range with characteristic frequencies of 77 kHz and 455 Hz and one in the low frequency range

with characteristic frequency of 103 mHz. The first semicircle remains constant over the entire 250 cycles and is attributed to the ionic conduction of lithium-ions in LiPON. Given the geometry of the cell, the ionic conductivity of the LiPON is estimated to be $2.1x10^{-6}$ S cm^{-1} which agrees with literature values [5]. As seen from previous literature, the interfacial resistance between Li/LiPON is negligible compared to the other interfaces and will not be included in the fitting [89, 126, 127]. The second and third semicircles can be attributed to two different charge transfer processes, which steadily increase in resistance over 250 cycles. The fitted spectra using the equivalent circuit are presented in Figure 7.8a, while Figure 7.8b exhibits the evolution of each contribution over the 250 cycles. Detailed fitting parameters are shown in Table 7.1.

Table 7.1 Equivalent circuit parameters of the 80 °C cycled all-solid-state battery at the charged state determined from non-linear least squares fitting of the impedance spectra.

			CPE_1			CPE_2			CPE_3	
	R_{cell}	$\mathbf{R_1}$	C		$\mathbf{R_2}$	C		$\mathbf{R_3}$	C	
	Ω	**Ω**	$nFs^{\eta-1}$	η	**Ω**	$\mu Fs^{\eta-1}$	η	**Ω**	$mFs^{\eta-1}$	η
Pristine	10	**51**	41.98	1	**28**	6.22	0.90	**613**	1.31	0.60
50^{th}	10	**57**	39.05	1	**47**	7.17	0.86	**1035**	1.32	0.56
100^{th}	10	**56**	39.81	1	**57**	4.63	0.90	**1223**	1.35	0.52
150^{th}	11	**57**	40.71	1	**67**	6.53	0.85	**1354**	1.29	0.53
200^{th}	10	**56**	41.60	1	**77**	6.35	0.84	**1517**	1.27	0.52
250^{th}	10	**59**	42.67	1	**132**	8.61	0.80	**1941**	0.71	0.56

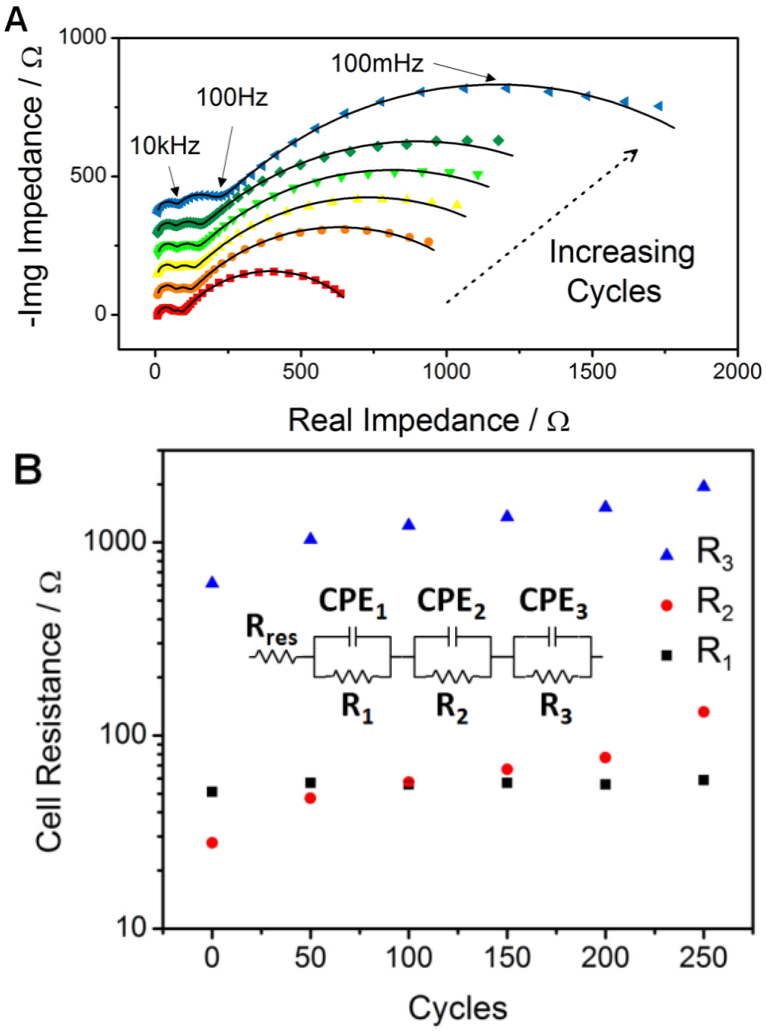

Figure 7.8 a) Electrochemical impedance spectroscopy of the 80 ºC cycled cell. The EIS spectra of the full cell taken every 50 cycles show that the interface impedance increases as the cell ages. b) The extracted values of charge transfer resistance of various processes in the full cell. R_1 is attributed to the ionic conductivity of LiPON. R_2 is attributed to the charge transfer resistance between the disordered LCO layer and LiPON while R_3 is attributed to the charge transfer resistance between the disordered LCO layer and ordered LCO layer.

Keeping the observation of the disordered layer in mind, we can precisely interpret the physical representations of the EIS data. When EIS was conducted on the electrochemical cell at the discharged state (3.6V) as shown in Figure 7.9, we do not see a third semicircle as the electrochemical Li intercalation reaction between the

ordered LCO layer and disordered LCO layer only occurs above ~3.9 V [89, 90]. Hence, the second semicircle with a characteristic frequency of 755 Hz can be attributed to charge transfer resistance between the LiPON layer and the disordered LCO layer, while the third semicircle with a characteristic frequency of 103 mHz can be attributed to charge transfer resistance between the disordered LCO layer and ordered LCO layer. As the disordered LCO layer grows in thickness upon cycling, its impedance at the LiPON and ordered LCO interfaces increases. It is also important to note that in the 25 °C cycled cell, the impedance spectra (Figure 7.10) remain mostly unchanged over 250 cycles mirroring the lack of growth of the disordered LCO layer.

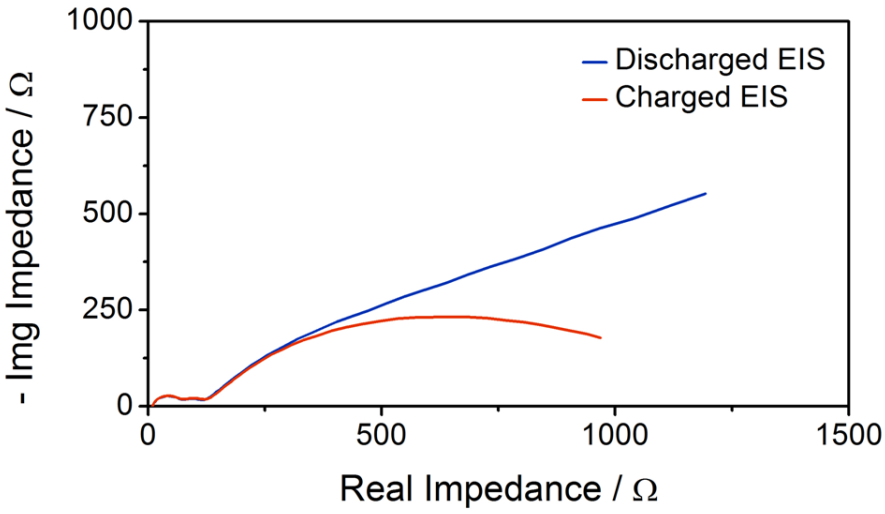

Figure 7.9 Electrochemical Impedance Spectroscopy of 80 °C cycled cell at the charged and discharged state. At the discharged state, only two semicircles are seem with a tail at approximately 45 degrees correlating to impedance from diffusion of lithium ions. At the charged state, three semicircles are seen. The third semicircle is attributed to the charge transfer resistance at the disordered LCO layer and ordered LCO layer interface as the lithium intercalation reaction in LCO is only active above 3.9 V

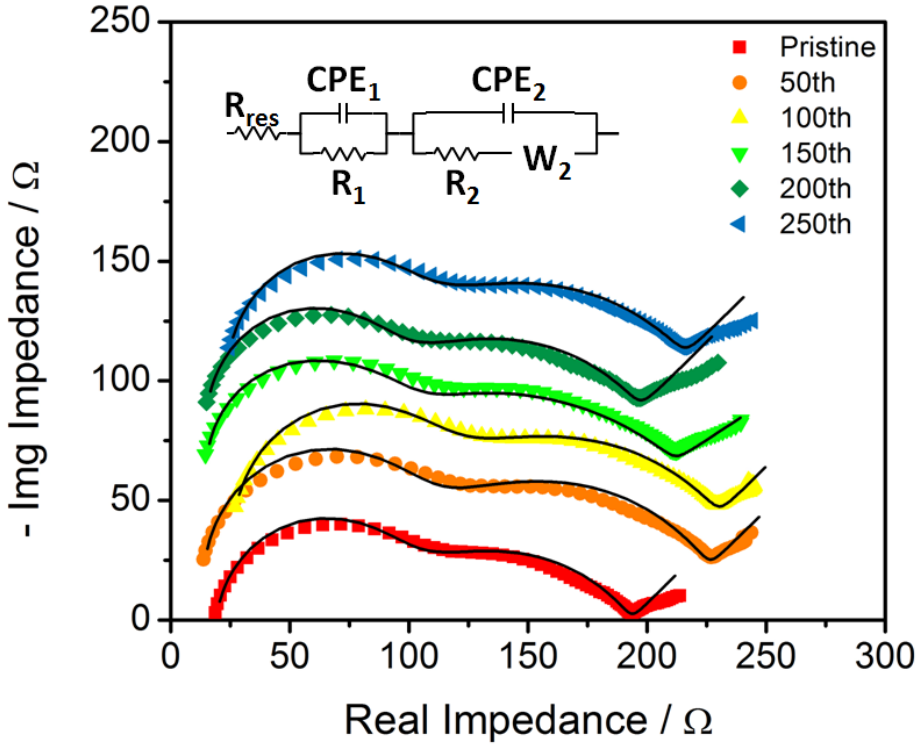

Figure 7.10 Electrochemical Impedance Spectroscopy of 25 °C cycled cell at the charged over 250 cycles. As the disordered LCO layer remains mostly unchanged, the impedance spectra of this cell also remain mostly unchanged. The detailed fitting parameters are shown in Table 7.2.

Table 7.2 Equivalent circuit parameters of the 25 °C cycled all-solid-state battery at the charged state determined from non-linear least squares fitting of the impedance spectra.

			CPE_1			CPE_2		
	R_{cell} Ω	**R_1 Ω**	C $nFs^{\eta-1}$	η	**R_2 Ω**	C $\mu Fs^{\eta-1}$	η	**W_2 $\Omega s^{-1/2}$**
Pristine	18	**68**	28.02	1	**107**	34.28	0.59	**4.54**
50th	14	**81**	26.75	1	**131**	29.21	0.61	**5.27**
100th	26	**72**	28.40	1	**132**	42.42	0.56	**4.90**
150th	14	**74**	27.50	1	**123**	36.05	0.59	**6.95**
200th	15	**69**	28.16	1	**113**	41.16	0.59	**7.61**
250th	23	**67**	28.68	1	**126**	46.89	0.55	**6.22**

7.4 Conclusion

We used STEM-EELS and EIS to elucidate capacity decay mechanisms of commercial all-solid-state thin-film batteries. By cycling these all-solid-state batteries at elevated temperatures, we were able to measure a significant increase in interfacial resistance due to the growth of a disordered interphase layer, which grew from ~300 nm in the pristine state to over four microns after cycling at 80 ºC. High temperature causes the decomposition of LCO into disordered rocksalt like cobalt oxide, Li_2O and Li_2O_2 while electrochemical cycling enhances the rate of decomposition. During cycling, the disordered layer consumes electrochemically active cathode layer, reducing the overall capacity. Through the combination of STEM-EELS and EIS, we were able to gain critical information correlating bulk scale performance and nanoscale probing. The analytical information gathered will help improve future engineering of all-solid-state batteries to establish new design rules for solid-solid interfaces and improve the electrochemical performance and lifetime of such devices.

Chapter 7, in full, is a reprint of the material “Effects of Cathode Electrolyte Interfacial (CEI) Layer on Long Term Cycling of All-Solid-State Thin-Film Batteries” as it appears in Journal of Power Sources, Ziying Wang, Jungwoo Z. Lee, Huolin L. Xin, Lili Han, Nathanael Grillon, Delphine Guy-Bouyssou, Emilien Bouyssou, Marina Proust, Ying Shirley Meng, 2016, 324, 342-348. The dissertation author was a co-primary investigator and author of this paper. All the experiment and writing were conducted by the author except for STEM-EELS data collection.

Chapter 8. Future Work

8.1 Formulating Guiding Principles for Interfacial Stability

The primary goal of high-end characterization techniques on lithium ion battery materials has always been to apply the knowledge gain through these techniques in order to improve material synthesis and explore new regimes of material. We hope to use our *in situ* AEM methodology on additional interfaces between the novel cathodes and novel electrolytes that have been proposed in the previous section. As a preliminary study, we have looked at the Spinel-LNMO/LiPON interface and observe that there is no evidence of a disordered interfacial layer that forms (Figure 8.1). Such a new interface is drastically different from what we previous seen in [128]. This is particularly interesting as Li et al [129] has shown over ten thousand cycles using a LNMO/LiPON/Li cell chemistry. Henceforth, it is of great scientific curiosity to understand what causes and prevents the formation of the disordered layer and not just its effects. Some recent computational papers have shown that there is a certain chemical instability between layered cathode material and solid state electrolytes [130]. There is a thermodynamic driving force for decomposition when the materials are in contact with each other. However if we can understand why certain interfaces do not form decomposition interfaces, we can use the knowledge learned in order to form guiding principles of interfacial engineering that produce distinct electrode-electrolyte interfaces with an additional protection layer. Such knowledge would be greatly useful in designing the next generation of all-solid-state thin film batteries and electrode coatings design for bulk systems.

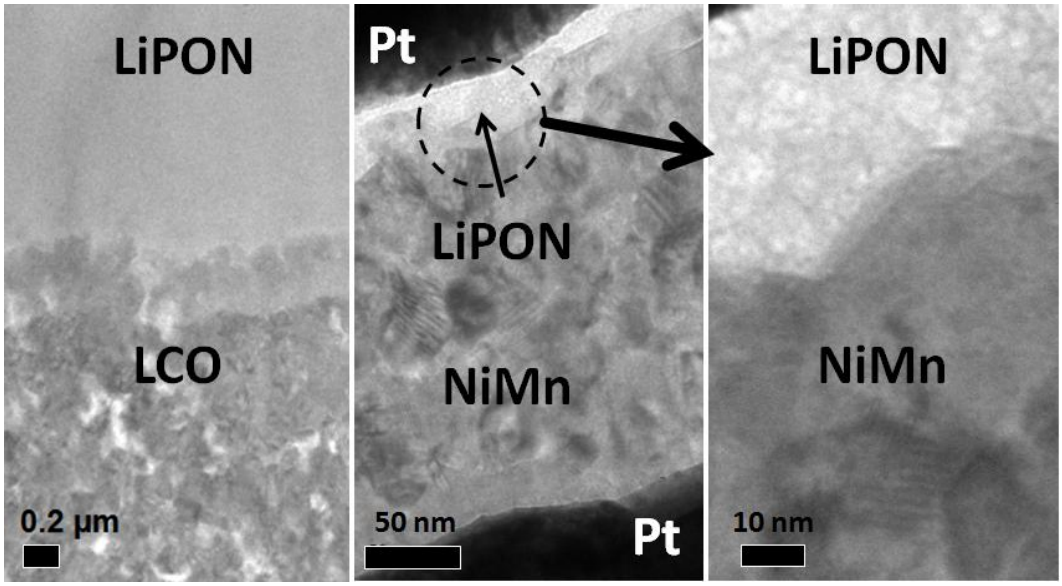

Figure 8.1 TEM image of the NiMn/LiPON interface showing no evidence of a disordered layer.

8.2 Elucidating the Role of Oxygen Activities

A novel oxygen vacancy assisted transition metal (TM) diffusion mechanism has been proposed by PI Meng's group to explain the near-surface phase transformation in lithium excess transition metal layered oxides (LENMO). Oxygen vacancies and TM migration have been observed at nm scale spatial resolution by STEM/EELS. Formation of (dilute) oxygen vacancies and their roles in assisting transition metal ion diffusion were revealed (Figure 8.2). The activation barriers of TM diffusion in the presence of oxygen vacancies are drastically reduced and consistently in a reasonable range for room temperature diffusion. One of the main questions we must answer is the role of oxygen activities at the interface and sub-surface between the bulk and the surface. Through *ex situ* STEM imaging, it has been shown that oxygen vacancy formation on the surface of lithium excess materials leads

to significant transition metal migration [110] and peroxo-like oxygen dimer formation within the bulk of the crystalline structure can contribute to charge provided by the overall redox reaction instead of mainly from transition metal oxidation [131]. Our plan to further elucidate the role of oxygen in structural changes involves the dynamic observation of STEM imaging of the crystal structure during cycling. Such capability can only be achieved when the electrochemical system is ultra-thin (~ 50 nm). We will discuss the methods by which we plan on tackling the technical challenges in a later section. Additionally, the electronic bonding changes that likely have occurred in O_2^{3-} oxidized from O_2^{4-} can be explored by O-K edge high loss EELS. Such experiments can definitively prove what types of oxygen (holes in O p-band, peroxo-like species, superoxo-like species or oxygen gas molecules) species are involved in the redox reactions of lithium ion battery materials. The data interpretations are likely to be complex and convoluted, for which we will also use first principles computation to assist the data analysis.

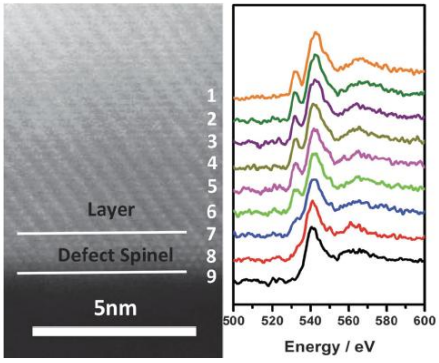

(a)

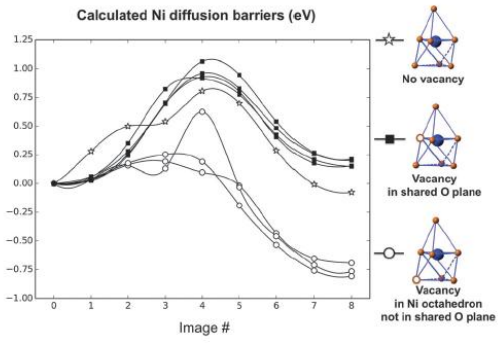

(b)

Figure 8.2 (a) Spatially resolved O K-edge EELS spectra from the bulk to the surface. (b) Calculated Ni diffusion barriers with oxygen vacancies in different positions at $Li_{20/28}Ni_{1/4}Mn_{7/12}O_2$ (vacancies in the tetrahedron but not in the shared plane are unstable)

8.3 Improving Temporal Resolution

So far the temporal resolution of our experiments has been limited by the scan time of the EELS mapping. It takes a significant amount of time to scan an area of 1 µm x 5 µm even with a pixel dwell time of 0.1 seconds due to small pixel size required for high spatial resolution. To resolve this issue, we further propose the employment of energy-filtered TEM (EFTEM) to observe the time-resolved distribution of lithium during charging and discharging. EFTEM combines the elemental specificity of EELS with the speed of conventional TEM image acquisition to achieve this goal. EFTEM has been applied to directly observe lithium distribution in past studies [132]. However, our unique *in situ* experimental setup coupled with our group's expertise in high resolution imaging of battery materials will allow us to enable lithium mapping during cycling with high temporal resolution. At UCSD, we have access to an FEI Tecnai G2 Polara 300KV electron microscope equipped with a field emission gun (FEG). It is equipped with a Gatan Quantum energy filter for zero-loss imaging and elemental mapping and EELS studies along with a Gatan K2 direct detector system, providing 4k x 4k imaging at 400 fps temporal resolution. We currently have an electrical bias-capable TEM holder at UCSD (Figure 8.3) manufactured by NanoFactory that can be used to conduct spectroscopy studies with the K2 detector. This holder can be used in conjunction with the aforementioned TEM's at UCSD.

Figure 8.3 *In situ* TEM holder by Nanofactory capable of electrical bias

8.4 Improving Spatial Resolution

High spatial resolution is the crux of transmission electron microscopy. Many aspects of the proposed study of interface dynamics depend on the ability to resolve atomic-scale characteristics and changes. These include, but are not limited to, application of annular bright and dark field STEM modes to enable direct observation of defect evolution such as oxygen vacancy formation [133] or local structural disorder [134] in cathode materials at the solid-solid interfaces. Up to this point, spatial resolution of our *in situ* method has been limited by the practicality of thinning nanobatteries beyond a critical thickness. Atomic-scale high-resolution imaging requires a sample below 50 nm in thickness. Yet reducing a nanobattery to this thickness will cause damage to the sample due to its remarkably small volume, unless the applied current can be reduced as well. A solution to the spatial resolution requires overcoming two obstacles: (1) reducing the magnitude of the current source to the

femtoAmpere (fA) scale and (2) shielding the sample (and hence the minute current) from stray fields within the TEM, and (3) the application of these features to a holder with double-tilt capabilities.

The fA-scale currents required will be achieved with the use of our current potentiostat, a Biologic SP-200. This equipment is rated with <0.1 fA noise resolution, which is suitable for the desired 10-100 fA current range. More importantly however, the ultra-low current required to cycle an appropriately thin nanobattery will be susceptible to stray fields generated by the electronics within the TEM and surrounding equipment. A common solution to mitigate noise from nearby equipment is the application of a Faraday cage, which effectively shields a region of space from those stray fields. Design of the Faraday cage only requires wire cage spacing smaller than the wavelength of the electromagnetic radiation to be blocked. It may appear counterintuitive to shield a sample from electric fields when the probe itself is an electron beam. However, a merit of the TEM is the high frequency of the electrons themselves, where $\lambda_{electron}$ (E=200 keV) = 0.0027 nm. As such, electrons will be largely unaffected by the shielding. Further, Faraday cages do not impact magnetic fields, and will not impact the microscope's ability to manipulate the electrons. Finally, in order to maximize the ability to achieve atomic-scale resolution, these features need to be applied to a sample holder with double-tilt capabilities. A prototype design of such a TEM holder is shown in Figure 8.4**.** We will work with the current sample holder (Hummingbird) supplier and Biologic to enable such low current option.

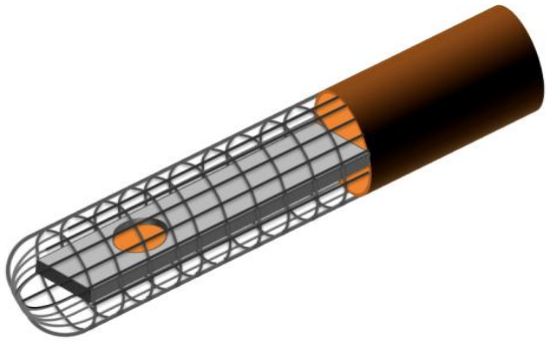

Figure 8.4 Prototype design of a proposed TEM holder with a Faraday Cage. The Faraday Cage screens out electric field interference that would impact femtoampere current measurement.

References

1. NASA. *Climate Change: Vital Signs of the Planet: Global Temperature*. 2016; Available from: http://climate.nasa.gov/vital-signs/global-temperature/.

2. NOAA. *NOAA Paleoclimatology Global Warming - The Data*. 2016; Available from: https://www.ncdc.noaa.gov/paleo/globalwarming/temperature-change.html.

3. NASA. *Climate Change: Vital Signs of the Planet: Carbon Dioxide*. 2016; Available from: http://climate.nasa.gov/vital-signs/carbon-dioxide/.

4. EPA. *Global Greenhouse Gas Emissions Data*. 2016; Available from: https://www3.epa.gov/climatechange/ghgemissions/global.html.

5. Bates, J.B., N.J. Dudney, G.R. Gruzalski, R.A. Zuhr, A. Choudhury, C.F. Luck, and J.D. Robertson, *Electrical properties of amorphous lithium electrolyte thin films.* Solid State Ionics, 1992. **53**: p. 647-654.

6. Wang, B., J.B. Bates, F.X. Hart, B.C. Sales, R.A. Zuhr, and J.D. Robertson, *Characterization of Thin-Film Rechargeable Lithium Batteries with Lithium Cobalt Oxide Cathodes.* Journal of The Electrochemical Society, 1996. **143**(10): p. 3203-3213.

7. Yu, X., J.B. Bates, G.E.J. Jellison, and F.X. Hart, *A Stable Thin-Film Lithium Electrolyte: Lithium Phosphorous Oxynitride.* J. Electrochem. Soc., 1997. **144**: p. 524-532.

8. Schwöbel, A., R. Hausbrand, and W. Jaegermann, *Interface reactions between LiPON and lithium studied by in-situ X-ray photoemission.* Solid State Ionics, 2015. **273**: p. 51-54.

9. Zhu, Y., X. He, and Y. Mo, *Origin of Outstanding Stability in the Lithium Solid Electrolyte Materials: Insights from Thermodynamic Analyses Based on First-Principles Calculations.* ACS Applied Materials & Interfaces, 2015. **7**(42): p. 23685-23693.

10. Zhu, Y., X. He, and Y. Mo, *First principles study on electrochemical and chemical stability of solid electrolyte-electrode interfaces in all-solid-state Li-ion batteries.* Journal of Materials Chemistry A, 2016. **4**(9): p. 3253-3266.

11. Mizushima, K., P.C. Jones, P.J. Wiseman, and J.B. Goodenough, *LixCoO2 (0<x<-1): A new cathode material for batteries of high energy density.* Materials Research Bulletin, 1980. **15**(6): p. 783-789.

12. Reimers, J.N. and J.R. Dahn, *Electrochemical and In Situ X-Ray Diffraction Studies of Lithium Intercalation in Li x CoO2.* Journal of The Electrochemical Society, 1992. **139**(8): p. 2091-2097.

13. Ohzuku, T. and A. Ueda, *Solid-State Redox Reactions of LiCoO2 ($R\bar{3}m$) for 4 Volt Secondary Lithium Cells.* Journal of The Electrochemical Society, 1994. **141**(11): p. 2972-2977.

14. Kasavajjula, U., C. Wang, and A.J. Appleby, *Nano- and bulk-silicon-based insertion anodes for lithium-ion secondary cells.* Journal of Power Sources, 2007. **163**(2): p. 1003-1039.

15. McDowell, M.T., S.W. Lee, W.D. Nix, and Y. Cui, *25th Anniversary Article: Understanding the Lithiation of Silicon and Other Alloying Anodes for Lithium-Ion Batteries.* Advanced Materials, 2013. **25**(36): p. 4966-4985.

16. Obrovac, M.N. and L. Christensen, *Structural Changes in Silicon Anodes during Lithium Insertion/Extraction.* Electrochemical and Solid-State Letters, 2004. **7**(5): p. A93-A96.

17. Takamura, T., S. Ohara, M. Uehara, J. Suzuki, and K. Sekine, *A vacuum deposited Si film having a Li extraction capacity over 2000 mAh/g with a long cycle life.* Journal of Power Sources, 2004. **129**(1): p. 96-100.

18. Li, J., A.K. Dozier, Y. Li, F. Yang, and Y.-T. Cheng, *Crack Pattern Formation in Thin Film Lithium-Ion Battery Electrodes.* Journal of The Electrochemical Society, 2011. **158**(6): p. A689-A694.

19. Bates, J.B., G.R. Gruzalski, N.J. Dudney, C.F. Luck, and X. Yu, *Rechargeable thin-film lithium batteries.* Solid State Ionics, 1994. **70**: p. 619-628.

20. Bates, J.B., N.J. Dudney, D.C. Lubben, G.R. Gruzalski, B.S. Kwak, X. Yu, and R.A. Zuhr, *Thin-film rechargeable lithium batteries.* Journal of Power Sources, 1995. **54**(1): p. 58-62.

21. Volkert, C.A. and A.M. Minor, *Focused Ion Beam Microscopy and Micromachining.* MRS Bulletin, 2007. **32**(05): p. 389-399.

22. Nathan, C.L., N. Prashant, M.M. Kevin, J.N. David, and O. Sang-Hyun, *Engineering metallic nanostructures for plasmonics and nanophotonics.* Reports on Progress in Physics, 2012. **75**(3): p. 036501.

23. Naik, J.P., *NANOWIRES FABRICATED BY FOCUSED ION BEAM*, in *Mechanical Engineering*. 2013, The University of Birmingham.

24. Utke, I., P. Hoffmann, and J. Melngailis, *Gas-assisted focused electron beam and ion beam processing and fabrication.* Journal of Vacuum Science & Technology B, 2008. **26**(4): p. 1197-1276.

25. Casey, J.D., A.F. Doyle, R.G. Lee, D.K. Stewart, and H. Zimmermann, *Gas-assisted etching with focused ion beam technology.* Microelectronic Engineering, 1994. **24**(1): p. 43-50.

26. Young, R.J., J.R.A. Cleaver, and H. Ahmed, *Characteristics of gas-assisted focused ion beam etching.* Journal of Vacuum Science & Technology B, 1993. **11**(2): p. 234-241.

27. Wikipedia. *Focused Ion Beam*.

28. Sparrow, T.G., B.G. Williams, C.N.R. Rao, and J.M. Thomas, *L3/L2 white-line intensity ratios in the electron energy-loss spectra of 3d transition-metal oxides.* Chemical Physics Letters, 1984. **108**(6): p. 547-550.

29. Thole, B.T. and G. van der Laan, *Branching ratio in x-ray absorption spectroscopy.* Physical Review B, 1988. **38**(5): p. 3158-3171.

30. de Groot, F.M.F., J.C. Fuggle, B.T. Thole, and G.A. Sawatzky, *2p X-ray absorption of 3d transition-metal compounds: An atomic multiplet description including the crystal field.* Physical Review B, 1990. **42**(9): p. 5459-5468.

31. Morrison, T.I., M.B. Brodsky, N.J. Zaluzec, and L.R. Sill, *Iron d -band occupancy in amorphous Fe_xGe_x-1.* Physical Review B, 1985. **32**(5): p. 3107-3111.

32. Pearson, D.H., B. Fultz, and C.C. Ahn, *Measurements of 3d state occupancy in transition metals using electron energy loss spectrometry.* Applied Physics Letters, 1988. **53**(15): p. 1405-1407.

33. Pearson, D.H., C.C. Ahn, and B. Fultz, *White lines and d -electron occupancies for the 3d and 4d transition metals.* Physical Review B, 1993. **47**(14): p. 8471-8478.

34. Riedl, T., T. Gemming, and K. Wetzig, *Extraction of EELS white-line intensities of manganese compounds: Methods, accuracy, and valence sensitivity.* Ultramicroscopy, 2006. **106**(4–5): p. 284-291.

35. Kurata, H. and C. Colliex, *Electron-energy-loss core-edge structures in manganese oxides.* Physical Review B, 1993. **48**(4): p. 2102-2108.

36. Mansot, J.L., P. Leone, P. Euzen, and P. Palvadeau, *Valence of manganese, in a new oxybromide compound, determined by means of electron energy loss spectroscopy.* Microsc. Microanal. Microstruct., 1994. **5**(2): p. 79-90.

37. Wang, Z.L., J.S. Yin, and Y.D. Jiang, *EELS analysis of cation valence states and oxygen vacancies in magnetic oxides.* Micron, 2000. **31**(5): p. 571-580.

38. Liu, X.H., H. Zheng, L. Zhong, S. Huang, K. Karki, L.Q. Zhang, Y. Liu, A. Kushima, W.T. Liang, J.W. Wang, J.H. Cho, E. Epstein, S.A. Dayeh, S.T. Picraux, T. Zhu, J. Li, J.P. Sullivan, J. Cumings, C. Wang, S.X. Mao, Z.Z. Ye, S. Zhang, and J.Y. Huang, *Anisotropic Swelling and Fracture of Silicon Nanowires During Lithiation.* Nano Lett., 2011. **11**: p. 3312-3318.

39. Wang, F., H.-C. Yu, M.-H. Chen, L. Wu, N. Pereira, K. Thornton, A.V.d. Ven, Y. Zhu, G.G. Amatucci, and J. Graetz, *Tracking lithium transport and electrochemical reactions in nanoparticles.* Nature Communications, 2012. **3**: p. 1201.

40. Liu, X.H., S. Huang, S.T. Picraux, J. Li, T. Zhu, and J.Y. Huang, *Reversible Nanopore Formation in Ge Nanowires during Lithiation–Delithiation Cycling: An In Situ Transmission Electron Microscopy Study.* Nano Letters, 2011. **11**(9): p. 3991-3997.

41. Zhang, L.Q., X.H. Liu, Y. Liu, S. Huang, T. Zhu, L. Gui, S.X. Mao, Z.Z. Ye, C.M. Wang, J.P. Sullivan, and J.Y. Huang, *Controlling the Lithiation-Induced Strain and Charging Rate in Nanowire Electrodes by Coating.* ACS Nano, 2011. **6**: p. 4800-4809.

42. Yamamoto, K., Y. Iriyama, T. Asaka, T. Hirayama, H. Fujita, C.A.J. Fisher, K. Nonaka, Y. Sugita, and Z. Ogumi, *Dynamic Visualization of the Electric Potential in an All-Solid-State Rechargeable Lithium Battery.* Angew. Chem. Int. Ed., 2010. **49**: p. 4414-4417.

43. Liu, X.H., L.Q. Zhang, L. Zhong, Y. Liu, H. Zheng, J.W. Wang, J.-H. Cho, S.A. Dayeh, S.T. Picraux, J.P. Sullivan, S.X. Mao, Z.Z. Ye, and J.Y. Huang, *Ultrafast Electrochemical Lithiation of Individual Si Nanowire Anodes.* Nano Lett., 2011. **11**: p. 2251-2258.

44. Huang, J.Y., L. Zhong, C.M. Wang, J.P. Sullivan, W. Xu, L.Q. Zhang, S.X. Mao, N.S. Hudak, X.H. Liu, A. Subramanian, H. Fan, L. Qi, A. Kushima, and J. Li, *In Situ Observation of the Electrochemical Lithiation of a Single SnO2 Nanowire Electrode.* Science, 2010. **330**(6010): p. 1515-1520.

45. Wang, C.M., W. Xu, J. Liu, J.G. Zhang, L.V. Saraf, B.W. Arey, D. Choi, Z.G. Yang, J. Xiao, S. Thevuthasan, and D.R. Baer, *In situ Trasnsmission Electron Microscopy Observation of Microstructural and Phase Evolution in a SnO2 Nanowire during Lithium Intercalation.* Nano Lett., 2011. **11**: p. 1874-1880.

46. Giannuzi, L.A. and F.A. Stevie, *Introduction to Focused Ion Beams: Instrumentation, Theory, Techniques and Practice*. 2005: Springer: New York.

47. Mayer, J., L.A. Giannuzi, T. Kamino, and J. Michael, *TEM Sample Preparation and FIB-induced Damage.* MRS Bulletin, 2007. **32**: p. 400-407.

48. Lugstein, A., B. Basnar, and E. Bertagnolli, *Study of focused ion beam response of GaAs in the nanoscale regime.* J. Vac. Sci. Technol. B., 2002. **20**: p. 2238 – 2242.

49. Rubanov, S. and P.R. Munroe, *Investigation of the structure of damage layers in TEM samples prepared using a focused ion beam.* J. Mater. Sci. Lett., 2001. **20**: p. 1181-1183.

50. Kato, N.I., *Reducing focused ion beam damage to transmission electron microscopy samples.* J. Elect. Micro., 2004. **53**: p. 451 – 458.

51. Bals, S., W. Tirry, R. Geurts, Z. Yang, and D. Schryvers, *High quality sample preparation by low kV FIB thinning for analytical TEM measurements.* Microsc. Microanal., 2007. **13**: p. 80 – 86.

52. Miyajima, N., C. Holzapfel, Y. Asahara, L. Dubrovinsky, K. Niwa, M. Ichihara, and T. Yagi, *Combining FIB milling and conventional argon ion milling techniques to prepare high-quality site-specific TEM samples for quantitative EELS analysis of oxygen in molten iron.* J. Elect. Microsc., 2010. **238**: p. 200 – 209.

53. Scahaffer, M., B. Schaffer, and Q. Ramasse, *Sample preparation for atomic-resolution STEM at low voltages by FIB.* Ultramicroscopy, 2012. **114**: p. 62 – 71.

54. Santhanagopalan, D., D. Qian, T. McGilvray, Z. Wang, F. Wang, F. Camino, J. Graetz, N. Dudney, and Y.S. Meng, *Interface Limited Lithium Transport in Solid-State Batteries.* The Journal of Physical Chemistry Letters, 2013: p. 298-303.

55. Balke, N., S. Jesse, Y. Kim, L. Adamccky, A. Tselev, I.N. Ivanov, N.J. Dudney, and S.V. Kalinin, *Real space mapping of Li-ion transport in amorphous Si anodes with nanometer resolution.* Nano Lett., 2010. **10**: p. 3420 – 3425.

56. Egerton, R.F., P. Li, and M. Malac, *Radiation damage in the TEM and SEM.* Micron, 2004. **35**: p. 399 – 409.

57. Buban, J.P., Q. Ramasse, B. Gipson, N.D. Browning, and H. Stahlberg, *High-resolution low-dose scanning transmission electron microscopy.* J. Elect. Microsc., 2010. **59**: p. 103 – 112.

58. Rightor, E.G., A.P. Hitchcock, H. Ade, R.D. Leapman, S.G. Urquhart, A.P. Smith, G. Mitchell, D. Fischer, H.J. Shin, and T. Warwick, *Spectromicroscopy*

of poly(ethylene terephthalate): comparison of spectra and radiation damage rates in X-ray absorption and electron energy loss. J. Phys. Chem. B., 1997. **101**: p. 1950 – 1960.

59. Jiang, N. and J.C.H. Spence, *On the dose-rate threshold of beam damage in TEM.* Ultramicroscopy, 2012. **113**: p. 77 – 82.

60. Li, P. and R.F. Egerton, *Radiation damage in Coronene, rubrene and p-terphenyl, measured for incident electrons of kinetic energy between 100 and 200 keV.* Ultramicroscopy, 2004. **101**: p. 161 – 172.

61. Bates, J.B., N.J. Dudney, G.R. Gruzalski, R.A. Zuhir, A. Choudhury, C.F. Luck, and J.D. Robertson, *Electrical properties of amorphous lithium electrolyte thin films.* Sol. Stat. Ionics., 1992. **53 – 56**: p. 647 – 654.

62. Yu, X., J.B. Bates, G.E.J. Jellison, and F.X. Hart, *A stable thin-film lithium electrolyte: Lithium pospohorous oxynitride.* J. Electrochem. Soc., 1997. **144**: p. 524 – 532.

63. Yu, X., J.B. Bates, and G.E.J. Jellison, *Characterization of lithium phosphorous oxynitride thin films*, in *188th Meeting of the Electrochemical Society*, J.B. Bates, Editor. 1996, Electrochemical Society, Pennington, New Jersey: Chicago, Illinois. p. 23 – 30.

64. Egerton, R.F., *Mechanism of radiation damage in beam-sensitive specimens, for TEM accelerating voltages between 10 and 300 kV.* Microsc. Res. Techniq., 2012. **75**: p. 1550 – 1556.

65. Ohata, N., K. Takada, L. Zhang, R. Ma, M. Osada, and T. Sasaki, *Enhancement of the High-Rate Capability of Solid-State Lithium Batteries by Nanoscale Interfacial Modification.* Adv. Mater., 2006. **18**: p. 2226-2229.

66. Brazier, A., L. Dupont, L. Dantras-Laffont, N. Kuwata, J. Kawamura, and J.M. Tarascon, *First Cross-Section Observation of an All Solid-State Lithium-Ion "Nanobattery" by Transmission Electron Microscopy.* Chem. Mater., 2008. **20**(6): p. 2352-2359.

67. Yu, X., Q. Wang, Y. Zhou, H. Li, X.-Q. Yang, K.-W. Nam, S.N. Ehrlich, S. Khalid, and Y.S. Meng, *High Rate Delithiation Behaviour of LiFePO4 Studied by Quick X-Ray Absorption Spectroscopy.* Chem. Commun., 2012. **48**: p. 11537-11539.

68. Liu, X.H., S. HUang, S.T. Picraux, J. Li, T. Zhu, and J.Y. Huang, *Reversible Nanopore Formation in Ge Nanowires during Lithiation-Delithiation Cycling: An In situ Transmission Electron Microscopy Study.* Nano Lett., 2011. **11**: p. 3991-3997.

69. Leung, K., *Electronic Structure Modeling of Electrochemical Reactions at Electrode/Electrolyte Interfaces in Lithium Ion Batteries.* J. Phys. Chem. C, 2013. **117**: p. 1539-1547.

70. Jorn, R., R. Kumar, D.P. Abraham, and G.A. Voth, *Atomistic Modeling of the Electrode-Electrolyte Interface in Li-Ion Energy Storage Systems: Electrolyte Structuring.* J. Phys. Chem. C, 2013. **117**: p. 3747-3761.

71. Fister, T.T., B.R. Long, A.A. Gewirth, B. Shi, L. Assoufid, S.S. Lee, and P. Fenter, *Real-Time Observations of Interfacial Lithiation in a Metal Silicide Thin Film.* J. Phys. Chem. C, 2012. **116**: p. 22341-22345.

72. Carroll, K.J., D. Qian, C. Fell, S. Calvin, G.M. Veith, M. Chi, L. Baggetto, and Y.S. Meng, *Probing the Electrode/Electrolyte Interface in the Lithium Excess Layered Oxide Li1.2Ni0.2Mn0.6O2.* Phys. Chem. Chem. Phys., 2013. **15**: p. 11128-11138.

73. Ruzmetov, D., V.P. Oleshko, P.M. Haney, H.J. Lezec, K. Karki, K.H. Baloch, A.K. Agarwal, A.V. Davydov, S. Krylyuk, Y. Liu, J.Y. Huang, M. Tanase, J. Cumings, and A.A. Talin, *Electrolyte Stability Determines Scaling Limits for Solid-State 3D Li-ion Batteries.* Nano Lett., 2012. **12**: p. 505-511.

74. Wang, F., H.C. Yu, M.H. Chen, L. Wu, N. Pereira, K. Thornton, A.V.D. Ven, Y.R. Zhu, G.G. Amatucci, and J. Graetz, *Tracking Lithium Transport and Electrochemical Reactions in Nanoparticles.* Nat. Commun., 2012. **3**: p. 1201-1208.

75. Jang, Y.-I., N.J. Dudney, D.A. Blom, and L.F. Allard, *High-Voltage Cycling Behavior of Thin-Film LiCoO2 Cathodes.* J. Electrochem. Soc., 2002. **149**: p. A1442-A1447.

76. Wang, J.W., Y. He, F. Fan, X.H. Liu, S. Xia, Y. Liu, C.T. Harris, H. Li, J.Y. Huang, S.X. Mao, and T. Zhu, *Two-Phase Electrochemical Lithiation in Amorphous Silicon.* Nano Lett., 2013. **13**: p. 709-715.

77. McDowell, M.T., S.W. Lee, J.T. Harris, B.A. Korgel, C. Wang, W.D. Nix, and Y. Cui, *In Situ TEM of Two-Phase Lithiation of Amorphous Silicon Nanospheres.* Nano Lett., 2013. **13**: p. 758-764.

78. Maranchi, J.P., A.F. Hepp, A.G. Evans, N.T. Nuhfer, and P.N. Kumta, *Interfacial Properties of the a-Si/Cu: Active-Inactive Thin-Film Anode System for Lithium-Ion Batteries.* J. Electrochem. Soc., 2006. **153**: p. A1246-A1253.

79. Neudecker, B.J., N.J. Dudney, and J.B. Bates, *"Lithium-Free" Thin-Film Battery with In Situ Plated Li Anode.* J. Electrochem. Soc., 2000. **147**: p. 517-523.

80. McDowell, M.T., I. Ryu, S.W. Lee, C. Wang, W.D. Nix, and Y. Cui, *Studying the Kinetics of Crystalline Silicon Nanoparticle Lithiation with In Situ Transmission Electron Microscopy.* Adv. Mater., 2012. **24**: p. 6034-6041.

81. Luntz, A.C., J. Voss, and K. Reuter, *Interfacial Challenges in Solid-State Li Ion Batteries.* The Journal of Physical Chemistry Letters, 2015. **6**(22): p. 4599-4604.

82. Kamaya, N., K. Homma, Y. Yamakawa, M. Hirayama, R. Kanno, M. Yonemura, T. Kamiyama, Y. Kato, S. Hama, K. Kawamoto, and A. Mitsui, *A lithium superionic conductor.* Nat Mater, 2011. **10**(9): p. 682-686.

83. Inaguma, Y., C. Liquan, M. Itoh, T. Nakamura, T. Uchida, H. Ikuta, and M. Wakihara, *High ionic conductivity in lithium lanthanum titanate.* Solid State Communications, 1993. **86**(10): p. 689-693.

84. Kanno, R. and M. Murayama *Lithium Ionic Conductor Thio-LISICON: The Li2 S - GeS2 - P 2 S 5 System.* Journal of The Electrochemical Society, 2001. **148**(7): p. A742-A746.

85. Murugan, R., V. Thangadurai, and W. Weppner, *Fast Lithium Ion Conduction in Garnet-Type Li7La3Zr2O12.* Angewandte Chemie International Edition, 2007. **46**(41): p. 7778-7781.

86. Kotobuki, M., H. Munakata, K. Kanamura, Y. Sato, and T. Yoshida, *Compatibility of Li7La3Zr2O12 Solid Electrolyte to All-Solid-State Battery Using Li Metal Anode.* Journal of The Electrochemical Society, 2010. **157**(10): p. A1076-A1079.

87. Sakuda, A., A. Hayashi, and M. Tatsumisago, *Interfacial Observation between LiCoO2 Electrode and Li2S−P2S5 Solid Electrolytes of All-Solid-State Lithium Secondary Batteries Using Transmission Electron Microscopy.* Chemistry of Materials, 2010. **22**(3): p. 949-956.

88. Ohta, N., K. Takada, L. Zhang, R. Ma, M. Osada, and T. Sasaki, *Enhancement of the High-Rate Capability of Solid-State Lithium Batteries by Nanoscale Interfacial Modification.* Advanced Materials, 2006. **18**(17): p. 2226-2229.

89. Iriyama, Y., T. Kako, C. Yada, T. Abe, and Z. Ogumi, *Reduction of charge transfer resistance at the lithium phosphorus oxynitride/lithium cobalt oxide interface by thermal treatment.* Journal of Power Sources, 2005. **146**(1–2): p. 745-748.

90. Iriyama, Y., T. Kako, C. Yada, T. Abe, and Z. Ogumi, *Charge transfer reaction at the lithium phosphorus oxynitride glass electrolyte/lithium cobalt oxide thin film interface.* Solid State Ionics, 2005. **176**(31–34): p. 2371-2376.

91. Yada, C., A. Ohmori, K. Ide, H. Yamasaki, T. Kato, T. Saito, F. Sagane, and Y. Iriyama, *Dielectric Modification of 5V-Class Cathodes for High-Voltage All-Solid-State Lithium Batteries.* Advanced Energy Materials, 2014. **4**(9): p. n/a-n/a.

92. Richards, W.D., L.J. Miara, Y. Wang, J.C. Kim, and G. Ceder, *Interface Stability in Solid-State Batteries.* Chemistry of Materials, 2016. **28**(1): p. 266-273.

93. Miara, L.J., W.D. Richards, Y.E. Wang, and G. Ceder, *First-Principles Studies on Cation Dopants and Electrolyte|Cathode Interphases for Lithium Garnets.* Chemistry of Materials, 2015. **27**(11): p. 4040-4047.

94. Brazier, A., L. Dupont, L. Dantras-Laffont, N. Kuwata, J. Kawamura, and J.M. Tarascon, *First Cross-Section Observation of an All Solid-State Lithium-Ion "Nanobattery" by Transmission Electron Microscopy.* Chemistry of Materials, 2008. **20**(6): p. 2352-2359.

95. Liu, X.H., J.W. Wang, S. Huang, F. Fan, X. Huang, Y. Liu, S. Krylyuk, J. Yoo, S.A. Dayeh, A.V. Davydov, S.X. Mao, S.T. Picraux, S. Zhang, J. Li, T. Zhu, and J.Y. Huang, *In situ atomic-scale imaging of electrochemical lithiation in silicon.* Nat Nano, 2012. **7**(11): p. 749-756.

96. Zhu, Y., J.W. Wang, Y. Liu, X. Liu, A. Kushima, Y. Liu, Y. Xu, S.X. Mao, J. Li, C. Wang, and J.Y. Huang, *In Situ Atomic-Scale Imaging of Phase Boundary Migration in FePO4 Microparticles During Electrochemical Lithiation.* Advanced Materials, 2013. **25**(38): p. 5461-5466.

97. Gu, M., L.R. Parent, B.L. Mehdi, R.R. Unocic, M.T. McDowell, R.L. Sacci, W. Xu, J.G. Connell, P. Xu, P. Abellan, X. Chen, Y. Zhang, D.E. Perea, J.E. Evans, L.J. Lauhon, J.-G. Zhang, J. Liu, N.D. Browning, Y. Cui, I. Arslan, and C.-M. Wang, *Demonstration of an Electrochemical Liquid Cell for Operando Transmission Electron Microscopy Observation of the Lithiation/Delithiation Behavior of Si Nanowire Battery Anodes.* Nano Letters, 2013. **13**(12): p. 6106-6112.

98. Mehdi, B.L., J. Qian, E. Nasybulin, C. Park, D.A. Welch, R. Faller, H. Mehta, W.A. Henderson, W. Xu, C.M. Wang, J.E. Evans, J. Liu, J.G. Zhang, K.T. Mueller, and N.D. Browning, *Observation and Quantification of Nanoscale Processes in Lithium Batteries by Operando Electrochemical (S)TEM.* Nano Letters, 2015. **15**(3): p. 2168-2173.

99. Holtz, M.E., Y. Yu, D. Gunceler, J. Gao, R. Sundararaman, K.A. Schwarz, T.A. Arias, H.D. Abruña, and D.A. Muller, *Nanoscale Imaging of Lithium Ion Distribution During In Situ Operation of Battery Electrode and Electrolyte.* Nano Letters, 2014. **14**(3): p. 1453-1459.

100. Santhanagopalan, D., D. Qian, T. McGilvray, Z. Wang, F. Wang, F. Camino, J. Graetz, N. Dudney, and Y.S. Meng, *Interface Limited Lithium Transport in Solid-State Batteries.* The Journal of Physical Chemistry Letters, 2013. **5**(2): p. 298-303.

101. Ziying, W. and M. Ying Shirley, *Analytical Electron Microscopy Study of All Solid-State Batteries*, in *Handbook of Solid State Batteries*. 2015, WORLD SCIENTIFIC. p. 109-131.

102. Lee, J., A. Urban, X. Li, D. Su, G. Hautier, and G. Ceder, *Unlocking the Potential of Cation-Disordered Oxides for Rechargeable Lithium Batteries.* Science, 2014. **343**(6170): p. 519-522.

103. Wang, F., J. Graetz, M.S. Moreno, C. Ma, L. Wu, V. Volkov, and Y. Zhu, *Chemical Distribution and Bonding of Lithium in Intercalated Graphite: Identification with Optimized Electron Energy Loss Spectroscopy.* ACS Nano, 2011. **5**(2): p. 1190-1197.

104. Fano, U., *Effects of Configuration Interaction on Intensities and Phase Shifts.* Physical Review, 1961. **124**(6): p. 1866-1878.

105. Graetz, J., A. Hightower, C.C. Ahn, R. Yazami, P. Rez, and B. Fultz, *Electronic Structure of Chemically-Delithiated LiCoO2 Studied by Electron Energy-Loss Spectrometry.* The Journal of Physical Chemistry B, 2002. **106**(6): p. 1286-1289.

106. Stemmer, S., A. Sane, N.D. Browning, and T.J. Mazanec, *Characterization of oxygen-deficient SrCoO3−δ by electron energy-loss spectroscopy and Z-contrast imaging.* Solid State Ionics, 2000. **130**(1–2): p. 71-80.

107. Aydinol, M.K., A.F. Kohan, G. Ceder, K. Cho, and J. Joannopoulos, *Ab initio study of lithium intercalation in metal oxides and metal dichalcogenides.* Physical Review B, 1997. **56**(3): p. 1354-1365.

108. Ceder, G., A.V.d. Ven, C. Marianetti, and D. Morgan, *First-principles alloy theory in oxides.* Modelling and Simulation in Materials Science and Engineering, 2000. **8**(3): p. 311-321.

109. Carroll, K.J., D. Qian, C. Fell, S. Calvin, G.M. Veith, M. Chi, L. Baggetto, and Y.S. Meng, *Probing the electrode/electrolyte interface in the lithium excess layered oxide Li1.2Ni0.2Mn0.6O2.* Physical Chemistry Chemical Physics, 2013. **15**(26): p. 11128-11138.

110. Xu, B., C.R. Fell, M. Chi, and Y.S. Meng, *Identifying surface structural changes in layered Li-excess nickel manganese oxides in high voltage lithium*

ion batteries: A joint experimental and theoretical study. Energy & Environmental Science, 2011. **4**(6): p. 2223-2233.

111. Fell, C.R., D. Qian, K.J. Carroll, M. Chi, J.L. Jones, and Y.S. Meng, *Correlation Between Oxygen Vacancy, Microstrain, and Cation Distribution in Lithium-Excess Layered Oxides During the First Electrochemical Cycle.* Chemistry of Materials, 2013. **25**(9): p. 1621-1629.

112. Hwang, S., W. Chang, S.M. Kim, D. Su, D.H. Kim, J.Y. Lee, K.Y. Chung, and E.A. Stach, *Investigation of Changes in the Surface Structure of LixNi0.8Co0.15Al0.05O2 Cathode Materials Induced by the Initial Charge.* Chemistry of Materials, 2014. **26**(2): p. 1084-1092.

113. Graetz, J., *Electronic Environments and Electrochemical Properties of Lithium Storage Materials*, in *Engineering and Applied Science*. 2003, California Institute of Technology.

114. Moreno, M.S., K. Jorissen, and J.J. Rehr, *Practical aspects of electron energy-loss spectroscopy (EELS) calculations using FEFF8.* Micron, 2007. **38**(1): p. 1-11.

115. Qiao, R., Y.-D. Chuang, S. Yan, and W. Yang, *Soft X-Ray Irradiation Effects of Li2O2, Li2CO3 and Li2O Revealed by Absorption Spectroscopy.* PLoS ONE, 2012. **7**(11): p. e49182.

116. Amatucci, G.G., J.M. Tarascon, and L.C. Klein, *CoO2, The End Member of the Li x CoO2 Solid Solution.* Journal of The Electrochemical Society, 1996. **143**(3): p. 1114-1123.

117. Kusano, E., T. Kobayashi, N. Kashiwagi, T. Saitoh, S. Saiki, H. Nanto, and A. Kinbara, *Ion energy distribution in ionized dc sputtering measured by an energy-resolved mass spectrometer.* Vacuum, 1999. **53**(1–2): p. 21-24.

118. Kadlec, S., C. Quaeyhaegens, G. Knuyt, and L.M. Stals, *Energy distribution of ions in an unbalanced magnetron plasma measured with energy-resolved mass spectrometry.* Surface and Coatings Technology, 1997. **89**(1–2): p. 177-184.

119. Iriyama, Y., K. Nishimoto, C. Yada, T. Abe, Z. Ogumi, and K. Kikuchi, *Charge-Transfer Reaction at the Lithium Phosphorus Oxynitride Glass Electrolyte/Lithium Manganese Oxide Thin-Film Interface and Its Stability on Cycling.* Journal of The Electrochemical Society, 2006. **153**(5): p. A821-A825.

120. Chan, C.K., H. Peng, G. Liu, K. McIlwrath, X.F. Zhang, R.A. Huggins, and Y. Cui, *High-performance lithium battery anodes using silicon nanowires.* Nat Nano, 2008. **3**(1): p. 31-35.

121. Wang, Z., J.Z. Lee, H. Xin, L. Han, N. Grillon, D. Guy-Bouyssou, E. Bouyssou, P. Proust, and Y.S. Meng, *Effects of Cathode Electrolyte Interfacial (CEI) Layer on Long Term Cycling of All-Solid-State Thin-Film Batteries.* Journal of Power Sources, 2016: p. Submitted.

122. Nykvist, B. and M. Nilsson, *Rapidly falling costs of battery packs for electric vehicles.* Nature Clim. Change, 2015. **5**(4): p. 329-332.

123. Fleutot, B., B. Pecquenard, F. Le Cras, B. Delis, H. Martinez, L. Dupont, and D. Guy-Bouyssou, *Characterization of all-solid-state Li/LiPONB/TiOS microbatteries produced at the pilot scale.* Journal of Power Sources, 2011. **196**(23): p. 10289-10296.

124. Phan, V.P., B. Pecquenard, and F. Le Cras, *High-Performance All-Solid-State Cells Fabricated With Silicon Electrodes.* Advanced Functional Materials, 2012. **22**(12): p. 2580-2584.

125. Bates, J.B. and N.J. Dudney, *Thin Film Rechargeable Lithium Batteries for Implantable Devices.* ASAIO Journal, 1997. **43**(5): p. M647.

126. Haruta, M., S. Shiraki, T. Suzuki, A. Kumatani, T. Ohsawa, Y. Takagi, R. Shimizu, and T. Hitosugi, *Negligible "Negative Space-Charge Layer Effects" at Oxide-Electrolyte/Electrode Interfaces of Thin-Film Batteries.* Nano Letters, 2015. **15**(3): p. 1498-1502.

127. S. Larfaillou, D.G.-B., F. Le Cras, S. Franger. *Characterization of Lithium Thin Film Batteries by Electrochemical Impedance Spectroscopy*. in *ECS Meeting*. 2014. Orlando.

128. Wang, Z., D. Santhanagopalan, W. Zhang, F. Wang, H. Xin, K. He, J. Li, N.J. Dudney, and Y.S. Meng, *In situ STEM/EELS Observation of Nanoscale Interfacial Phenomena in All-Solid-State Batteries.* Nano Letters, 2015. **Manuscript Submitted**.

129. Li, J., C. Ma, M. Chi, C. Liang, and N.J. Dudney, *Solid Electrolyte: the Key for High-Voltage Lithium Batteries.* Advanced Energy Materials, 2014: p. 1401408.

130. Richards, W.D., L.J. Miara, Y. Wang, J.C. Kim, and G. Ceder, *Interface stability in solid-state batteries.* Chemistry of Materials, 2015.

131. McCalla, E., A.M. Abakumov, M. Saubanère, D. Foix, E.J. Berg, G. Rousse, M.-L. Doublet, D. Gonbeau, P. Novák, G. Van Tendeloo, R. Dominko, and J.-M. Tarascon, *Visualization of O-O peroxo-like dimers in high-capacity layered oxides for Li-ion batteries.* Science, 2015. **350**(6267): p. 1516-1521.

132. Gomez, E.D., A. Panday, E.H. Feng, V. Chen, G.M. Stone, A.M. Minor, C. Kisielowski, K.H. Downing, O. Borodin, G.D. Smith, and N.P. Balsara, *Effect of Ion Distribution on Conductivity of Block Copolymer Electrolytes.* Nano Letters, 2009. **9**(3): p. 1212-1216.

133. Huang, R., Y.H. Ikuhara, T. Mizoguchi, S.D. Findlay, A. Kuwabara, C.A.J. Fisher, H. Moriwake, H. Oki, T. Hirayama, and Y. Ikuhara, *Oxygen-Vacancy Ordering at Surfaces of Lithium Manganese(III,IV) Oxide Spinel Nanoparticles.* Angewandte Chemie-International Edition, 2011. **50**(13): p. 3053-3057.

134. Truong, Q.D., M.K. Devaraju, T. Tomai, and I. Honma, *Direct Observation of Antisite Defects in LiCoPO4 Cathode Materials by Annular Dark- and Bright-Field Electron Microscopy.* Acs Applied Materials & Interfaces, 2013. **5**(20): p. 9926-9932.